Technische Universität München

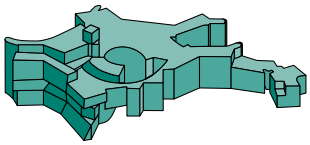

Max-Planck-Institut für Astrophysik

Non-axisymmetric modes in three-dimensional magnetized tori accreting onto black holes

Matteo Bugli

Vollständiger Abdruck der von der Fakultät für Physik der Technischen Universität München zur Erlangung des akademischen Grades eines

Doktors der Naturwissenschaften (Dr. rer. nat.)

genehmigten Dissertation.

Vorsitzende:		Prof. Dr. Elisa Resconi
Prüfer der Dissertation:	1.	apl. Prof. Dr. Ewald Müller
	2.	Prof. Dr. Alejandro Ibarra

Die Dissertation wurde am 09.03.2017 bei der Technischen Universität München eingereicht und durch die Fakultät für Physik am 28.04.2017 angenommen.

Dedicated to Ms. Babbi

Acknowledgments

After more than three years spent here in Munich, I've come to realize three fundamental truths: (1) I will never learn Bavarian; (2) The laws of Physics here do not apply to joggers when they run on thick ice; (3) There is no such thing as too much meat on a restaurant's menu.
They say that you really start appreciating something only when you lose it, and all this time away from my hometown, Florence, should have taught me that. Luckily for me, my Mom has never missed our daily Skype call in all these years, I guess to mercifully prevent me from knowing the excruciating pain of homesickness. Only because fortified by her and my father's unconditional love (but mostly by their homemade tomato sauce, chestnut flour, and marmalades) I've been able to survive the cold German winters.
To my brothers goes a special thank, as they were able to cope with my crippling absence and at the same time compensate for it with my parents by keeping them extremely busy. Thanks, guys. I owe you a big one.
This side of the Alps (someone would say the *wrong* one) has been also extremely generous, though. My gratitude goes of course to Ewald, who almost four years ago believed in this young Italian expat, despite him being ridiculously late for any application and having visited MPA without any shred of invitation.
This work would have never come to an end if it wasn't for a very bright Neapolitan that took my code and pimped it better than Xzibit could have ever done. A Gallehault indeed, that Advance Fortran Course at LRZ. Thank you, Fabio.
A special mention to the excellent Dr. Ertl and Dr. Melson from the Max Planck Department for Pedantry and Semantics. They brilliantly showed me the difference between 500 *words* and 500 *characters*, and made it possible for all German speakers to understand what this manuscript is all about (i.e. magnetically glazed Donuts, in case it wasn't clear).
My gratitude goes also to my officemate Dijana, who sometimes utterly misunderstood the meaning of the words: "*No, thanks*", and never missed a chance to stuff me with cookies, chocolate, and cake. Half of my body fat is on you, lady (the rest is just a byproduct of my systematic lack of willpower).
To my 3% blood-brother Haakon I say *"Takk for at vi kunne dele en felles smerte"*.
Thanks to all the people that in all these years gave me a chance to immerse myself into the Socratic method. Whether it was a passionate debate over the nature of morality, an argument about the teleport machine/suicide-box conundrum or a dream-like conversation about why on Earth do sloths climb down a tree to

poop, I've always felt enriched after these exchanges.
But above all, I want to thank the person who, probably driven by a pronounced self-destructive tendency, decided to follow me across the Alps and made this whole experience in Munich possible. For her, I would start another Ph.D. tomorrow (then stop, two is my hard limit). Grazie, Amore.

Contents

List of Figures

List of Tables

"When you have eliminated all which is impossible, then whatever remains, however improbable, must be the truth."

— Arthur Conan Doyle, *The sign of the Four*

1. Introduction

Accretion of matter onto black holes in one of the most efficient mechanisms in the Universe in producing high-energy radiation, and for this reason it is considered to be the central engine that powers up a number of different astrophysical sources. Accretion disks orbiting around a central compact object represent a fundamental ingredient in the current models explaining the high-energy emission from such sources as active galactic nuclei (AGNs) (Rees, 1984; Marconi et al., 2004; Reynolds, 2014), x-ray binaries (XRBs) (Narayan and Yi, 1995; Fender et al., 2004; Remillard and McClintock, 2006) and gamma-ray bursts (GRBs) (Woosley, 1993; Piran, 1999; Kumar and Zhang, 2015), just to cite a few.
To get an idea of how powerful an energy source accretion can be, consider a body of mass M and radius R_* on whose surface a mass m is accreted. Then the gravitational potential energy of the mass m is

$$\Delta E_{\rm acc} = GMm/R_*, \tag{1.1}$$

where G is the gravitational constant. Considering the typical case of a neutron star with radius $R_* \sim 10$ km and mass $M \sim M_\odot$, the solar mass, then the released energy $\Delta E_{\rm acc}$ is roughly 10^{20} erg per accreted gram. Let us compare it to the energy produced by nuclear fusion reactions. In the most favorable case, i.e. conversion (or burning) of hydrogen into helium, the energy release is

$$\Delta E_{\rm nuc} = 0.007mc^2, \tag{1.2}$$

where c is the speed of light. Hence we obtain 6×10^{18} erg g^{-1} from the most energetic fusion reaction, which is about 20 times less than what accretion yields in the case we considered. It is clear from Eq. (1.1), though, that the efficiency of accretion as energy source strongly depends on the compactness of the central object: the larger the ratio M/R_*, the greater the energy output.
The conservation of angular momentum commonly leads to the formation of accretion disks orbiting around a central object, whether it is a protoplanetary disk around a young forming star or a thick torus surrounding a supermassive black hole at the center of a galaxy. This means, however, that some physical mechanism is required to transport angular momentum outwards, leading to sufficiently high accretion rates that can ultimately explain the observed emission from high-energy sources.

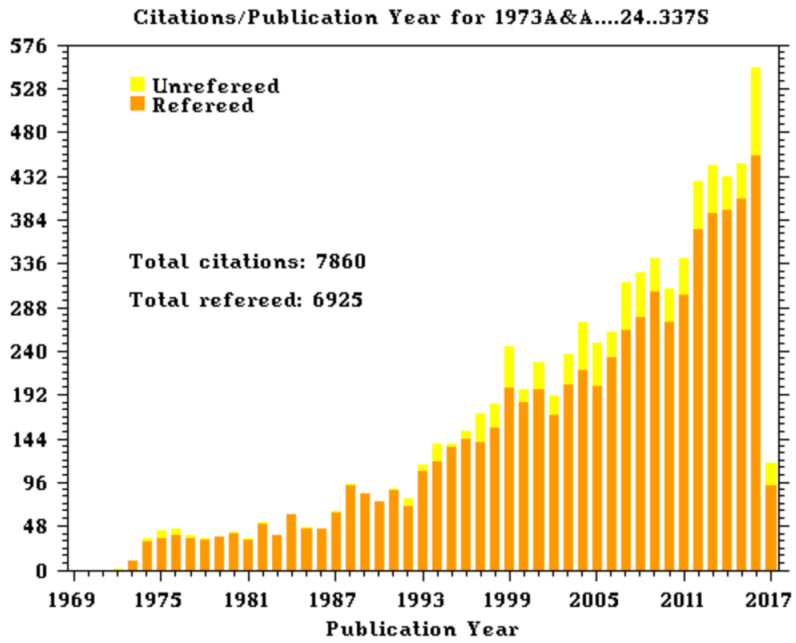

Figure 1.1.: Citation history of the seminal paper Shakura and Sunyaev (1973). (`http://adsabs.harvard.edu/`)

Since black-hole-disk models were proposed as central engine for quasar by Lynden-Bell (1969), there has been a continuous interest in the physics underlying accretion onto black holes. The seminal papers by Shakura and Sunyaev (1973) and Lynden-Bell and Pringle (1974) first described what now is known as the *standard disk model*: a geometrically thin, optically thick Keplerian disk where the accretion process is driven by a local turbulent viscosity that is parametrized by the quantity α. Given the great success of the standard disk model in providing a self-consistent and plausible way to enable accretion, the actual nature and physical mechanism behind the parameter α (which essentially gives an estimate of the efficiency of the angular momentum transport in the disk) has been the object of numerous studies and is currently still under investigation. Fig. 1.1 gives a sense of how influential the standard disk model still is, as the number of citations per year to the work by Shakura and Sunyaev (1973) increases steadily. Hydrodynamic Keplerian disk models have always had significant problems in explaining from first principles the nature of accretion. They are indeed stable to local linear perturbations, since their distribution of specific angular momentum increases with distance from the central object (this is the well-known Rayleigh stability criterion), and in general, a small displacement of a fluid element will lead to epicyclic oscillations. The non-linear stability of hydrodynamic disks is to this date a matter of debate. In particular, at high enough Reynolds numbers non-linear perturbations could lead to self-sustained turbulence (Lesur and Longaretti, 2005), but it would be too weak to explain observed accretion rates.

An important class of hydrodynamic disks often used in the context of accretion onto black holes are accretion tori (Abramowicz et al., 1978), also referred to as *Polish doughnuts* (Fig. 1.2). These thick disks have a large internal energy, and they rely on pressure gradients to support the disk together with centrifugal forces, resulting in a significant vertical thickening of the disk and a departure from a Keplerian distribution of specific angular momentum. Despite their local stability, Papaloizou and Pringle (1984) discovered that they are prone to develop a global non-axisymmetric instability (known as Papaloizou-Pringle instability, PPI) which is able to transport angular momentum outwards. Although capable of triggering some accretion, the PPI could not explain in a satisfactory way the ubiquity of accreting systems (since it mainly affects nearly constant angular momentum tori) and it did not fit well in the standard disk model (which requires the onset of a turbulent environment to enable accretion).

The breakthrough in accretion theory was the realization that magnetic fields are the key to explain how disks can get rid of their angular momentum. The discovery of the *magnetorotational instability* (MRI) in astrophysics by Balbus and

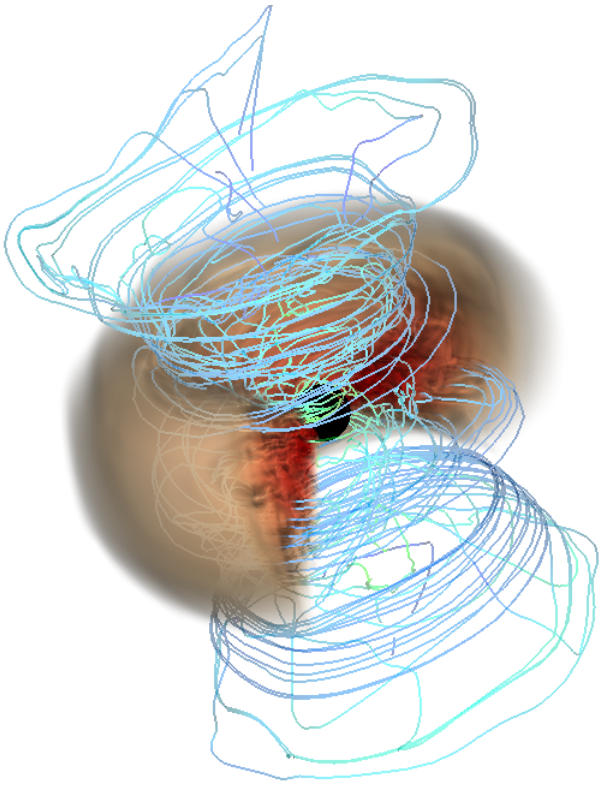

Figure 1.2.: Volume rendering of the rest mass density of a thick accretion disk (model T256r3s12 from Chapter 5, see Table 5.3 for the details). The lines are streamlines of the fluid velocity colour-coded according to the strength of the magnetic field (low for dark blue, high for light green).

Hawley (1991) provided a local mechanism, efficient for a wide range of magnetic field strength, which leads to a growth on dynamical time-scales of linear perturbations and naturally develops MHD turbulence. The only necessary condition for its onset is the presence of a differentially rotating fluid threaded by a weak magnetic field. Since its discovery, the properties of the MRI have been investigated in great detail by both analytical and numerical studies. In the latter case, one can find two major numerical tools that have been extensively employed in the literature and differ by the typical length scale they focus on:

- *Shearing box simulations*: they consider a very thin slice of an accretion disk, and allow for the simulation of the local development of the MRI and the investigation of its growth, saturation and general statistical properties.

- *Global simulations*: they evolve an accretion disk in its entirety and can study non-local dynamical phenomena (as the interaction with the disk's edges or the development of winds and jets).

Both approaches are of course important to reach a better understanding of the MRI and accretion physics in general.
Ordered large-scale magnetic fields are expected in accretion disks around black holes, as they represent a key ingredient in the launching mechanism and collimation of relativistic jets from AGNs McKinney and Blandford (2009). They can also affect the disk's global stability. For instance, magnetic pressure dominated thin disks are stable against the *thermal instability* that affects radiation dominated disks (Sądowski, 2016), while sufficiently strong (super-thermal) toroidal fields seem to rapidly destabilize thick accretion tori (Fragile and Sadowski, 2017).

Despite the fundamental importance of magnetic fields in providing a general and universal mechanism to enable accretion in astrophysical disks, the PPI is still quite relevant as an agent of global non-axisymmetric instability, since thick disks with sub-Keplerian angular momentum distributions are expected to form in binary neutron stars (NS-NS) (Rezzolla et al., 2010; Kiuchi et al., 2010) or black hole-neutron star (BH-NS) (Shibata and Uryū, 2006; Foucart et al., 2012) mergers, and also after the rotational gravitational collapse of massive stars (MacFadyen and Woosley, 1999; Aloy et al., 1999). The stability of such wide tori has been studied from both an analytical (Goldreich et al., 1986; Glatzel, 1987) and numerical (Blaes and Hawley, 1988; Hawley, 1991; De Villiers and Hawley, 2002) point of view. They have been proven to be quite generally unstable to some non-axisymmetric mode induced by the PPI. In recent years there have been several studies which included self-gravity of the disk (Kiuchi et al., 2011; **?**). They have shown how the non-axisymmetric structures that arise from the instability can lead to a significant emission of gravitational waves.
Nevertheless, the relative importance of both MRI and PPI in the evolution and

dynamics of an important class of accretion flows, such as thick disks around black holes, has not yet been studied in detail. Though it is quite well known how they individually operate in differentially rotating astrophysical flows, it is still not completely clear how they interact with each other and whether one instability dominates the other (and if so, why and for which particular disk models would that be). Fu and Lai (2011) tried to analytically establish the effect of magnetic fields on the development of the PPI. Their analysis (which assumed an incompressible fluid) suggested that sufficiently strong magnetic fields could actually further destabilize the torus and reinvigorate the hydrodynamical instability. Wielgus et al. (2015) studied the stability of strongly magnetized tori, showing the onset of the non-axisymmetric MRI for initial purely toroidal magnetic configurations. Their models, however, did only cover a limited azimuthal range ($\phi \in \{0, \pi/2\}$). Therefore they could only capture the dynamics of modes with an azimuthal number m being a multiple of 4.

Our main goal is to investigate what is the interplay between PPI and MRI, how these instabilities affect each other, and whether or not one dominates over the other. The numerical tool we chose is the General Relativistic Magnetohydrodynamic (GRMHD) code `ECHO` (Del Zanna et al., 2007). This code has been extended in the last 4 years from its original version to include non-ideal effects such as turbulent resistivity and a mean-field dynamo mechanism. Both these physical processes have been tested in the context of accretion disks through kinematic simulations of $\alpha\Omega$-dynamo in magnetized tori (Bugli et al., 2014), but the former is particularly interesting for the investigation of the PPI-MRI interaction. Resistivity can in fact deeply affect the onset of MHD turbulence, while a hydrodynamic process such as PPI is not influenced by it. Therefore, a finite conductivity is likely to have a significant impact on the system evolution.

In Chapter 2 we present the theoretical models of the two instabilities, their main properties, and the fundamental aspects of turbulent mean-field dynamo theory. Then we introduce the GRMHD formalism and the disk models used in our simulations in Chapter 3, while Chapter 4 describes the structure of the code `ECHO` and its recently developed parallelization scheme. In Chapter 5 we first show the results of the study of the $\alpha\Omega$-dynamo in thick disks and then discuss three-dimensional GRMHD simulations of magnetized tori with the goal to establish the effect of the MRI on the PPI development. Finally, we present some conclusions and perspectives in Chapter 6.

2. Accretion disks theory

Accretion disks are complex systems where different physical mechanisms have an active role in shaping their dynamics. There are *dynamical* processes (gravity, pressure forces, rotation) that act on time-scales $t_{dyn} \sim 1/\Omega_0$, where Ω_0 is a typical value for the orbital angular velocity of the disk; there are then *thermal* processes that develop on a typical time $t_{th} \sim c_s^2/(\nu_* \Omega_0^2)$, where c_s is the local sound speed and ν_* is the disk kinematic viscosity; finally we have *viscous* processes on the characteristic time-scale $t_{vis} \sim r^2/\nu_*$, with r the radial distance from the central object. Since the dynamical phenomena are typically faster than the thermal and viscous ones (and thus $t_{dyn} \ll t_{th} \ll t_{vis}$) a first approximation that is usually made is to consider only the dynamical structure of the disk.
Let us start by considering hydrodynamic disks, i.e. neglecting magnetic fields. Depending then on the relative importance of the different forces considered (gravity, pressure and rotation) it will be possible to have quite different disk models, in particular with very different values for the accretion efficiency

$$\eta_{\rm acc} \equiv \frac{L}{\dot{M}c^2}, \tag{2.1}$$

where L is the source luminosity, $\dot{M}$ is the accretion rate and c is the speed of light. The parameter $\eta_{\rm acc}$ represents a measure of how much of the accreted mass has been radiated away as energy, and for accreting black holes it can reach values of $\eta_{\rm acc} \sim 0.1$. If we neglect the disk self-gravity and consider the gravitational background to be set by the central black hole, then we end up with a classification of the possible accretion flows that is specified by the relative importance of pressure gradients and rotational support (see Table 2.1). If the contribution of the latter is not dominant, and there are significant pressure gradients we obtain the so-called *Advection Dominated Accretion Flows* (ADAFs) or, when the pressure support is negligible, a free-falling flow onto the black hole (the *Bondi* solution). If, on the other hand, the flow exhibits fast rotation, the accreting matter has significant angular momentum and forms a disk-like structure. In this case the possible solutions may be divided into the following classes (in order of increasing vertical sizes):

- Thin disk: their rotational profile are fundamentally Keplerian, that is rotation fully supports the disk, with negligible contribution from the pressure gradients in the radial direction. As a consequence, the typical vertical scale

height H required by hydrostatic equilibrium conditions is small compared to the disk's radial extent R, i.e. $H/R \ll 1$, and the local orbital velocity (which approaches the Keplerian value) is highly supersonic

$$r\Omega_K \gg c_s, \tag{2.2}$$

where Ω_K is the Keplerian angular velocity. Transport of energy by advection with the flow is very inefficient, meaning that the radial velocities involved are quite small ($v_r \ll c_s \ll r\Omega$), and there is essentially local equilibrium between viscous heating and radiative cooling. The resulting accretion rates $\dot{M}$ are small in the sense of

$$\dot{m} \equiv \frac{0.1\dot{M}c^2}{L_{\rm Edd}} = \frac{L}{L_{\rm Edd}}\frac{0.1}{\eta_{\rm acc}} < 1, \tag{2.3}$$

where $L_{\rm Edd}$ is the *Eddington luminosity*, that is the maximum value of an accreting source's luminosity beyond which the outgoing radiation pressure is strong enough to counteract the gravitational pull and push the infalling material further away from the central object. For these systems $\eta_{\rm acc} \sim 0.1$.

- Slim disk: in this case the radial velocities involved and the thickness of the disk are high enough to make advection another efficient cooling mechanism, besides radiation. This means higher accretion rates ($\dot{m} \gtrsim 1$) , $H/R \sim 1$ and a typical efficiency $\eta < 0.1$. It may be considered a more general realization of an accretion disk with radiative cooling, as it reduces to a thin disk in the limit of weak advection.

- Thick disk: when the radial pressure gradients are no longer negligible they contribute significantly to the disk support and therefore the vertical size of the disk increases significantly, i.e. $H/R \gtrsim 1$ (for this reason they are also referred to as accreting *tori*). Contrary to the former models, these disks are *radiatively inefficient*, that is they lack an efficient radiative cooling mechanism. Accretion rates can be very high in this case ($\dot{m} \gg 1$), but the efficiency drops accordingly to very low values $\eta_{\rm acc} \ll 1$.

In the following sections we will focus mainly on some aspects regarding thin and thick accretion disks, having in mind the goal of investigating the dynamical stability of magnetized tori. For more details on accretion flows and disk models, the interested reader can also consult the excellent review on accretion onto black holes by Abramowicz and Fragile (2013) and the authoritative book *Accretion Power in Astrophysics* by Frank et al. (2002).

Table 2.1.: Simple classification of the most important accretion flows.

	Fast rotation (disks)	Slow rotation (Bondi-like)
Large pressure forces	**Thick, Slim**	**ADAFs**
Small pressure forces	**Thin**	**Free-fall**

2.0.1. Stability of hydrodynamic Keplerian disks

Following the exposition offered by Balbus and Hawley (1998), let us introduce the fundamental equations that regulate the dynamics of a non-relativistic hydrodynamic accretion disk, assuming it to be composed of an ideal gas of adiabatic index $\Upsilon = 5/3$. The first ingredient we need is the mass conservation equation

$$\frac{\partial \rho}{\partial t} + \boldsymbol{\nabla} \cdot (\rho \boldsymbol{v}) = 0, \tag{2.4}$$

where ρ is the mass density and $\boldsymbol{v}$ is the fluid velocity. The equation of motion is given instead by the conservation of momentum

$$\rho \frac{\partial \boldsymbol{v}}{\partial t} + (\rho \boldsymbol{v} \cdot \boldsymbol{\nabla})\boldsymbol{v} = -\boldsymbol{\nabla} p - \rho \boldsymbol{\nabla} \Phi + \eta_V \left(\nabla^2 \boldsymbol{v} + \frac{1}{3} \boldsymbol{\nabla} (\boldsymbol{\nabla} \cdot \boldsymbol{v}) \right), \tag{2.5}$$

where p denotes the thermal pressure, Φ the gravitational potential, η_V the microscopic kinematic shear viscosity and the three terms on the right-hand side represent respectively the pressure, gravitational and viscous forces acting on the fluid. If we now take the dot product of Eq. (2.5) with $\boldsymbol{v}$ and use the mass conservation in Eq. (2.4) we obtain

$$\frac{\partial}{\partial t} \left(\frac{1}{2} \rho v^2 + \rho \Phi \right) + \boldsymbol{\nabla} \cdot \left[\boldsymbol{v} \left(\frac{1}{2} \rho v^2 + \rho \Phi + p \right) + \boldsymbol{F}_{\text{vis}} \right] = p \boldsymbol{\nabla} \cdot \boldsymbol{v} - \Psi, \tag{2.6}$$

which describes the evolution of the system's mechanical energy, that can be either transported by a dynamic flux (in the square brackets) or modified by doing work on the fluid (the $p \boldsymbol{\nabla} \cdot \boldsymbol{v}$ term) and heat losses (the Ψ term). The viscous flux

$$\boldsymbol{F}_{\text{vis}} = -\eta_V \left(\boldsymbol{\nabla} \frac{v^2}{2} + \frac{\boldsymbol{v}}{3} \boldsymbol{\nabla} \cdot \boldsymbol{v} \right), \tag{2.7}$$

does not usually contribute significantly to the transport and can generally be neglected, while the heat loss source term $(-\Psi)$ on the right-hand side is defined as

$$\Psi = \eta_V \left[\frac{1}{2} (\partial_i v_j)(\partial_i v_j) + \frac{1}{3} (\boldsymbol{\nabla} \cdot \boldsymbol{v})^2 \right]. \tag{2.8}$$

The internal energy density of the system $\rho \epsilon = p/(\Upsilon - 1)$ evolves on the other hand according to

$$\rho \left(\frac{\partial}{\partial t} + \boldsymbol{v} \cdot \boldsymbol{\nabla} \right) \frac{3p}{2\rho} = -p \boldsymbol{\nabla} \cdot \boldsymbol{v} - \boldsymbol{\nabla} \cdot \boldsymbol{F}_{\text{rad}} + \Psi, \tag{2.9}$$

where $\boldsymbol{F}_{\rm rad}$ is the radiative flux and Ψ takes into account the heating rate due to viscous dissipation. Combining Eq. (2.6) and Eq. (2.9) leads to

$$\frac{\partial}{\partial t}\left(\frac{1}{2}\rho v^2+\frac{3}{2}p+\rho\Phi\right)+\boldsymbol{\nabla}\cdot\left[\boldsymbol{v}\left(\frac{1}{2}\rho v^2+\rho\Phi+\frac{5}{2}p\right)\right]=-\boldsymbol{\nabla}\cdot\boldsymbol{F}_{\rm rad}, \qquad (2.10)$$

which shows how energy is lost from an isolated disk only through radiation, while there is no explicit contribution from the viscous source terms. This result simply means that any dissipation of mechanical energy leads to a corresponding increase of internal energy, with no net energy loss from the global system. Another important phenomenon is the conservation of angular momentum, which can be easily obtained by considering the azimuthal component of Eq. (2.5). If we introduce a cylindrical coordinate system (R,ϕ,z) with origin at the central black hole and multiply by R the ϕ-component equation, we get

$$\frac{\partial}{\partial t}(\rho R v_\phi)+\boldsymbol{\nabla}\cdot R\left(\rho v_\phi\boldsymbol{v}+p\hat{\boldsymbol{e}}_\phi\right)-\boldsymbol{\nabla}\cdot\left[\frac{R\eta_V}{3}(\boldsymbol{\nabla}\cdot\boldsymbol{v})\hat{\boldsymbol{e}}_\phi+\eta_V R^2\boldsymbol{\nabla}\frac{v_\phi}{R}\right]=0, \qquad (2.11)$$

where $\hat{\boldsymbol{e}}_\phi$ is the unit vector in the azimuthal direction and, as for the mechanical energy equation (2.6), the viscous transport term due to η_V can usually be neglected. Eq. (2.11) shows clearly that the angular momentum is, as expected, a locally conserved quantity that can be transported across the disk (as it is required in order to have accretion) but can never be destroyed.
Let us now specialize these findings for the case of flows orbiting around a central point mass M on circular orbits with Keplerian angular velocity

$$\Omega(R)=\sqrt{\frac{GM}{R^3}}. \qquad (2.12)$$

We separate the large-scale properties of the flow from the small-scale fluctuations by introducing the fluctuation velocity $\boldsymbol{u}$ as

$$\boldsymbol{u}\equiv\boldsymbol{v}-(R\Omega)\hat{\boldsymbol{e}}_\phi=(v_R,v_\phi-R\Omega,v_z), \qquad (2.13)$$

and we make use of the *local approximation*, meaning that we neglect the effect of curvature on the fluctuations' local behavior, and therefore we assume that $u\ll R\Omega$. Moreover, in the limit of subsonic turbulence (i.e. for $u\ll c_s$) the velocity field is nearly incompressible, and therefore we can adopt the so-called *Boussinesq approximation*: instead of naively setting $\boldsymbol{\nabla}\cdot\boldsymbol{v}=0$ everywhere (which is in general incompatible with Eq. (2.6)), we just assume the characteristic time-scale $t_{\rm char}\equiv(\boldsymbol{\nabla}\cdot\boldsymbol{v})^{-1}=(\boldsymbol{\nabla}\cdot\boldsymbol{u})^{-1}$ to be much longer than the characteristic turbulent turnover time $t_{\rm turn}\sim(\partial u/\partial x)^{-1}$, but not necessarily longer than other time-scales involved in the system (such as the ones related to rotation, thermal processes, etc.).
If we now define the derivation operator

$$\frac{D}{Dt}\equiv\frac{\partial}{\partial t}+\boldsymbol{u}\cdot\boldsymbol{\nabla}+\Omega\frac{\partial}{\partial\phi}, \qquad (2.14)$$

we can rewrite Eq. (2.5) by components as

$$\rho\left(\frac{Du_r}{Dt} - 2\Omega u_\phi\right) = -\frac{\partial p}{\partial R} + \eta_V \nabla^2 u_R, \tag{2.15}$$

$$\rho\frac{Du_z}{Dt} = -\frac{\partial p}{\partial z} - \rho\frac{\partial \Phi}{\partial z} + \eta_V \nabla^2 u_z, \tag{2.16}$$

$$\rho\left(\frac{Du_\phi}{Dt} + \frac{\kappa^2}{2\Omega}u_R\right) = -\frac{1}{R}\frac{\partial p}{\partial \phi} + \eta_V \nabla^2 u_\phi, \tag{2.17}$$

where κ is the so-called *epicyclic frequency*, defined by

$$\kappa^2 \equiv \frac{1}{R^3}\frac{d(R^4\Omega^2)}{dR}. \tag{2.18}$$

Linearizing the former equations allows one to retrieve a dispersion relation that characterizes the local stability of the system once we look for a solution for general modes in the form

$$u(R, \phi, z, t) = u_0(R, z)\exp[i(m\phi - \omega t)], \tag{2.19}$$

where ω is the mode frequency and $m \equiv k_\phi R$ is the mode's azimuthal number. To show the most interesting feature of Keplerian disks, let us restrict ourself to the case of a disk for which the orbital velocity $R\Omega$ exceeds the isothermal sound speed $c_s = \sqrt{p/\rho}$ by far. Then the disk's vertical structure is governed by hydrostatic balance

$$\frac{\partial p}{\partial z} = -\frac{GM\rho}{R^3}z = -\rho\Omega^2 z, \tag{2.20}$$

and the vertical density profile is given by

$$\rho = \rho_0 \exp(-\Omega^2 z^2/2c_s^2) = \rho_0 \exp(-z^2/H^2), \tag{2.21}$$

where ρ_0 is the density at the equatorial plane and $H = \sqrt{2}c_s/\Omega$ is the characteristic scale height. Since we assumed $R\Omega \gg c_s$ we also have $H/R \ll 1$, i.e. the disk is geometrically thin. Under these assumptions it is possible to show that the dispersion relation for a perturbation of frequency ω and wave number k is given by (Kato, 2016)

$$\omega^2 = \kappa^2, \tag{2.22}$$

showing that the response to a radial displacement of a fluid element is in fact an oscillation at frequency κ. In the most general case of compressible perturbations, Eq. (2.22) is slightly modified to

$$\omega^2 = c_s^2 k^2 + \kappa^2, \tag{2.23}$$

and describes the so-called *inertial-acoustic modes*. From Eq. (2.22) it is clear that the disk is stable whenever $\kappa^2 > 0$, in other words

$$\frac{dl}{dR} > 0 \tag{2.24}$$

where $l = R^2\Omega$ is the fluid's specific angular momentum. This stability condition, known as the *Rayleigh criterion*, is practically always satisfied by astrophysically relevant accretion disks, and therefore represents the main reason why hydrodynamic accretion disks are in fact extremely stable. When on the contrary $\kappa^2 < 0$, then for sufficiently large scales ($k^2 < k_{\rm th}^2 = -\kappa^2/c_s^2$) the flow is linearly unstable: an outwardly (inwardly) displaced fluid element will have a higher (lower) angular momentum than its surroundings, and therefore it will travel even further to the disk exterior (interior) setting in motion the *Rayleigh instability*.
Finally, it is interesting to calculate the behavior of the energy contained in the fluctuations. To do so we multiply Eq. (2.15),Eq. (2.16) and Eq. (2.17) respectively by u_R, u_z and u_ϕ, then we volume average, and by summing the three components we obtain

$$\frac{\partial}{\partial t}\langle\mathcal{E}\rangle + \boldsymbol{\nabla}\cdot\langle\boldsymbol{u}\mathcal{E} + \boldsymbol{u}p + \boldsymbol{F}_{\rm rad}\rangle = -\frac{d\Omega}{d\ln R}\langle\rho u_R u_\phi\rangle, \tag{2.25}$$

where

$$\mathcal{E} = \frac{1}{2}\rho u^2 + \frac{3}{2}p + \rho\Phi. \tag{2.26}$$

The operator $\langle\rangle$ performs a *global* azimuthal average and a *local* average along the z and R directions, i.e. along the full azimuthal range but on vertical and radial scales much smaller than the disk's thickness and radial extent. In contrast with the evolution of the total energy content in the disk given by Eq. (2.10), which exhibits no source term, the fluctuations can exchange energy with the mean-flow. The ultimate reason for the stability of differentially rotating disks with epicyclic motions lies in the azimuthal contribution of Eq. (2.25)

$$\frac{\partial}{\partial t}\left\langle\frac{\rho u_\phi^2}{2}\right\rangle + \boldsymbol{\nabla}\cdot\left\langle\frac{1}{2}\rho u_\phi^2\boldsymbol{u}\right\rangle = -\frac{\kappa^2}{2\Omega}\langle\rho u_R u_\phi\rangle - \left\langle\frac{u_\phi}{R}\frac{\partial p}{\partial\phi}\right\rangle - \eta_V\langle|\boldsymbol{\nabla}u_\phi|^2\rangle. \tag{2.27}$$

The mixing term (first on the right-hand side) couples the fluctuations to the mean flow's angular momentum distribution, leading to the linear stability represented by the Rayleigh criterion. It is though still a matter of debate whether non-linear perturbations can lead to self-sustained hydrodynamic turbulence, and hence angular momentum transport (Lesur and Longaretti, 2005).

2.1. Papaloizou-Pringle instability

Although hydrodynamic astrophysical disks prove to be locally very stable, the same cannot be said in general from a global point of view. Once the perturbation modes involve motions of the whole system and not just localized regions, then completely new dynamical responses may arise. This is the case for the

Papaloizou-Pringle instability (PPI, Papaloizou and Pringle (1984)), a mechanism that leads to the development of global non-axisymmetric modes in hydrodynamic thick *tori*.
Accretion disks belonging to this particular class are characterized by high internal temperatures and well-defined inner and outer boundaries. The main consequence is that pressure gradients can provide support against the gravitational force comparable to the centrifugal force, and therefore these disks are not purely rotationally supported as in the case of the thin disk model we considered in the previous section. As a result of this extra support the disk rotational profile will inevitably differ significantly from the Keplerian case, and thus its orbital velocity distribution will be said to be *sub-Keplerian*.

2.1.1. Slender incompressible tori

We now analyze in more detail the steps necessary to compute the fundamental characteristics of the PPI. We will first consider the case of a *slender torus*, i.e. a torus that extends from radius $R_0 - a$ to $R_0 + a$, with $a \ll R_0$. The equilibrium structure of the torus is such that in correspondence of the center R_0 the pressure reaches its maximum (Papaloizou and Pringle, 1984). The angular velocity is parametrized as

$$\Omega(R) = \Omega_0 \left(\frac{R}{R_0} \right)^{-q}, \tag{2.28}$$

where the parameter q can range from 3/2, corresponding to a Keplerian disk, to 2, which represents the case of a constant specific angular momentum distribution. This parameter relates also directly to the local linear stability of the disk, as we can plug Eq. (2.28) into the definition of the epicyclic frequency Eq. (2.18) to obtain

$$\kappa^2 = 2\Omega^2(2 - q), \tag{2.29}$$

from which it is evident that for $q > 2$ the disk is Rayleigh unstable, while the case $q = 2$ corresponds to a marginally stable accretion disk. It can be also shown (Papaloizou and Pringle, 1984) that the half-thickness of the torus can be expressed as $H = a\sqrt{2q - 3}$, ranging therefore from 0 for a Keplerian disk to a (circular cross-section) for the case $q = 2$.
To solve the problem of the evolution of the velocity ($\boldsymbol{u}$), density (ρ') and pressure (p') perturbations we need to specify an equation of state (EoS), which we will write in polytropic form

$$p = K\rho^{1+\frac{1}{n}}, \tag{2.30}$$

where the polytropic index n is a measure of the compressibility of the fluid; for instance $n = 0$ describes an incompressible fluid, while $n = \infty$ corresponds to an isothermal one. Instead of developing the calculations necessary to fully solve

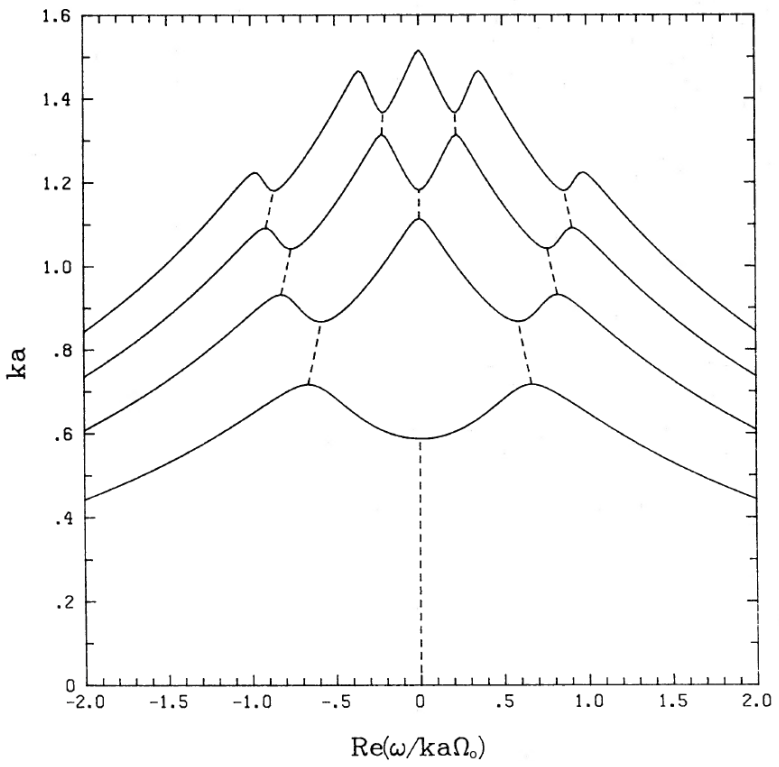

Figure 2.1.: Dispersion relation for an isentropic, incompressible ($n = 0$), constant angular momentum ($q = 2$) torus, where $k = m/R_0$, $\Omega_0 = \Omega(R_0)$ is the disk local orbital velocity and the horizontal axis $Re(\omega/ka\Omega)$ equals $q\xi_c$. The solid curves represent neutral modes, while the dashed curves can be shown to represent unstable modes. (Goldreich et al., 1986)

the analytical problem in detail, we will only outline the overall strategy, the consequent findings, and comment on their physical meaning.
After linearizing the three components of the Euler equation, the continuity equation, and the EoS, and imposing a solution of the form given in Eq. (2.19), we end up with a partial differential equation in (R, z) with eigenvalue ω whose solution requires the selection of appropriate boundary conditions (which in this case is the vanishing of the Lagrangian pressure perturbation at the disk's edges). This is the main difference with the local analysis that produced the Rayleigh criterion in Eq. (2.24). It allows one to capture the effect of global motions across the disk and interactions with the edges of the system. A generic mode of frequency ω will represent a pattern of fluid rotating (in the inertial frame) with angular velocity Ω_p and growing exponentially in time as $\exp(st)$, where

$$\Omega_p = Re(\omega)/m, \tag{2.31}$$

$$s = Im(\omega). \tag{2.32}$$

For a given value of Ω_p we may calculate at which radius R_c the pattern or-

bital velocity matches the local disk one, i.e. the *corotation radius*. Using the approximation of slender torus, we can express the velocity of the mean flow as

$$v_\phi = R\Omega(R) \simeq R\Omega_0 - q\Omega_0(R - R_0), \tag{2.33}$$

where $\Omega_0 = \Omega(R_0)$ is the angular velocity at the torus center. Corotation between mean flow and perturbation requires that the latter's phase velocity has to match the mean flow velocity in a frame rotating with angular velocity Ω_0, i.e. $Re(\omega)/k = -q\Omega_0(R_c - R_0)$. This can be expressed in a convenient way using the parameter

$$\xi_c \equiv \frac{R_c - R_0}{a} = -\frac{1}{qka}\frac{Re(\omega)}{\Omega_0}, \tag{2.34}$$

where $k \equiv k_\phi$ and the parameter ξ can assume values within the range $[-1, +1]$ (assuming the corotation radius lies within the disk). From the dispersion relation in Fig. 2.1 we can identify two main branches for the unstable modes (dashed lines):

- Principal branch: this class is present for values of $ka < 0.59$ and has a corotation radius at the torus pressure maximum, i.e. $R_c = R_0$. Its modes are essentially independent of z and therefore two-dimensional, and the fastest-growing one occurs for $ka = 0.38$ with growth rate $s = 0.29\Omega_0$.

- Higher-oder modes: these modes occurring at higher values of ka are intrinsically three-dimensional and have lower growth rates. The corotation radius does not necessarily coincide with the pressure maximum, but lies however within the torus boundaries.

We now discuss the physical mechanism responsible for the onset of the PPI. The starting point is the role of the corotation radius R_c. A wave propagating in the region where $R > R_c$ will in general move faster than its surroundings, and therefore it will carry and transport *positive energy*, i.e. at its passage the energy of the medium will locally increase. The opposite will instead apply for a perturbation that propagates in the region contained within R_c. If the total energy is conserved (which is when there is no resonance at corotation that absorbs energy from incoming waves) a growing mode must have positive and negative energy in equal amounts and thus will require the corotation radius to be within the disk. It can be shown (Goldreich et al., 1986) that there is a *forbidden* zone around R_c where the radial part of the mode's eigenfunction is evanescent, surrounded by two *permitted* regions where the wave can propagate radially. This wave barrier at the corotation radius can be tunneled through by an incoming wave-packet, leading to a transmitted and reflected component. For a wave that reaches the exterior of the disk from the inner region the transmitted packet will have positive energy, but then the reflected one will end up having even more negative energy than the original wave-packet to compensate for this gain. Since an analogous

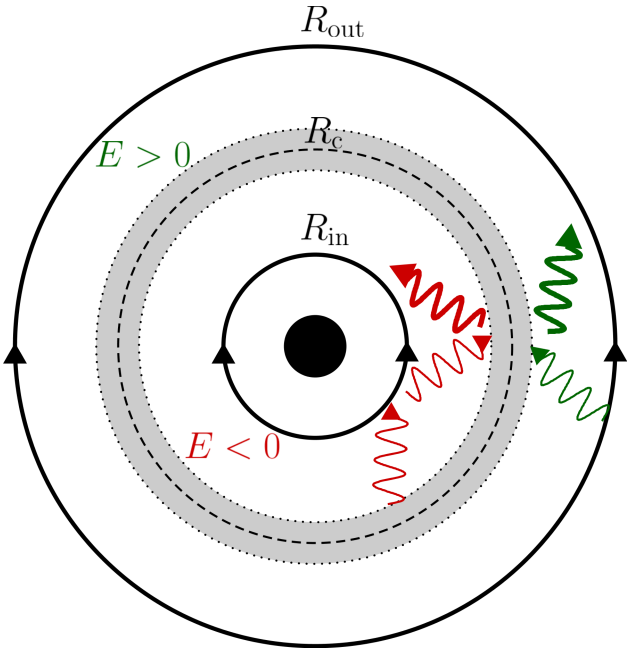

Figure 2.2.: Sketch of the fundamental physical mechanism responsible for the PPI development. The red and green waves represent respectively negative and positive energy waves, which interact at the corotation radius (dashed circle) and are *over-reflected* back. The gray area represents the *forbidden zone* nearby the corotation radius (dashed circle), where the waves become evanescent.

process will happen for waves propagating in the opposite direction (towards the disk's inner edge) the corotation radius acts effectively as an amplifier that allows the removal of energy (and angular momentum) from the region with $R < R_c$ and its deposition at radii $R > R_c$ (see Fig. 2.2).
In order for this process to be self-sustained some sort of positive feedback is required. This role is covered by the disk's edges that act as reflective boundaries and enable a continuous amplification of the energy transport at R_c. However, for this to be effective a phase condition has to be satisfied, that is there must be an integral number of wavelengths between boundary and corotation. For this reason the nature of the modes will, in general, depend significantly on the specific position of the inner and outer boundaries, and on whether the disk has just one or two edges: in the latter case there can be growing modes if both edges can satisfy the phase condition, but also neutral ones if only one side achieves the positive feedback.
Finally, we briefly focus on the modes belonging to the principal branch, since they differ from the others because they are nodeless in the radial direction. According to a physical picture first described by Blaes and Glatzel (1986) and Goldreich et al. (1986) the principal branch may be viewed as a superposition of incompressible surface waves (also called *edge waves*) traveling along the inner and outer edge of the slender torus. As a consequence of the disk shear due to the

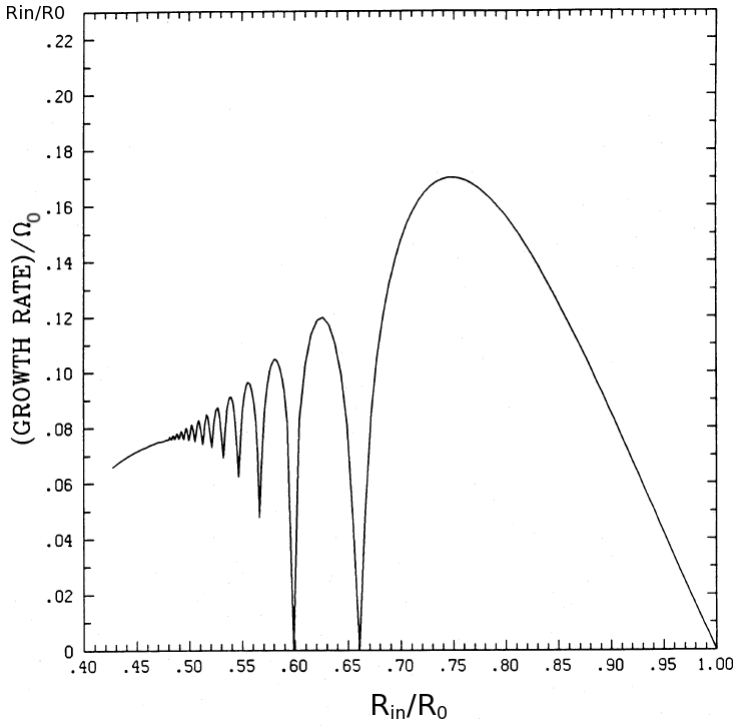

Figure 2.3.: PPI maximum linear growth rates as a function of the disk's width for the $m = 1$ mode. The horizontal axis gives the ratio $R_{\rm in}/R_0$, while the vertical one shows Ω_p/Ω_0. (Blaes and Hawley, 1988)

differential rotation, they are advected with respect to the pressure maximum at R_0 with velocity

$$V_s = q\Omega_0 a. \tag{2.35}$$

If the phase velocity of each edge wave is high enough to effectively counteract the shear, then the edge waves will interact at the corotation radius R_c and will constitute a growing mode. This is the reason why the very existence of these modes relies entirely on the dynamics of the system boundaries, which provides both the perturbations and the reflective mechanism.

2.1.2. Wide compressible tori

Let us now try to understand what is the response of the torus to linear perturbations once we relax the slender and incompressible assumptions we used so far. There is first of all a certain range of torus sizes $\Delta R = R_{\rm out} - R_{\rm in}$ for which the principal branch of the instability can efficiently develop (Blaes and Glatzel, 1986). Increasingly slender tori are unstable to all modes with $m \neq 0$, although the growth rate of any given mode decreases proportionally with ΔR because the shear across the corotation radius is also becoming smaller, and with

it the energy reservoir tapped by the instability. However, as ΔR gets smaller, the highest growth rate will appear at higher m and will tend to a constant value. Increasing the size of the torus leads at first to an enhancement of the growth rates, but then the system becomes stable to the principal branch. This is due to the fact that the larger is the radial extension of the torus, the larger is the shear between the corotation radius and the external edge, and therefore the faster the edge wave is advected with respect to the corotation radius.
Very wide tori seem therefore stable to large-scale (low-order) perturbations. However, once we consider compressible perturbations, low-order modes can develop in wide tori but instead of being the superposition of two nodeless edge waves they result from the interaction between an internal surface wave and an external acoustic wave. This is illustrated in Fig. 2.3, where the first maximum from the right represents the principal branch, while the following maxima describe the interaction between a surface wave advected by the shear for $R < R_c$ and an acoustic wave propagating along the radial direction. The second maximum results from an acoustic wave with one radial node, the next one to the left from a wave with two nodes and so on. The more the disk becomes stable to the principal branch, the less important is the outer edge. The only boundary that really matters is therefore the inner one as the torus size increases, leading to the inner standing wave being reflected back and forth between $R_{\rm in}$ and R_c. These kind of modes are the ones of interest for our study, as it will become clear in Chapter 5.

2.2. Magnetorotational instability

After discussing the stability and dynamical properties of hydrodynamic disks we now study the effect of magnetic fields which, compared to the unmagnetized case, will give rise to qualitative differences because of the onset of the *magnetorotational instability* (MRI), a mechanism first studied by Chandrasekhar (1960) in plasma physics but rediscovered in the context of accretion disks only 30 years later by Balbus and Hawley (1991). Magnetic fields represent the fundamental ingredient that allowed accretion disk theory to make a giant leap forward during the last 25 years. It is therefore of great importance to elucidate their role in the stability of accretion disks.
Let us consider a magnetized plasma of ions and electrons permeated by an electric field $\boldsymbol{E}$ and a magnetic field $\boldsymbol{B}$, whose evolution is governed by Faraday's and Ampere's law

$$\boldsymbol{\nabla} \times \boldsymbol{E} = -\frac{1}{c}\frac{\partial \boldsymbol{B}}{\partial t}, \tag{2.36}$$

$$\boldsymbol{\nabla} \times \boldsymbol{B} = \frac{1}{c}\left(4\pi \boldsymbol{J} + \frac{\partial \boldsymbol{E}}{\partial t}\right), \tag{2.37}$$

where the current $\boldsymbol{J}$ is related to the electromagnetic field by Ohm's law

$$\boldsymbol{J} = \sigma \left(\boldsymbol{E} + \frac{\boldsymbol{v}}{c} \times \boldsymbol{B} \right), \tag{2.38}$$

with σ being the plasma conductivity. Since we restrict ourselves to non-relativistic motions, we can neglect the displacement current term in Eq. (2.37). Inserting the latter expression, i.e. $\boldsymbol{J} = c/4\pi \boldsymbol{\nabla} \times \boldsymbol{B}$, into Eq. (2.38), solving for $\boldsymbol{E}$, and substituting the result into Eq. (2.36) provides us with the so-called *induction equation*

$$\frac{\partial \boldsymbol{B}}{\partial t} = \boldsymbol{\nabla} \times (\boldsymbol{v} \times \boldsymbol{B} - \eta_B \boldsymbol{\nabla} \times \boldsymbol{B}), \tag{2.39}$$

which describes the evolution of the magnetic field in a conducting fluid of velocity $\boldsymbol{v}$, and where we defined the microscopic resistivity $\eta_B = c^2/(4\pi\sigma)$. The presence of $\boldsymbol{B}$ directly affects the fluid through the action of the Lorentz force $\boldsymbol{F}_{\rm L} = \boldsymbol{J} \times \boldsymbol{B}/c$ on the electrical charges. By using once again Eq. (2.37) to eliminate $\boldsymbol{J}$ from the force expression and adding it to Eq. (2.5), we obtain

$$\rho \frac{\partial \boldsymbol{v}}{\partial t} + (\rho \boldsymbol{v} \cdot \boldsymbol{\nabla}) \boldsymbol{v} = -\boldsymbol{\nabla} p - \rho \boldsymbol{\nabla} \Phi + \frac{1}{4\pi} (\boldsymbol{\nabla} \times \boldsymbol{B}) \times \boldsymbol{B} + \eta_V \left(\nabla^2 \boldsymbol{v} + \frac{1}{3} \boldsymbol{\nabla} (\boldsymbol{\nabla} \cdot \boldsymbol{v}) \right). \tag{2.40}$$

This expression can be written in a more useful form as

$$\rho \frac{\partial \boldsymbol{v}}{\partial t} + (\rho \boldsymbol{v} \cdot \boldsymbol{\nabla}) \boldsymbol{v} = -\boldsymbol{\nabla} \left(p + \frac{B^2}{8\pi} \right) - \rho \boldsymbol{\nabla} \Phi + \left(\frac{\boldsymbol{B}}{4\pi} \cdot \boldsymbol{\nabla} \right) \boldsymbol{B} + \eta_V \left(\nabla^2 \boldsymbol{v} + \frac{1}{3} \boldsymbol{\nabla} (\boldsymbol{\nabla} \cdot \boldsymbol{v}) \right), \tag{2.41}$$

where we have used the vector identity

$$\boldsymbol{\nabla}(B^2) = 2[(\boldsymbol{B} \cdot \boldsymbol{\nabla}) \boldsymbol{B} + \boldsymbol{B} \times (\boldsymbol{\nabla} \times \boldsymbol{B})]. \tag{2.42}$$

According to Eq. (2.41) two new ingredients regulate the flow when a magnetic field is present:

- Magnetic pressure: the thermal pressure is enhanced by the term $B^2/8\pi$, which takes into account the extra support that the magnetic field provides to the system.

- Magnetic tension: the other term containing $\boldsymbol{B}$ represents a dynamical force that acts whenever the field exhibits some curvature and tends to *unbend* the field-lines back to a straight orientation.

To understand now what is the response of a magnetized fluid to a small perturbation, let us consider first the case of a non-rotating medium threaded by a magnetic field $\boldsymbol{B}$ and perturbed by a local disturbance of the form $\exp[i(\boldsymbol{k} \cdot \boldsymbol{r} - \omega t)]$, with $kr \gg 1$. By linearizing the continuity equation (2.4), the equation of motion

(2.41), the induction equation (2.39), and in the adiabatic limit, it can be shown that the resulting dispersion relation is (Balbus and Hawley, 1998)

$$[\omega^2 - (\boldsymbol{k}\cdot\boldsymbol{u_A})^2][\omega^4 - k^2\omega^2(c_s^2 + u_A^2) + (\boldsymbol{k}\cdot\boldsymbol{u_A})^2 k^2 c_s^2] = 0, \tag{2.43}$$

where we introduced the *Alfvén velocity* $\boldsymbol{u_A} = \boldsymbol{B}/\sqrt{4\pi\rho}$. Naming θ the angle between $\boldsymbol{B}$ and $\boldsymbol{k}$, we can write one obvious solution to Eq. (2.43)

$$\omega_A^2 = k^2 u_A^2 cos^2\theta, \tag{2.44}$$

which corresponds to the so-called *Alfvén waves*. These modes are compressionless disturbances which propagate along the magnetic field with velocity $\boldsymbol{u}_A$ and effective wave number $kcos\theta$. Since the restoring force that defines these modes is the magnetic tension, there is no hydrodynamic analog to them. Alfvén waves can be imagined to be similar to the vibrations of a pulled string (represented in this case by the magnetic field lines). The remaining roots of Eq. (2.43) correspond to the *fast* and *slow* modes, whose phase velocity is respectively higher and lower than that of the Alfvén wave. Their physics is more clearly explained if at least one of the following three conditions is fulfilled: $(1)c_s \ll u_A; (2)u_A \ll c_s; (3)cos\theta \ll 1$. Then the relations for the fast and slow modes become respectively

$$\omega_+^2 = k^2(u_A^2 + c_s^2), \tag{2.45}$$

$$\omega_-^2 = \frac{k^2 u_A^2 c_s^2 cos^2\theta}{u_A^2 + c_s^2}, \tag{2.46}$$

showing clearly that $\omega_+ > \omega_A > \omega_-$. From Eq. (2.45) we see that the fast mode is the result of the simultaneous action of magnetic and thermal pressures. In the limit of a vanishing magnetic field the fast mode becomes a simple sound wave, reason why it is sometimes referred to as *magnetosonic wave*. The slow mode results instead from the opposition between magnetic tension and gas compression. When $\boldsymbol{B}$ is strong the slow mode becomes a sound wave that propagates along the magnetic field lines, while it becomes degenerate with the Alfvén wave when the field is weak.
If Keplerian rotation is introduced into the previous analysis, the situation is significantly modified. Particularly if we consider the case of a weak magnetic field, the Alfvén wave and the slow wave are non-degenerate for $\Omega = 0$ due to a finite value of the fluid compressibility, but their frequencies start diverging once the rotation rate increases (Fig. 2.4). Eventually the slow mode becomes unstable ($\omega_-^2 < 0$) for a sufficiently high rotation rate (in the case of a Keplerian disk this occurs for $\Omega^2 > 1/3\ \omega_-^2$). This transition of the slow mode to instability in the case of rotation is in fact at the very core of the onset of the magnetorotational instability.

To better understand the physics of the MRI, let us now consider the simple

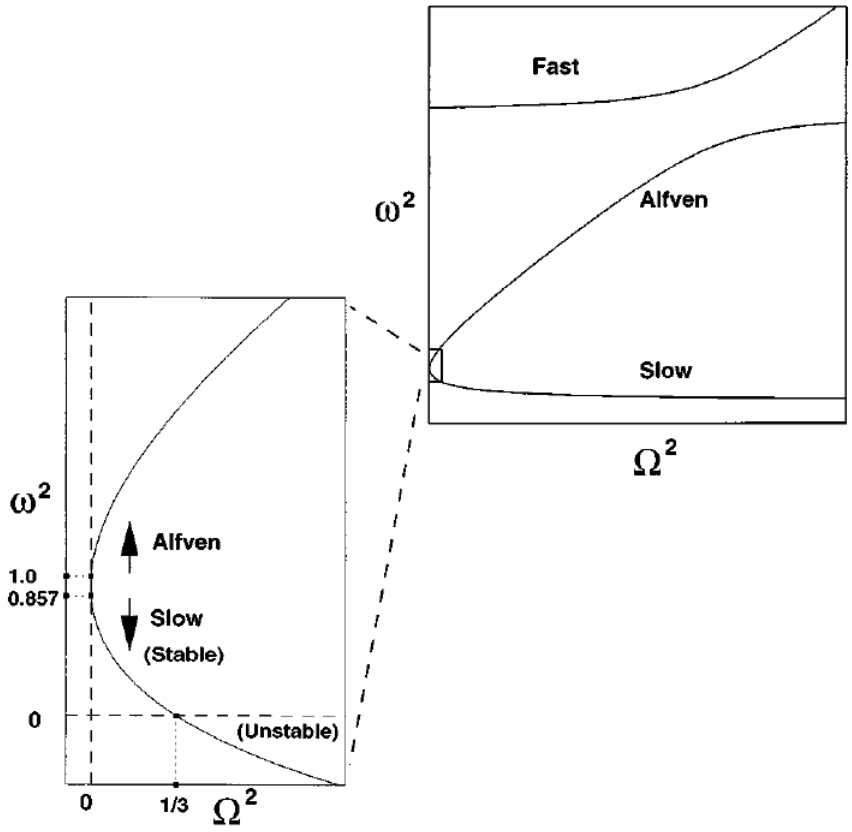

Figure 2.4.: Plot of the mode frequency ω^2 vs the rotation rate Ω^2 for a Keplerian disk. All frequencies are given in units of $\boldsymbol{k} \cdot \boldsymbol{u_A} = 1$. The numerical values correspond to the case $ku_{A\phi} = 2$, $kc_s = 5$. The expanded scale on the left shows the almost degenerate Alfvén and slow mode. (Balbus and Hawley, 1998)

case of an axisymmetric accretion disk threaded by a weak vertical magnetic field $\boldsymbol{B} = B\hat{\boldsymbol{e}}_z$, ignoring the effects of kinematic viscosity and magnetic resistivity. If we perturb a fluid element by a small amount $\boldsymbol{\xi}$ with spatial dependence e^{ikz}, then from the induction equation (2.39) one can derive

$$\delta\boldsymbol{B} = ikB\boldsymbol{\xi}, \quad \delta B_z = \xi_z = 0, \tag{2.47}$$

where $\delta\boldsymbol{B}$ is the magnetic field fluctuation vector. Using Eq. (2.47) we can compute the following expression for the magnetic tension term

$$\frac{ikB}{4\pi\rho}\delta\boldsymbol{B} = -(\boldsymbol{k} \cdot \boldsymbol{u_A})^2\boldsymbol{\xi}. \tag{2.48}$$

Since we are considering incompressible planar motions we can neglect the pressure contribution and rewrite the equations of motion in a simple and convenient

form

$$\ddot{\xi}_R - 2\Omega\dot{\xi}_\phi = -\left(\frac{d\Omega^2}{d\ln R} + (\boldsymbol{k}\cdot\boldsymbol{u_A})^2\right)\xi_R, \tag{2.49}$$

$$\ddot{\xi}_\phi + 2\Omega\dot{\xi}_R = -(\boldsymbol{k}\cdot\boldsymbol{u_A})^2\xi_\phi. \tag{2.50}$$

These equations provide a simple and suggestive physical interpretation for the effects of a weak magnetic field in accretion disks, as they describe the motion of two orbiting point masses connected by a spring with spring constant $(\boldsymbol{k}\cdot\boldsymbol{u_A})^2$. Let us call these two point masses m_+ and m_- and displace them from the same circular orbit to respectively an outer radius R_+ and an inner radius R_- (see Fig. 2.5). The point m_- will be orbiting faster than m_+ and their relative distance will increase accordingly, but since they are connected by a massless spring (i.e. the magnetic field with its tension) the inner mass will be pulled backwards and the outer one will be pushed forward. Thus, m_- will not remain on a stable orbit but instead it will fall even further towards the center (since it is losing angular momentum), and on the opposite the point m_+ will gain angular momentum and will be driven even further towards a more distant orbit. Therefore, the separation between m_- and m_+ widens and the whole process runs away.
The efficiency of this mechanism relies on the assumption that the spring constant is sufficiently weak to prevent oscillations during an orbital period. If this is not the case, the magnetic tension is strong enough to stabilize any radial displacement. Eq. (2.49) suggests the stability criterion

$$(\boldsymbol{k}\cdot\boldsymbol{u_A})^2 > -\frac{d\Omega^2}{d\ln R}, \tag{2.51}$$

from which we see that for sufficiently small k the disk will always be unstable, unless

$$\frac{d\Omega^2}{d\ln R} > 0. \tag{2.52}$$

But since Eq. (2.52) is a condition that is almost never encountered in astrophysical disks, there will be a lower limit for the wavenumber below which the system will be unstable. In this simplified problem we considered only the coupling of the modes with a vertical field, therefore to have stable mode the wavelength will have to exceed twice the scale height H, thus

$$u_A^2 > -\frac{1}{k^2}\frac{d\Omega^2}{d\ln R} \sim \frac{H^2}{\pi^2}\frac{d\Omega^2}{d\ln R} \sim \frac{6}{\pi^2}c_s^2. \tag{2.53}$$

The Alfvén velocity has therefore to exceed the sound velocity for the magnetic field to be *too strong* and hence have a stabilizing effect. It is interesting to note that there is no such constraint regarding the smallest value for the magnetic field. In the ideal MHD regime, where effects related to magnetic diffusivity are neglected, there is no limit to how weak $\boldsymbol{B}$ can be and still destabilize the system.

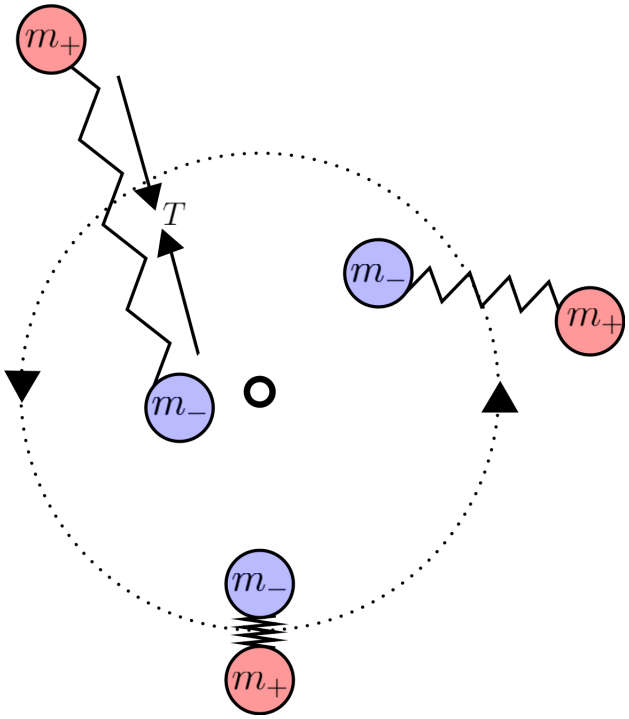

Figure 2.5.: Sketch of the physical mechanism responsible for the onset of the MRI. The magnetic tension T that acts on both masses m_+ and m_- leads to a run away instability and outward transport of angular momentum.

Its pure presence is sufficient to qualitatively change the dynamics of the disk. In this sense the MRI is also referred to as a *weak field instability*. As long as a sufficiently weak magnetic field is present in the disk there will always be unstable modes on sufficiently small scales.
From Eq. (2.49) and Eq. (2.50) we can derive the following dispersion relation

$$\omega^4 - \omega^2[\kappa^2 + 2(\boldsymbol{k}\cdot\boldsymbol{u_A})^2] + (\boldsymbol{k}\cdot\boldsymbol{u_A})^2\left((\boldsymbol{k}\cdot\boldsymbol{u_A})^2 + \frac{d\Omega^2}{d\ln R}\right) = 0, \tag{2.54}$$

from which the stability condition Eq. (2.51) follows directly. After some calculations we get the growth rate of the fastest growing mode

$$|\omega_{\max}| = \frac{1}{2}\left|\frac{d\Omega^2}{d\ln R}\right|, \tag{2.55}$$

which corresponds to

$$(\boldsymbol{k}\cdot\boldsymbol{u_A})^2_{\max} = -\left(\frac{1}{4} + \frac{\kappa^2}{16\Omega^2}\right)\frac{d\Omega^2}{d\ln R}. \tag{2.56}$$

For a Keplerian disk these relations reduce respectively to

$$|\omega_{\max}| = \frac{3}{4}\Omega, \quad (\boldsymbol{k}\cdot\boldsymbol{u_A})^2_{\max} = \frac{\sqrt{15}}{4}\Omega, \tag{2.57}$$

from which it is clear that the instability can develop on dynamical time-scales. Its onset can lead to extremely high amounts of energy tapped from the shear reservoir (and ultimately from the gravitational reservoir if the disk is Keplerian) which are injected in the MRI unstable modes. Moreover, the magnetic field strength sets the absolute scale for the fastest growing wavenumber $k_{\max}$, but has no effect in determining $|\omega_{\max}|$. The MRI growth rate is in general independent of the actual fluid magnetization. It just relies on its presence and its sufficient *weakness*.

2.2.1. Non-axisymmetric perturbations

We consider now a few aspects of the MRI which are related to the presence of an azimuthal magnetic field and ϕ-dependent disturbances. This interest is motivated by the fact that the PPI is an inherently non-axisymmetric instability. A full local analysis for non-axisymmetric perturbation was conducted by Balbus and Hawley (1992), from which we will just take the main results and general considerations.
One first point that has to be taken into account is that the interpretation of the system's *local* behavior gets more complicated in presence of shear and plane waves of the form $\exp i(\boldsymbol{k}\cdot\boldsymbol{r}-\omega t)$ with $\boldsymbol{k}$ having a ϕ component. The radial wave number will, in fact, show a time dependence given by the relation

$$k_R(t) = k_R(0) - mt\frac{d\Omega}{dR}, \tag{2.58}$$

where $k_R(0)$ is the initial value of k_R and $m = k_\phi R$ is the usual azimuthal number. From Eq. (2.58) is evident that only in the case of axisymmetric disturbances ($m = 0$) or absence of shear, the radial wave number is fixed, while in the more general case of a differentially rotating disk (with a finite value for m) the wave is first unwound by the shear (with $|k_R|$ decreasing to zero), and then is wrapped up as k_R increases linearly with time. Another consequence of the shear is that when a radial magnetic field is present, it gets stretched by the differential rotation and leads to a linear increase in time of the azimuthal field according to

$$B_\phi(t) = B_\phi(0) + tB_R\frac{d\Omega}{d\ln R}, \tag{2.59}$$

where $B_\phi(0)$ is the initial value of the azimuthal magnetic field component. This is the so-called Ω-*effect*. It represents a dynamo mechanism that converts the energy stored in the shear into magnetic energy by amplifying B_ϕ at the expense of $d\Omega/d\ln R$. Despite these complications, the time evolution of k_R and B_ϕ have the nice property of proceeding in such a way as to maintain the Alfvén coupling parameter $\boldsymbol{k}\cdot\boldsymbol{B}$ constant

$$\boldsymbol{k}\cdot\boldsymbol{B} = k_R(t)B_R + k_\phi B_\phi(t) = (\boldsymbol{k}\cdot\boldsymbol{B})_{t=0}, \tag{2.60}$$

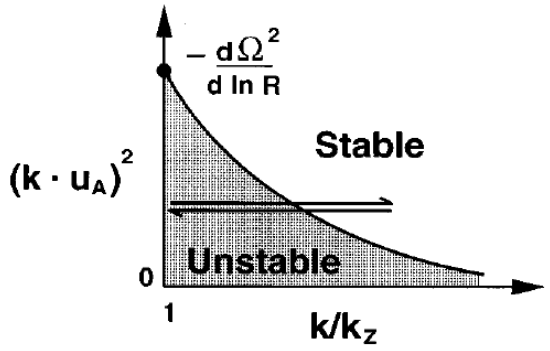

Figure 2.6.: $((\boldsymbol{k} \cdot \boldsymbol{u_A})^2, k/k_Z)$ plane. The shaded area represent the region of instability, while the path of a leading disturbance is represented by the arrows. (Balbus and Hawley, 1998)

because the shear terms cancel each other and the magnetic tension stays the same. Assuming that the winding time of k_R is longer compared to the disk orbital period, $m/R \ll k_Z$, and that the vertical structure of the disk can be ignored we can derive a relatively simple evolution equation for the radial disturbance of the magnetic field

$$\left[\frac{k^2}{k_Z^2} D^4 + \kappa^2 D^2 - 4\Omega^2 (\boldsymbol{k} \cdot \boldsymbol{u_A})^2\right] \delta B_R = 0, \tag{2.61}$$

where we defined

$$D^2 = \frac{d^2}{dt^2} + (\boldsymbol{k} \cdot \boldsymbol{u_A})^2, \quad k^2 = k_R(t)^2 + \frac{m^2}{R^2} + k_Z^2. \tag{2.62}$$

It is interesting to note that Eq. (2.61) gives exactly Eq. (2.54) in the limit of vanishing m, once it is solved using standard WKB methods. Its physical meaning may be more easily understood once we consider the plane $(k/k_Z, (\boldsymbol{k} \cdot \boldsymbol{u_A})^2)$ in Fig. 2.6. Starting from a disturbance of coordinate $(k/k_Z, \boldsymbol{k} \cdot \boldsymbol{u_A})$, the shear will cause the ratio k/k_Z to decrease with time, reach a value near unity and then increase again. If $(\boldsymbol{k} \cdot \boldsymbol{u_A})^2 < -d\Omega^2/d \ln R$, a finite portion of time is spent by the system in an unstable region, and substantial growth can occur.
The maximum growth rate for a weak azimuthal field turns out to be $1/2|d\Omega/d \ln R|$, which is precisely the value corresponding to the instability in presence of a weak vertical field. The difference is that it is reached at much higher vertical wave numbers, in particular only if the following scaling holds

$$m \gg Rk_R \gg Rk_Z. \tag{2.63}$$

This relation essentially makes Eq. (2.61) approach an axisymmetric form, and the role of m is just to provide a coupling between the perturbation and the azimuthal field.

2.3. Mean-field dynamo in accretion disks

In the last part of this chapter devoted to the exploration of some of the most important physical phenomena relevant to the dynamics of an accretion disk, we briefly introduce the classical theory of *mean-field dynamo*. This topic has become quite important in the last decades, since its goal is to try to ultimately explain the origin and amplification of magnetic fields in differentially rotating fluids. We will discuss the core mechanism, which is at the base of this theory, in the non-relativistic regime and show its importance in an astrophysical context, following the description of Moffatt (1978a) and leaving the generalization to a general relativistic frame to Chapter 3. Finally, we discuss the recent implementation of this new *ingredient* in our numerical code and the results from a preliminary application in magnetized thick disks in Chapter 4.

2.3.1. Classical laminar dynamo theory

Let us consider a non-relativistic resistive plasma, whose e.m. fields evolve according to the induction equation and Ohm's law described respectively by Eq. (2.39) and Eq. (2.38), and let us define the magnetic energy contained in a fixed volume $\mathcal{V}$ as

$$M(t) = \frac{1}{2}\int_{\mathcal{V}} B^2 \mathrm{d}\mathcal{V}. \tag{2.64}$$

The time evolution of M is set by

$$\frac{\mathrm{d}}{\mathrm{d}t}\int_{\mathcal{V}} \frac{B^2}{2}\mathrm{d}\mathcal{V} = -\int_{\mathcal{V}} \boldsymbol{v}\cdot(\boldsymbol{J}\times\boldsymbol{B})\mathrm{d}\mathcal{V} - \int_{\mathcal{V}} \eta_B J^2 \mathrm{d}\mathcal{V} - \int_{\mathcal{S}} (\boldsymbol{E}\times\boldsymbol{B})\cdot\mathrm{d}\boldsymbol{\mathcal{S}}, \tag{2.65}$$

where $\mathcal{S}$ is the surface that contains the volume $\mathcal{V}$. Eq. (2.65) shows that the magnetic energy of a system can increase if work *against* the Lorentz force (first term on the right-hand side) is made, so to counteract the losses by ohmic dissipation (second term) and radiation through the system boudnaries (third term). To understand the source of the first term, we take Eq. (2.41) (neglecting the external gravity field and the viscosity terms), multiply it by $\boldsymbol{v}$ and obtain (after some manipulations)

$$\frac{\mathrm{d}}{\mathrm{d}t}\int_{\mathcal{V}} \frac{1}{2}\rho v^2 \mathrm{d}\mathcal{V} = \int_{\mathcal{V}} p\boldsymbol{\nabla}\cdot\boldsymbol{v}\mathrm{d}\mathcal{V} + \int_{\mathcal{V}} \boldsymbol{v}\cdot(\boldsymbol{J}\times\boldsymbol{B})\mathrm{d}\mathcal{V}, \tag{2.66}$$

from which it becomes clear that the amplification of magnetic energy is sustained by a decrease of kinetic energy, with no net energy loss for the whole system. Without such a mechanism, the magnetic field will still be affected by ohmic dissipation, which will lead to a magnetic decay on a time scale $\tau_d = L^2/\eta_B$,

where L is the characteristic macroscopic length scale of the volume $\mathcal{V}$. The velocity field is instead said to be *acting as a dynamo* if $M(t) \not\to 0$ for $t \to \infty$, i.e. if it is capable of efficiently converting kinetic energy into magnetic energy. In accretion disks the ultimate source of energy is of course the gravitational potential, which is then converted into orbital and turbulent kinetic energy.
One of the problems encountered in the search for an efficient dynamo mechanism is described by the *Cowling anti-dynamo theorem* (Cowling, 1976):

No axisymmetric magnetic field can be maintained stationarily through the dynamo action of axisymmetric currents.

This theorem precludes the possibility of self-sustaining axisymmetric dynamos, and it was elegantly illustrated by Boyd and Sanderson (2003) in the following way. Consider a fluid with velocity $\boldsymbol{v}$ and magnetic field $\boldsymbol{B}$ whose field lines are contained in a meridional plane that intersects the rotational axis. In any of the possible planes they will be closed lines containing at least a point where the magnetic field vanishes. We denote with $\mathcal{C}$ the curve that goes through all meridional planes and connects all points where $\boldsymbol{B}$ vanishes. If we integrate Ohm's law along this curve we get

$$\begin{aligned} \eta \oint_{\mathcal{C}} \boldsymbol{J} \cdot \mathrm{d}\boldsymbol{l} &= \oint_{\mathcal{C}} \boldsymbol{E} \cdot \mathrm{d}\boldsymbol{l} + \oint_{\mathcal{C}} (\boldsymbol{v} \times \boldsymbol{B}) \cdot \mathrm{d}\boldsymbol{l} \\ &= \int_{\mathcal{S}_{\mathcal{C}}} (\boldsymbol{\nabla} \times \boldsymbol{E}) \cdot \mathrm{d}\boldsymbol{\mathcal{S}} = - \int_{\mathcal{S}_{\mathcal{C}}} \frac{\partial \boldsymbol{B}}{\partial t} \cdot \mathrm{d}\boldsymbol{\mathcal{S}} = 0, \end{aligned} \tag{2.67}$$

where $\mathcal{S}_{\mathcal{C}}$ is an arbitrary open surface based on $\mathcal{C}$. The integral of the convective term turns out to be zero due to the vanishing magnetic field on $\mathcal{C}$, while the last equality comes from the assumption of stationarity. Eq. (2.67) tells us that there cannot be azimuthal currents, in clear contradiction with Ampere's law $\boldsymbol{J} = \boldsymbol{\nabla} \times \boldsymbol{B}$. If we also consider the presence of azimuthal fields, then we will still have no contribution from the convective term, since this time $\boldsymbol{B}$ and $\mathrm{d}\boldsymbol{l}$ will be parallel. Hence the theorem's thesis is demonstrated.
To better visualize what prevents the onset of a stable axisymmetric dynamo, let us decompose the fields in their *poloidal* and *toroidal* components (which respectively correspond to the meridional and azimuthal components in the case of a rotating system)

$$\boldsymbol{v} = \boldsymbol{v}_P + \boldsymbol{v}_T, \tag{2.68}$$

$$\boldsymbol{B} = \boldsymbol{B}_P + \boldsymbol{B}_T, \tag{2.69}$$

and let us also introduce the vector potential $\boldsymbol{A}$ likewise decomposed as $\boldsymbol{A} = \boldsymbol{A}_P + \boldsymbol{A}_T$, so that

$$\boldsymbol{B}_P = \boldsymbol{\nabla} \times \boldsymbol{A}_T. \tag{2.70}$$

Using the fact that $\boldsymbol{v}_T \times \boldsymbol{B}_T = 0$, we can rewrite the poloidal component of the induction equation as

$$\partial \boldsymbol{B}_P/\partial t = \boldsymbol{\nabla} \times (\boldsymbol{v}_P \times \boldsymbol{B}_P) + \eta_B \nabla^2 \boldsymbol{B}_P, \tag{2.71}$$

and with the help of Eq. (2.70) we can express it in terms of the toroidal component of the vector potential

$$\partial \boldsymbol{A}_T/\partial t = \boldsymbol{v}_P \times (\boldsymbol{\nabla} \times \boldsymbol{A}_T) + \eta_B \nabla^2 \boldsymbol{A}_T. \tag{2.72}$$

In a similar way we can obtain an expression for the evolution of the toroidal magnetic field

$$\partial \boldsymbol{B}_T/\partial t = \boldsymbol{\nabla} \times (\boldsymbol{v}_P \times \boldsymbol{B}_T + \boldsymbol{v}_T \times \boldsymbol{B}_P) + \eta_B \nabla^2 \boldsymbol{B}_T. \tag{2.73}$$

We now introduce standard cylindrical coordinates (R, ϕ, z) and set (in axisymmetry)

$$\boldsymbol{A}_T = A(R,z)\boldsymbol{i}_\phi, \tag{2.74}$$
$$\boldsymbol{B}_T = B(R,z)\boldsymbol{i}_\phi, \tag{2.75}$$
$$\boldsymbol{v}_T = v(R,z)\boldsymbol{i}_\phi, \tag{2.76}$$

from which we obtain with some vector identities

$$\nabla^2 \boldsymbol{A}_T = \boldsymbol{i}_\phi(\nabla^2 - R^{-2})A, \tag{2.77}$$
$$\boldsymbol{v}_P \times (\boldsymbol{\nabla} \times \boldsymbol{A}_T) = -R^{-1}(\boldsymbol{v}_P \cdot \boldsymbol{\nabla})RA. \tag{2.78}$$

If we insert these relations into Eq. (2.72) and Eq. (2.73) we finally get

$$\partial A/\partial t + R^{-1}(\boldsymbol{U}_P \cdot \boldsymbol{\nabla})RA = \eta_B(\nabla^2 - R^{-2})A, \tag{2.79}$$
$$\partial B/\partial t + R(\boldsymbol{U}_P \cdot \boldsymbol{\nabla})(R^{-1}B) = R(\boldsymbol{B}_P \cdot \boldsymbol{\nabla})\Omega + \eta_B(\nabla^2 - R^{-2})B, \tag{2.80}$$

where $\Omega(R,z) = R^{-1}U(R,z)$ is the fluid angular velocity. The first term on the right-hand side of Eq. (2.80) shows that a variation of Ω along a flux line of $\boldsymbol{B}_P$ leads, by distortion of the field lines, to the generation of a toroidal field: this is the so-called Ω-*effect*. It represents a fundamental ingredient of the dynamics of differentially rotating magnetized plasmas. On the other hand we notice that Eq. (2.79) does not present an analogous source term: $\boldsymbol{A}_T$ is just damped by the diffusive term on the right-hand side, and consequently the poloidal magnetic field can do nothing but eventually vanish due to ohmic diffusion. But if the ultimate destiny of $\boldsymbol{B}_P$ is to disappear, then $\boldsymbol{B}_T$ shares the same fate, since the Ω-effect relies on a steady reservoir of poloidal field to generate a toroidal one through shearing. To have a steady dynamo it is necessary to provide a mechanism that can close the so-called *dynamo cycle*, i.e. that can assure amplification of both toroidal and poloidal magnetic field against the action of diffusive processes.

2.3.2. Turbulent mean-field dynamo theory

Instead of assuming $\boldsymbol{v}$ to be a known function of time and space, let us consider the case where the velocity field has a stochastic component, whose instantaneous properties are just too complex to be appropriately captured. This describes for instance the case of turbulent motions triggered by instabilities in astrophysical plasmas.
We call l_0 and L respectively the typical length-scale of the stochastic motions and the global scale we are interested in, so that on an intermediate scale a

$$l_0 \ll a \ll L, \tag{2.81}$$

the properly averaged *global* variables can be considered constant. The averages can be defined for instance as a mean over a sphere of radius a, leading for any arbitrary quantity $\psi(\boldsymbol{x}, t)$ to the expression

$$\langle \psi(\boldsymbol{x}, t) \rangle_a = \frac{3}{4\pi a^3} \int_{|\boldsymbol{\xi}|<a} \psi(\boldsymbol{x} + \boldsymbol{\xi}, t) d\boldsymbol{\xi}, \tag{2.82}$$

where this mean value is not expected to depend on the particular value of a. We can now decompose the velocity field and magnetic field into their mean and variable (on small-scales) components

$$\boldsymbol{v}(\boldsymbol{x}, t) = \boldsymbol{U}_0(\boldsymbol{x}, t) + \boldsymbol{u}(\boldsymbol{x}, t), \tag{2.83}$$
$$\boldsymbol{B}(\boldsymbol{x}, t) = \boldsymbol{B}_0(\boldsymbol{x}, t) + \boldsymbol{b}(\boldsymbol{x}, t), \tag{2.84}$$

where both $\boldsymbol{u}$ and $\boldsymbol{b}$ have a vanishing mean by definition. If we substitute these expressions in the induction equation we obtain two evolution equations, for the mean magnetic field and its stochastic component respectively

$$\partial \boldsymbol{B}_0/\partial t = \boldsymbol{\nabla} \times (\boldsymbol{U}_0 \times \boldsymbol{B}_0) + \boldsymbol{\nabla} \times \boldsymbol{\mathcal{E}} + \eta_B \nabla^2 \boldsymbol{B}_0, \tag{2.85}$$
$$\partial \boldsymbol{b}/\partial t = \boldsymbol{\nabla} \times (\boldsymbol{U}_0 \times \boldsymbol{b}) + \boldsymbol{\nabla} \times (\boldsymbol{u} \times \boldsymbol{B}_0) + \boldsymbol{\nabla} \times \boldsymbol{\mathcal{G}} + \eta_B \nabla^2 \boldsymbol{b}, \tag{2.86}$$

where we defined

$$\boldsymbol{\mathcal{E}} = \langle \boldsymbol{u} \times \boldsymbol{b} \rangle, \tag{2.87}$$
$$\boldsymbol{\mathcal{G}} = \boldsymbol{u} \times \boldsymbol{b} - \langle \boldsymbol{u} \times \boldsymbol{b} \rangle. \tag{2.88}$$

It is clear from Eq. (2.85) that small-scale fluctuations can contribute to the evolution of $\boldsymbol{B}_0$, since they introduce a large-scale electromotive force $\boldsymbol{\mathcal{E}}$ that can in general deeply affect the behavior of the mean large-scale magnetic field.
To proceed further in the study of a mean-field dynamo, it is necessary to express $\mathcal{E}$ in terms of known quantities, i.e. the mean fields $\boldsymbol{B}_0$, and $\boldsymbol{U}_0$ and the statistical properties of the fluctuations (which will be assumed). If we consider Eq. (2.86) and assume $\boldsymbol{b}(\boldsymbol{x}, 0) = 0$, the field $\boldsymbol{b}$ is linear in $\boldsymbol{B}_0$ through the source term

$\boldsymbol{\nabla} \times (\boldsymbol{u} \times \boldsymbol{B}_0)$, while $\boldsymbol{B}_0$ is linear in $\boldsymbol{b}$ through the e.m.f. term $\boldsymbol{\nabla} \times \boldsymbol{\mathcal{E}}$. Since we assumed that the mean fields vary on length-scales much larger than the one on which averages are calculated, it is possible to express $\mathcal{E}$ in terms of $\boldsymbol{B}_0$ with the series expansion

$$\mathcal{E}_i = \alpha_{ij} B_{0j} + \beta_{ijk} \frac{\partial B_{0j}}{\partial x_k} + \gamma_{ijkl} \frac{\partial^2 B_{0j}}{\partial x_k \partial x_l} + \dots . \tag{2.89}$$

The coefficients $\alpha_{ij}, \beta_{ijk}, \dots$ will in general depend on the mean field $\boldsymbol{U}_0$, the resistivity η, and the statistical properties of $\boldsymbol{u}(\boldsymbol{x}, t)$, since $\boldsymbol{b}$ depends also on the coefficients via Eq. (2.86). However, in the limit of $L/l_0 \to \infty$, the coefficients will reduce to strictly uniform quantities, since $\boldsymbol{U}_0$ becomes uniform and $\boldsymbol{u}$ statistically homogeneous.
Let us consider the dominant term in Eq. (2.89), i.e.

$$\mathcal{E}_i^{(0)} = \alpha_{ij} B_{0j}. \tag{2.90}$$

Tensor α_{ij}, which is uniform as long as $\boldsymbol{u}$ is homogeneous, can be decomposed in its symmetric and antisymmetric part as $\alpha_{ij} = \alpha_{ij}^{(s)} - \epsilon_{ijk} a_k$, where $a_k = -\frac{1}{2} \epsilon_{ijk} \alpha_{ij}$ and ϵ_{ijk} is the Levi-Civita antisymmetric symbol. If we insert this expression for α_{ij} into Eq. (2.89) we obtain

$$\mathcal{E}_i^{(0)} = \alpha_{ij}^{(s)} B_{0j} + (\boldsymbol{a} \times \boldsymbol{B}_0)_i. \tag{2.91}$$

The effect of the antisymmetric component $\boldsymbol{a}$ is to introduce a correction to the mean flow velocity $\boldsymbol{U}_0$ and lead to an *effective velocity* $\boldsymbol{U}_0 + \boldsymbol{a}$. However, this contribution can usually be neglected in the situations of interest for us. To better understand the role of the symmetric component $\alpha_{ij}^{(s)}$, let us assume $\boldsymbol{u}$ to be isotropic and homogeneous. In this case also α_{ij} is isotropic, hence we can set

$$\alpha_{ij} = \alpha \delta_{ij}, \tag{2.92}$$

$$\boldsymbol{a} = 0, \tag{2.93}$$

where the scalar α derives from the statistical properties of the velocity fluctuations. Inserting Eq. (2.92) into Eq. (2.90) we obtain the simple relation

$$\boldsymbol{\mathcal{E}}^{(0)} = \alpha \boldsymbol{B}_0, \tag{2.94}$$

which inserted into Ohm's law (2.38) leads to a contribution to the current density equal to

$$\boldsymbol{J}^{(0)} = \frac{1}{\eta} \boldsymbol{\mathcal{E}}^{(0)} = \frac{\alpha}{\eta} \boldsymbol{B}_0. \tag{2.95}$$

The presence of α introduces an electric current *parallel* to the mean magnetic field, which is in strong contrast with the usual situation where the induction current $(\boldsymbol{U} \times \boldsymbol{B})/\eta$ is perpendicular to the magnetic field.

This phenomenon, known in the literature as α-*effect*, is at the core of the mean-field dynamo theory. It provides a way to close a dynamo cycle by generating poloidal magnetic fields starting from a toroidal field $\boldsymbol{B}_T$. In fact, such a field would lead, according to Eq. (2.95), to a toroidal current, which consequently would generate a poloidal magnetic component $\boldsymbol{B}_T$. The latter then allows the amplification of $\boldsymbol{B}_T$ through the Ω-effect, i.e. in presence of differential rotation. In such a system, called $\alpha - \Omega$ dynamo, the cycle $\boldsymbol{B}_P \leftrightarrows \boldsymbol{B}_T$ is closed and it is possible to have a steady amplification of magnetic field. The individual efficiency of the α-effect and the Ω-effect in generating magnetic field against dissipation can be estimated a priori by their relative *dynamo numbers*. This parameters (widely used in the literature) are defined as (Brandenburg and Subramanian, 2005)

$$C_\alpha = \frac{\alpha L}{\eta}, \tag{2.96}$$

$$C_\Omega = \frac{\Delta\Omega L^2}{\eta}. \tag{2.97}$$

They represent an estimate of the ratio between the source terms that result from the α-effect and the differential rotation and the dissipation due to a finite resistivity η.
It can be shown (Priest, 2014) that by neglecting the non-linear terms in Eq. (2.86) we can retrieve an analytical expression for α in terms of the velocity fluctuations, i.e.

$$\alpha = -\frac{1}{3}\tau\langle \boldsymbol{u} \cdot \boldsymbol{\nabla} \times \boldsymbol{u}\rangle, \tag{2.98}$$

where τ is the correlation time of the turbulent motions and $\langle \boldsymbol{u} \cdot \boldsymbol{\nabla} \times \boldsymbol{u}\rangle$ is the kinetic helicity of the fluid. Since the latter is essentially a measure of how entangled the turbulent flow is, Eq. (2.98) shows that the α-effect relies on the presence of asymmetries in the turbulent motions, and in particular it implies that the sign of α changes when crossing the equatorial plane of a rotating fluid.
We consider now the second term of Eq. (2.89)

$$\mathcal{E}_i^{(1)} = \beta_{ijk}\partial B_{0j}/\partial x_k. \tag{2.99}$$

Assuming an isotropic field $\boldsymbol{u}$, the coefficient β_{ijk} is also isotropic, i.e.

$$\beta_{ijk} = \beta\epsilon_{ijk}, \tag{2.100}$$

where β is a scalar. Inserting this expression into Eq. (2.99) we obtain for the induced e.m.f.

$$\boldsymbol{\mathcal{E}}^{(1)} = -\beta\boldsymbol{\nabla} \times \boldsymbol{B}_0 = -\beta\boldsymbol{J}_0, \tag{2.101}$$

where $\beta\boldsymbol{J}_0$ is the mean current density. This result leads to a contribution in the induction equation for the mean magnetic field equal to

$$\boldsymbol{\nabla} \times \boldsymbol{\mathcal{E}}^{(1)} = \beta\nabla^2\boldsymbol{B}_0, \tag{2.102}$$

where it is evident from a comparison with Eq. (2.85) that the effect of the induced e.m.f $\boldsymbol{\mathcal{E}}^{(1)}$ is to enhance the effective value of the magnetic resistivity η_B to $\tilde{\eta} = \eta_B + \beta$. This phenomenon describes the *turbulent resistivity*: magnetic field lines with opposite polarities are entangled by turbulent motions, which leads to their diffusion and consequently to a decrease of the mean field.
The final form of the induction equation with the inclusion of the α-effect and turbulent resistivity reads

$$\partial \boldsymbol{B}_0/\partial t = \boldsymbol{\nabla} \times (\boldsymbol{U}_0 \times \boldsymbol{B}_0) + \boldsymbol{\nabla} \times \boldsymbol{\mathcal{E}} + \eta_B \nabla^2 \boldsymbol{B}_0, \tag{2.103}$$

where

$$\boldsymbol{\mathcal{E}} = \alpha \boldsymbol{B} - \beta \boldsymbol{\nabla} \times \boldsymbol{B}. \tag{2.104}$$

Eq. (2.103) can be also reformulated in terms of an effective large scale electric field $\boldsymbol{E}_0$ as

$$\partial \boldsymbol{B}_0/\partial t = -c \boldsymbol{\nabla} \times \boldsymbol{E}_0, \tag{2.105}$$

once we replace the standard Ohm's law for a resistive plasma

$$\boldsymbol{E_0} = -\frac{\boldsymbol{U}_0}{c} \times \boldsymbol{B_0} + \frac{4\pi}{c^2} \eta_B \boldsymbol{J}_0, \tag{2.106}$$

with

$$\boldsymbol{E_0} = -\frac{\boldsymbol{U}_0}{c} \times \boldsymbol{B_0} + \frac{4\pi}{c^2} \tilde{\eta} \boldsymbol{J}_0 - \alpha \boldsymbol{B}_0, \tag{2.107}$$

where $\boldsymbol{J}_0 = c/4\pi \boldsymbol{\nabla} \times \boldsymbol{B}_0$. Eq. (2.107) will be an essential ingredient for the inclusion in the ideal GRMHD framework of resistivity and mean-field dynamo effects, as explained in detail in Chapter 3.

3. GRMHD

Since our goal is to describe the evolution of a magnetized plasma in a spacetime deeply warped by the gravity of a massive black hole, it is necessary to introduce the magnetohydrodynamics equations in covariant form. Once the fundamental GRMHD equations are known, we will use them to construct the disk model considered in our simulations as initial condition, i.e. a stationary magnetized torus orbiting around a black hole. In the following we will assume a spacetime metric with signature $(-,+,+,+)$ and we will use the greek letters μ, ν, λ, ...(which run from 0 to 3) for the tensor and vector components in the 4D spacetime, while the latin letters i, j, k, ...(which run from 1 to 3) will label the tensor and vector components in the 3D space. Moreover, we will set $c = G = 1$ and make use of the Lorentz-Heaviside notation for the electromagnetic quantities, i.e. absorbing the factor $\sqrt{4\pi}$ within the definition of the electric and magnetic field.

3.1. Covariant formalism

Following the treatment of Del Zanna et al. (2007) we consider an ideal fluid interacting with an electromagnetic field. The equations for conservation of mass and momentum-energy are respectively

$$\nabla_\mu(\rho u^\mu) = 0, \tag{3.1}$$

$$\nabla_\mu T^{\mu\nu} = 0, \tag{3.2}$$

where ∇_μ is the spacetime covariant derivative, ρ is the rest mass density measured in the Lagrangian frame comoving with the fluid four-velocity u^μ, and $T^{\mu\nu}$ is the stress-energy tensor. The latter is composed of two terms $T^{\mu\nu} = T^{\mu\nu}_m + T^{\mu\nu}_{em}$ due respectively to the matter distribution

$$T^{\mu\nu}_m = \rho h u^\mu u^\nu + p g^{\mu\nu}, \tag{3.3}$$

and the electromagnetic field

$$T^{\mu\nu}_{em} = F^\mu_{\ \lambda} F^{\nu\lambda} - \frac{1}{4}(F^{\lambda\kappa}F_{\lambda\kappa})g^{\mu\nu}. \tag{3.4}$$

In the previous expressions we find the spacetime metric tensor $g^{\mu\nu}$, the specific enthalpy $h = 1 + \epsilon + p/\rho$, the specific internal energy ϵ, the thermal pressure p and the electromagnetic field (or Faraday's) tensor $F^{\mu\nu}$. It is interesting to notice that the individual components are not conserved in general

$$\nabla_\mu T^{\mu\nu}_m = -\nabla_\mu T^{\mu\nu}_{em} = -I_\mu F^{\mu\nu}, \tag{3.5}$$

where I_μ is the four-current density and the last term is the electromagnetic force acting on the conducting fluid. Concerning the electromagnetic field, Maxwell equations in covariant form are given by

$$\nabla_\mu F^{\mu\nu} = -I_\nu, \tag{3.6}$$
$$\nabla_\mu F^{*\mu\nu} = 0, \tag{3.7}$$

where $F^{*\mu\nu} = \frac{1}{2}\epsilon^{\mu\nu\lambda\kappa}F_{\lambda\kappa}$ is the dual of the Faraday tensor, $\epsilon^{\mu\nu\lambda\kappa} = (-g)^{-1/2}[\mu\nu\lambda\kappa]$ is the Levi-Civita tensorial density, $g = \det\{g_{\mu\nu}\}$, and $[\mu\nu\lambda\kappa]$ is the completely antisymmetric symbol with convention $[0123] = +1$.
Once an equation of state $p = p(\rho, \epsilon)$ is chosen the system of GRMHD equations can be closed by selecting an appropriate form for Ohm's law, i.e. a relation between the four-current and the electromagnetic fields.

3.2. 3+1 Formalism

Despite its elegance and compactness, the covariant formalism is not well suited for a straightforward implementation in numerical codes. The main reason is the equal treatment of spatial and temporal variables, while standard computations in MHD require a separate time-integration along with a discretization of the spatial derivatives. It is therefore necessary to explicitly express the time-derivatives by adopting the so-called *3+1 decomposition* of the GRMHD equations (for a detailed and more complete derivation see Alcubierre (2008)).
In this formalism the 4-dimensional spacetime is foliated in time-like, non-intersecting hyper-surfaces Σ_t, defined as the iso-surfaces of a time scalar function t. We denote as

$$n_\mu = -\alpha\nabla_\mu t, \tag{3.8}$$

the time-like four-vector normal to the hyper-surface Σ_t pointing in direction of the future, where α is called *lapse function*. The observer moving with four-velocity n^μ is called *Eulerian* and all the quantities can be expressed in the corresponding frame of reference. If we consider any given vector (or tensor) V^μ, we can always decompose it in its temporal and spatial components

$$V^{\hat{n}} = -n_\mu V^\mu, \tag{3.9}$$
$$\perp V^\mu = (g^\mu_\nu + n^\mu n_\nu)V^\nu, \tag{3.10}$$

where we introduced the spatial projection operator $\perp \equiv g^{\mu}_{\nu} + n^{\mu}n_{\nu}$. If we apply $\perp$ to the metric tensor $g^{\mu\nu}$ we obtain the spatial metric $\gamma_{\mu\nu}$ induced on Σ_t by the 4-dimensional metric

$$\gamma_{\mu\nu} = \perp g_{\mu\nu} = g_{\mu\nu} + n_{\mu}n_{\nu}, \tag{3.11}$$

and we can identify the projection operator also as $\perp \equiv \perp^{\mu}_{\nu} = \gamma^{\mu}_{\nu}$.
We now introduce a coordinate system $x^{\mu} = (t, x^i)$ which adapts to the foliation Σ_t. Then it is possible to express the line element in the so-called *ADM form* (Arnowitt et al., 1962)

$$ds^2 = -\alpha^2 dt^2 + \gamma_{ij}(dx^i + \beta^i dt)(dx^j + \beta^j dt), \tag{3.12}$$

where β^{μ} is referred to as *shift-vector*, which is an arbitrary spatial vector. In this coordinate system the components of the unit vector are

$$n_{\mu} = (-\alpha, 0_i), \tag{3.13}$$
$$n^{\mu} = (1/\alpha, -\beta^i/\alpha), \tag{3.14}$$

and any purely spatial vector (or tensor) V^{μ} will necessarily have a vanishing contravariant time component, i.e. $V^t = 0$, while the covariant time component will be given by $V_t = g_{\mu t}V^{\mu} = \beta_i V^i$, and will in general be different from zero. Also the gradient of the unit vector can be decomposed in time and space components

$$\nabla_{\mu} n_{\nu} = -K_{\mu\nu} - n_{\mu}a_{\nu}, \tag{3.15}$$

where $K_{\mu\nu}$ is *extrinsic curvature* of the metric (a symmetric spatial tensor), and a_{ν} is the acceleration of the Eulerian observer (also a spatial vector). It is then possible to demonstrate that (York, 1979)

$$a_{\nu} = n^{\mu}\nabla_{\mu} n_{\nu} = \perp \nabla_{\nu} \ln\alpha, \tag{3.16}$$

which will be a useful relation we will use in short.
We can now decompose all the quantities in the GRMHD equations into their time and space components

$$u^{\mu} = \Gamma n^{\mu} + \Gamma v^{\mu}, \tag{3.17}$$
$$T^{\mu\nu} = W^{\mu\nu} + S^{\mu}n^{\nu} + n^{\mu}S^{\nu} + Un^{\mu}n^{\nu}, \tag{3.18}$$
$$F^{\mu\nu} = n^{\mu}E^{\nu} - E^{\mu}n^{\nu} + \epsilon^{\mu\nu\lambda\kappa}B_{\lambda}n_{\kappa}, \tag{3.19}$$
$$F^{*\mu\nu} = n^{\mu}B^{\nu} - B^{\mu}n^{\nu} - \epsilon^{\mu\nu\lambda\kappa}E_{\lambda}n_{\kappa}, \tag{3.20}$$
$$I^{\mu} = qn^{\mu} + J^{\mu}, \tag{3.21}$$

where all the newly introduced vectors and tensors are purely spatial and correspond to the usual observables measurable in the 3-dimensional space by the Eulerian observer. In fact v^{μ} is the fluid velocity with Lorentz factor $\Gamma = u^{\hat{n}}$, so that

$$v^i = u^i/\Gamma + \beta^i/\alpha, \tag{3.22}$$
$$\Gamma = \alpha u^t = (1 - v^2)^{-1/2}, \tag{3.23}$$

with $v^2 = v_i v^i$ and where we used the normalization condition $u_\mu u^\mu = -1$. The decomposition of the stress-energy tensor instead provides the energy density $U = T^{\hat{n}\hat{n}}$, the momentum density $S^\mu =\perp T^{\hat{n}\mu}$, and the spatial stress tensor of the plasma $W^{\mu\nu} =\perp T^{\mu\nu}$. The electric and magnetic field spatial vectors are defined as $E^\mu = F^{\hat{n}\mu}$ and $B^\mu = F^{*\hat{n}\mu}$, so that their components are given by

$$E^i = \alpha F^{ti}, \tag{3.24}$$
$$B^i = \alpha F^{*ti}. \tag{3.25}$$

Finally we denote the electric charge density with q and the spatial conduction current with J^μ, measured once again in the frame of the Eulerian observer.
By applying the usual covariant derivation rules and splitting the time and space components of Eq. (3.1), Eq. (3.2), Eq. (3.6), and Eq. (3.7) we obtain the GRMHD equations in the following form

$$(-g)^{-1/2}\partial_\mu\left[(-g)^{1/2}\rho u^\mu\right] = 0, \tag{3.26a}$$
$$(-g)^{-1/2}\partial_\mu\left[(-g)^{1/2}T^\mu_{\ i}\right] = \tfrac{1}{2}T^{\mu\nu}\partial_i g_{\mu\nu}, \tag{3.26b}$$
$$(-g)^{-1/2}\partial_\mu\left[(-g)^{1/2}T^{\mu\nu}n_\nu\right] = T^{\mu\nu}\nabla_\mu n_\nu, \tag{3.26c}$$
$$(-g)^{-1/2}\partial_\mu\left[(-g)^{1/2}F^{*\mu i}\right] = 0, \tag{3.26d}$$
$$(-g)^{-1/2}\partial_\mu\left[(-g)^{1/2}F^{\mu i}\right] = q\beta^i/\alpha - J^i, \tag{3.26e}$$
$$(-g)^{-1/2}\partial_\mu\left[(-g)^{1/2}F^{*\mu t}\right] = 0, \tag{3.26f}$$
$$(-g)^{-1/2}\partial_\mu\left[(-g)^{1/2}F^{\mu t}\right] = -q/\alpha. \tag{3.26g}$$

To reformulate them in terms of purely 3D spatial quantities we have to use all the previous relations and decompose the source terms on the right-hand sides of Eq. (3.26b) and Eq. (3.26c) as

$$\tfrac{1}{2}T^{\mu\nu}\partial_j g_{\mu\nu} = \tfrac{1}{2}W^{ik}\partial_j\gamma_{ik} + \alpha^{-1}S_i\partial_j\beta^i - U\partial_j\ln\alpha, \tag{3.27}$$
$$T^{\mu\nu}\nabla_\mu n_\nu = -K_{ij}W^{ij} + S^j\partial_j\ln\alpha. \tag{3.28}$$

We finally introduce the *bold notation* to indicate 3D spatial vectors and define $\boldsymbol{\nabla} =\perp \nabla$ as the 3D covariant derivate operator for the metric γ_{ij}. The final form of the GRMHD equations reads

$$\gamma^{-1/2}\partial_t\left(\gamma^{1/2}D\right) + \boldsymbol{\nabla}\cdot(\alpha\boldsymbol{v}D - \boldsymbol{\beta}D) = 0, \tag{3.29a}$$
$$\gamma^{-1/2}\partial_t\left(\gamma^{1/2}\boldsymbol{S}\right) + \boldsymbol{\nabla}\cdot(\alpha\mathbb{W} - \boldsymbol{\beta}\boldsymbol{S}) = (\boldsymbol{\nabla}\boldsymbol{\beta})\cdot\boldsymbol{S} - U\boldsymbol{\nabla}\alpha, \tag{3.29b}$$
$$\gamma^{-1/2}\partial_t\left(\gamma^{1/2}U\right) + \boldsymbol{\nabla}\cdot(\alpha\boldsymbol{S} - \boldsymbol{\beta}U) = \alpha\mathbb{K}:\mathbb{W} - \boldsymbol{S}\cdot\boldsymbol{\nabla}\alpha, \tag{3.29c}$$
$$\gamma^{-1/2}\partial_t\left(\gamma^{1/2}\boldsymbol{B}\right) + \boldsymbol{\nabla}\times(\alpha\boldsymbol{E} + \boldsymbol{\beta}\times\boldsymbol{B}) = 0, \tag{3.29d}$$
$$\gamma^{-1/2}\partial_t\left(\gamma^{1/2}\boldsymbol{E}\right) + \boldsymbol{\nabla}\times(-\alpha\boldsymbol{B} + \boldsymbol{\beta}\times\boldsymbol{E}) = -(\alpha\boldsymbol{J} - q\boldsymbol{\beta}), \tag{3.29e}$$
$$\boldsymbol{\nabla}\cdot\boldsymbol{B} = 0, \tag{3.29f}$$
$$\boldsymbol{\nabla}\cdot\boldsymbol{E} = q, \tag{3.29g}$$

where $\mathbb{K}$ and $\mathbb{W}$ denote respectively the extrinsic curvature and the stress tensor, while $\gamma = det\{\gamma_{ij}\}$ is the determinant of the spatial metric tensor, related to the four-dimensional one by $(-g)^{1/2} = \alpha\gamma^{1/2}$.
Eq. (3.29a) describes the continuity equation for $D = \rho\Gamma$, i.e. the mass density measured by the Eulerian observer. Eq. (3.29b) is the momentum equation, containing the divergence of the stress tensor $\mathbb{W}$. Its last term with the lapse function gradient reduces to the usual gravitational force in the Newtonian limit. Eq. (3.29c) is the energy equation, where the extrinsic curvature can be expressed (assuming a stationary metric) in terms of the covariant derivatives of the shift vector components β^i (Alcubierre, 2008)

$$\alpha\mathbb{K} : \mathbb{W} = \tfrac{1}{2}W^{ik}\beta^j\partial_j\gamma_{ik} + W_i{}^j\partial_j\beta^i. \tag{3.30}$$

Eq. (3.29d) is the general relativistic extension of the induction equation, where the components of the curl operator are defined as

$$(\boldsymbol{a}\times\boldsymbol{b})^i = \epsilon^{ijk}a_j b_k. \tag{3.31}$$

It is important to notice that the 3D Levi-Civita tensorial density is given by $\epsilon^{ijk} = \epsilon^{\hat{n}\mu\nu\lambda}$, so that $\epsilon^{ijk} = \gamma^{-1/2}[ijk]$ and $\epsilon_{ijk} = \gamma^{1/2}[ijk]$ are implicitly defined through the induction equation. Similarly Eq. (3.29e) is the GR generalization of Ampere's law, containing additional contributions due to the curved metric in both the hyperbolic and the source terms. Finally, Eq. (3.29f) and Eq. (3.29g) are the usual constraints on the fields $\boldsymbol{B}$ and $\boldsymbol{E}$.
In absence of gravity the quantities related to the metric reduce to

$$\begin{aligned}
\alpha &= 1, &(3.32)\\
\boldsymbol{\beta} &= 0, &(3.33)\\
\mathbb{K} &= 0, &(3.34)\\
\partial_t\gamma &= 0, &(3.35)
\end{aligned}$$

and the system Eq. (3.29) will therefore describe the evolution of a plasma in a Minkowski spacetime.
The stress tensor, the momentum density, and the energy density can be expressed in terms of the fluid and electromagnetic quantities respectively as

$$\begin{aligned}
W^{ij} &= \rho h\Gamma^2 v^i v^j - E^iE^j - B^iB^j + \left[p + \tfrac{1}{2}\left(E^2+B^2\right)\right]\gamma^{ij}, &(3.36)\\
S^i &= \rho h\Gamma^2 v^i + \epsilon^{ijk}E_jB_k, &(3.37)\\
U &= \rho h\Gamma^2 - p + \tfrac{1}{2}\left(E^2+B^2\right). &(3.38)
\end{aligned}$$

Finally, it is important to remember that Eq. (3.29) describe the evolution in time of the *contravariant* components of the vectorial quantities. Whenever is necessary to recover information on the components of a spatial vector with contravariant components V^i projected on an orthonormal set of axis, assuming a

diagonal spatial metric, we can easily compute the *orthonormal components* defined as

$$V_{\hat{1}} = \sqrt{\gamma_{11}}\, V^1, \tag{3.39}$$
$$V_{\hat{2}} = \sqrt{\gamma_{22}}\, V^2, \tag{3.40}$$
$$V_{\hat{3}} = \sqrt{\gamma_{33}}\, V^3. \tag{3.41}$$

3.2.1. General relativistic Ohm's law

So far we computed the GRMHD equations without assuming any specific form for Ohm's law, which essentially encodes the information on how the conducting fluid reacts to the presence of an electric field (we will neglect possible effects due to polarization). Depending on the particular choice we will end up with a different relation between the electric field and other quantities such as the current density, the magnetic field, and the fluid velocity, which will be necessary to close the GRMHD system (once an EoS is also specified).
In order to achieve a covariant formulation of Ohm's law, it is convenient to consider the comoving frame of the fluid, where the intuition and interpretation of a generalization from the non-relativistic case should be easier (see Bucciantini et al. (2012)).
Let us consider the Faraday tensor and the four-current, and decompose both quantities in the frame comoving with the fluid four-velocity u^μ

$$F^{\mu\nu} = u^\mu e^\nu - e^\mu u^\nu + \epsilon^{\mu\nu\lambda\kappa} b_\lambda u_\kappa, \tag{3.42}$$
$$F^{*\mu\nu} = u^\mu b^\nu - b^\mu u^\nu - \epsilon^{\mu\nu\lambda\kappa} e_\lambda u_\kappa, \tag{3.43}$$
$$I^\mu = q_0 u^\mu + j^\mu, \tag{3.44}$$

where $e^\mu = F^{\mu\nu} u_\nu, b^\mu = F^{*\mu\nu} u_\nu, q_0 = -I^\mu u_\mu$, and j^μ are respectively the electric field, the magnetic field, the electric charge density, and the conducting current in this frame. We now further decompose the vectors in the comoving frame in the $3+1$ Eulerian foliation of spacetime

$$e^\mu = \Gamma(\boldsymbol{E}\cdot\boldsymbol{v}) n^\mu + \Gamma(E^\mu + \epsilon^{\mu\nu\lambda} v_\nu B_\lambda), \tag{3.45}$$
$$b^\mu = \Gamma(\boldsymbol{B}\cdot\boldsymbol{v}) n^\mu + \Gamma(B^\mu - \epsilon^{\mu\nu\lambda} v_\nu E_\lambda), \tag{3.46}$$
$$j^\mu = (q - q_0\Gamma) n^\mu + J^\mu - q_0 \Gamma v^\mu, \tag{3.47}$$

where $q_0 = \Gamma(q - \boldsymbol{J}\cdot\boldsymbol{v})$. At this point we are ready to choose a specific expression for Ohm's law among the following alternatives

1. **Ideal GRMHD**. For a perfectly conducting plasma the electric field in the comoving frame has to vanish, i.e. $e^\mu = 0$. Plugging this condition in Eq. (3.45) and projecting on the 3D space provides the well known relation

$$\boldsymbol{E} + \boldsymbol{v}\times\boldsymbol{B} = 0. \tag{3.48}$$

The physical meaning of Eq. (3.48) is that free charges in the plasma can effectively shield any electric field that may rise locally, while its mathematical consequence is to make Eq. (3.29e) redundant as dynamical equation, and reduce it to a simple relation between the magnetic field $\boldsymbol{B}$ and the current $\boldsymbol{J}$, just as in the non-relativistic case.

2. **Resistive GRMHD**. For a plasma with a finite conductivity the electric field in the comoving frame will be proportional to the conduction current, hence (Palenzuela et al., 2009)

$$e^\mu = \eta j^\mu, \tag{3.49}$$

where η represents the magnetic resistivity (assumed to be isotropic) measured in the comoving frame. Substituting once again this relation in Eq. (3.45), whose time projection will be

$$\Gamma(\boldsymbol{E}\cdot\boldsymbol{B}) = \eta(q - q_0\Gamma). \tag{3.50}$$

We then use Eq. (3.50) to express q_0 and eliminate it from the spatial projection of Eq. (3.45), obtaining

$$\Gamma[\boldsymbol{E} + \boldsymbol{v}\times\boldsymbol{B} - (\boldsymbol{E}\cdot\boldsymbol{v})\boldsymbol{v}] = \eta(\boldsymbol{J} - q\boldsymbol{v}). \tag{3.51}$$

For $\eta = 0$ we obtain the result for the ideal case, while for $|\boldsymbol{v}| \ll 1$ Eq. (3.51) reduces to the non-relativistic limit

$$\boldsymbol{E} + \boldsymbol{v}\times\boldsymbol{B} = \eta\boldsymbol{J}. \tag{3.52}$$

3. **Resistive GRMHD + Dynamo**. The natural extension of Ohm's law when including a mean-field dynamo effect (as introduced in Chapter 2), is to add a term proportional to the magnetic field (Bucciantini et al., 2012)

$$e^\mu = \eta j^\mu + \xi b^\mu. \tag{3.53}$$

The parameter ξ is defined as

$$\xi \equiv -\alpha_{\rm dyn}, \tag{3.54}$$

where $\alpha_{\rm dyn}$ represents the mean-field coefficient present in Eq. (2.104). This definition has been introduced to avoid ambiguity with the lapse function α, and the magnetic resistivity η now takes into account the turbulent resistivity introduced by the small-scale fluctuations (see Eq. (2.102)). As in the previous case we substitute Eq. (3.53) in Eq. (3.45), whose time projection gives

$$\Gamma(\boldsymbol{E}\cdot\boldsymbol{v}) = \eta(q - q_0\Gamma) + \xi\Gamma(\boldsymbol{B}\cdot\boldsymbol{v}). \tag{3.55}$$

From this relation we compute q_0, and eliminate it from the space projection of Eq. (3.45), which then reads

$$\Gamma[\boldsymbol{E}+\boldsymbol{v}\times\boldsymbol{B}-(\boldsymbol{E}\cdot\boldsymbol{v})\boldsymbol{v}]=\eta(\boldsymbol{J}-q\boldsymbol{v})+\xi\Gamma[\boldsymbol{B}-\boldsymbol{v}\times\boldsymbol{E}-(\boldsymbol{B}\cdot\boldsymbol{v})\boldsymbol{v}]. \quad (3.56)$$

This relation reduces to the resistive formulation in Eq. (3.51) when $\xi = 0$, and in the limit of small velocities it becomes

$$\boldsymbol{E}+\boldsymbol{v}\times\boldsymbol{B}=\eta\boldsymbol{J}+\xi\boldsymbol{B}. \quad (3.57)$$

It is interesting to note how all the examples we considered depend on the presence of a curved metric only through the scalar and vector products that involve the spatial metric γ_{ij}, while there is no explicit term involving α or β^i. In the non-relativistic regime of resistive MHD the displacement current can always be neglected, as the electrical charge density. This means that Ampere's law can be written as $\boldsymbol{J} = \boldsymbol{\nabla}\times\boldsymbol{B}$, which represents a relation to compute the current from the magnetic field.
In the relativistic regime the displacement current $\partial\boldsymbol{E}/\partial t$ is in general no longer negligible, therefore it becomes necessary to use Eq. (3.29e) to evolve the electric field under the constrained given by Eq. (3.29g). Ohm's law provides a way to express the spatial current density $\boldsymbol{J}$, while q is derived from Gauss theorem $q = \boldsymbol{\nabla}\cdot\boldsymbol{E}$.
In the most general case of a resistive plasma with mean-field dynamo effects, the electric field will evolve in time according to

$$\begin{aligned}\gamma^{-1/2}\partial_t\left(\gamma^{1/2}\boldsymbol{E}\right)-\boldsymbol{\nabla}\times(\alpha\boldsymbol{B}-\boldsymbol{\beta}\times\boldsymbol{E})+(\alpha\boldsymbol{v}-\boldsymbol{\beta})q=\\ -\alpha\Gamma[\boldsymbol{E}+\boldsymbol{v}\times\boldsymbol{B}-(\boldsymbol{E}\cdot\boldsymbol{v})\boldsymbol{v}]/\eta+\xi\alpha\Gamma[\boldsymbol{B}-\boldsymbol{v}\times\boldsymbol{E}-(\boldsymbol{B}\cdot\boldsymbol{v})\boldsymbol{v}]/\eta.\end{aligned} \quad (3.58)$$

When $\eta = 0$, the left-hand side of the equation can be neglected, i.e. no time-integration is required to retrieve the electric field at any given time (as it should be in the ideal GRMHD case), while for $\xi = \eta = 0$ we obtain, as expected, Ohm's law for an ideal plasma ($\boldsymbol{E} = -\boldsymbol{v}\times\boldsymbol{B}$).

3.3. Thick magnetized disks

We now present in more detail the analytical stationary solution for Eq. (3.29) which describes the model used in our simulations, i.e. a thick disk of magnetized plasma orbiting around a black hole (see Font and Daigne (2002); Komissarov (2006)). We will neither include in the analysis the self-gravity of the disk nor contributions due to viscous and radiative effects, but will focus on the external gravitational potential generated by the black hole and the support provided by both thermal and magnetic pressure in the disk.

3.3.1. Kerr spacetime

Let us consider a rotating black hole of mass M and angular momentum per unit of mass $a = J/M$, assuming both to be constant. In the Boyer-Lindquist coordinates (t, r, θ, ϕ) and in the ADM formalism, the spacetime line element can be expressed as

$$\mathrm{d}s^2 = g_{tt}\mathrm{d}t^2 + 2g_{t\phi}\mathrm{d}t\mathrm{d}\phi + g_{\phi\phi}\mathrm{d}\phi^2 + g_{rr}\mathrm{d}r^2 + g_{\theta\theta}\mathrm{d}\theta^2, \tag{3.59}$$

where the metric coefficients are given by

$$g_{tt} = -\left(1 - \frac{2Mr}{\varrho^2}\right), \tag{3.60}$$

$$g_{t\phi} = -\frac{2Mar\sin^2\theta}{\varrho^2}, \tag{3.61}$$

$$g_{rr} = \frac{\varrho^2}{\Delta}, \tag{3.62}$$

$$g_{\theta\theta} = \varrho^2, \tag{3.63}$$

$$g_{\phi\phi} = \frac{\Sigma^2}{\varrho^2}\sin^2\theta, \tag{3.64}$$

with the following definitions

$$\Delta \equiv r^2 - 2Mr + a^2, \tag{3.65}$$

$$\varrho^2 \equiv r^2 + a^2\cos^2\theta, \tag{3.66}$$

$$\Sigma^2 \equiv (r^2 + a^2)^2 - a^2\Delta\sin^2\theta. \tag{3.67}$$

In these equations it is important not to confuse the geometric factor ϱ with the mass density ρ. This solution of the Einstein field equations due to Kerr (1963) shows that the metric retains the stationary and axisymmetric character of the mass distribution that generates it, i.e. a rotating black hole with constant mass and spin.
It is interesting to note that when setting $c = G = 1$, M and a have both the dimension of a length. Furthermore, for the black hole spin we have $0 \leq a \leq M$. When $a = 0$, the stationary and spherically symmetric Schwarzschild metric of a non-rotating black hole results

$$\mathrm{d}s^2 = -\left(1 - \frac{2M}{r}\right)\mathrm{d}t^2 + \left(1 - \frac{2M}{r}\right)^{-1}\mathrm{d}r^2 + r^2\mathrm{d}\theta^2 + r^2\sin^2\theta\mathrm{d}\phi^2, \tag{3.68}$$

while $a = M$ corresponds to the case of a maximally rotating black hole. When $\Delta = 0$ the Kerr metric has two singularities given by the roots of Eq. (3.65)

$$r_\pm = M \pm (M^2 - a^2)^{1/2}, \tag{3.69}$$

where r_+ corresponds to the proper black hole event horizon r_h, that ranges between M and $2M$ depending on the value of a.
Let us now consider an external observer orbiting around the black hole with four-velocity $u^\mu = (u^t, 0, 0, u^\phi)$ and constant angular velocity

$$\Omega = \frac{u^\phi}{u^t}. \tag{3.70}$$

Exploiting the normalization constraint $u_\mu u^\mu = -1$ we get

$$g_{tt} + 2\Omega g_{t\phi} + \Omega^2 g_{\phi\phi} < 0, \tag{3.71}$$

i.e. the value of the observer's angular velocity lies within the interval $[\Omega_-, \Omega_+]$, where

$$\Omega_\pm = \frac{-g_{t\phi} \pm (g_{t\phi}^2 - g_{tt} g_{\phi\phi})^{1/2}}{g_{\phi\phi}} = \omega \pm \left(\omega^2 - \frac{g_{tt}}{g_{\phi\phi}}\right)^{1/2}, \tag{3.72}$$

and where we defined $\omega \equiv -g_{t\phi}/g_{\phi\phi}$. In those regions where $g_{tt} < 0$ the observer's angular velocity can be zero (since $\Omega_- < 0$), but where $g_{tt} > 0$ there will be a minimum value $\Omega_- > 0$ below which ω cannot drop. The observer that in other circumstances would be at rest will be dragged by the rotating spacetime with an angular velocity ω. Such a region is referred to as the *ergosphere*. It is limited by the surfaces where the coefficient g_{tt} is zero, i.e. at a distance from the black hole given by

$$r_0(\theta) = M + (M^2 - a^2 \cos^2\theta)^{1/2}, \tag{3.73}$$

which turns out to be external to the black hole event horizon r_h. In this region where $g_{tt} > 0$ it is possible to have particles with negative energy measured at infinity, since the latter is a motion constant defined by $\bar{E} = -p_t = -g_{t\mu} p^\mu$, with p^μ the four-momentum of the particle. Because of this property of the ergosphere and the existence of particle trajectories that can fall into the black hole with negative energy, it is in principle possible to extract energy from a Kerr black hole tapping its rotational energy through the *Penrose mechanism* (Penrose, 1969). The most plausible way to realize such a process is currently thought to be the Blandford-Znajek machanism (Blandford and Znajek, 1977), where the black hole rotational energy is extracted by the torques due to magnetic fields treading the ergosphere.
Considering the 3+1 decomposition and comparing Eq. (3.59) with Eq. (3.12) we can represent the corresponding 3D spatial metric tensor γ_{ij} as a diagonal matrix with coefficients

$$\gamma_{rr} = \frac{\varrho^2}{\Delta}, \quad \gamma_{\theta\theta} = \varrho^2, \quad \gamma_{\phi\phi} = \frac{\Sigma^2}{\varrho^2}\sin^2\theta, \tag{3.74}$$

while the shift vector and the lapse function are respectively given by

$$\boldsymbol{\beta} = \left(0, 0, -\frac{2Mar}{\Sigma^2}\right), \quad \alpha = \left(\frac{\varrho^2 \Delta}{\Sigma^2}\right)^{1/2}. \tag{3.75}$$

Finally we introduce the relativistic generalization of the distance from the black hole rotational axis

$$\mathcal{L}(r,\theta) = g_{t\phi}^2 - g_{tt}g_{\phi\phi} = \Delta \sin^2\theta, \tag{3.76}$$

which in the Newtonian limit simply gives $\mathcal{L} = r^2 \sin^2\theta$.

3.3.2. Stationary magnetized models

We study now an analytical stationary solution of the GRMHD equations that describes the disk model we will use in our simulations. Consider a magnetized perfect fluid orbing around a Kerr black hole with four-velocity $u^\mu = (u^t, 0, 0, u^\phi)$ in the positive ϕ-direction (corotating with the black hole) with positive angular momentum and rotation axis aligned with the black hole's spin. To calculate the plasma stress-energy tensor we need to consider both the hydrodynamic contribution Eq. (3.3) and the electromagnetic one Eq. (3.4). Limiting ourselves to the case of an ideal plasma, we set $e^\mu = 0$ in Eq. (3.43)) and obtain

$$F^{*\mu\nu} = u^\mu b^\nu - b^\mu u^\nu, \tag{3.77}$$

where $b^\mu = (b^t, 0, 0, b^\phi)$ is the four-vector of the magnetic field assumed to be spatially toroidal. We will see however in Chapter 5 that the general equilibrium structure of the disk in this case will be essentially the same as that of unmagnetized configurations (Abramowicz et al., 1978; Kozlowski et al., 1978).
Using Eq. (3.77) in Eq. (3.4) we get the final form of the total stress-energy tensor

$$T^{\mu\nu} = (w + b^2)u^\mu u^\nu + \left(p + \frac{b^2}{2}\right) g^{\mu\nu} - b^\mu b^\nu, \tag{3.78}$$

where $w = \rho h$ is the fluid enthalphy density. We now define the specific angular momentum of the fluid as $l = -u_\phi/u_t$, while its orbital velocity is given by Eq. (3.70). It is important to note that these quantities are consistent with their definitions in the Newtonian limit, respectively $l = r^2 \sin^2\theta\ \Omega$ and $\Omega = \mathrm{d}\phi/\mathrm{d}t$. Using the normalization constraint for the four-velocity u^μ and the fact that $u_\mu = g_{\mu\nu}u^\nu$ we can also express l and Ω in terms of each other

$$l = -\frac{g_{t\phi} + g_{\phi\phi}\Omega}{g_{tt} + g_{t\phi}\Omega}, \tag{3.79}$$

$$\Omega = -\frac{g_{t\phi} + g_{tt}l}{g_{\phi\phi} + g_{t\phi}l}. \tag{3.80}$$

Using Eq. (3.2) and contracting it with the projection operator $P^\mu_{\ \nu} = g^\mu_{\ \nu} + u^\mu u_\nu$ we obtain

$$(w + b^2)u_\nu \nabla_i u^\nu + \nabla_i \left(p + \frac{b^2}{2}\right) - b_\nu \nabla_i b^\nu = 0. \tag{3.81}$$

Exploiting the definitions of l and Ω, we finally derive the GRMHD generalization of the Euler equation

$$\nabla_i(\ln|u_t|) - \frac{\Omega}{1-\Omega l}\nabla_i l + \frac{\nabla_i p}{w} + \frac{\nabla_i(\mathcal{L}b^2)}{2\mathcal{L}w} = 0, \tag{3.82}$$

which determines the equilibrium of our stationary, axisymmetric system with u^μ and b^μ having purely toroidal spatial components, and where the index i represents either r or θ. In the limit of $b^2 \to 0$ we get

$$\nabla_i(\ln|u_t|) - \frac{\Omega}{1-\Omega l}\nabla_i l + \frac{\nabla_i p}{w} = 0, \tag{3.83}$$

which describes the equilibrium state of an unmagnetized plasma.
Assuming a barotropic equation of state $w = w(p)$ we can rewrite Eq. (3.82) as

$$\mathrm{d}\left(\ln(|u_t| + \int_o^p \frac{\mathrm{d}p}{w}\right) = \frac{\Omega}{1-\Omega l}\mathrm{d}l - \frac{\mathrm{d}(\mathcal{L}b^2)}{2\mathcal{L}w}. \tag{3.84}$$

In the case of an unmagnetized torus this equation implies that $\Omega = \Omega(l)$, which means that the surfaces of constant l and Ω coincide. They are called *von Zeipel cylinders* (Kozlowski et al., 1978). For a given spatial metric we can construct such surfaces for a certain value of angular velocity Ω_0 and angular momentum l_0 by the roots of

$$g_{tt}l_0 + g_{t\phi}(1 + \Omega_0 l_0) + g_{\phi\phi}\Omega_0 = 0. \tag{3.85}$$

Moreover, if the distribution of angular momentum is known in the equatorial plane $l(r, \theta = \pi/2) \equiv l_{\mathrm{eq}}(r)$, the corresponding profile of the angular velocity is

$$\Omega(r, \pi/2) \equiv \Omega_{\mathrm{eq}}(r) = -\frac{g_{t\phi}(r,\pi/2) + g_{tt}(r,\pi/2)l_{eq}(r)}{g_{\phi\phi}(r,\pi/2) + g_{t\phi}(r,\pi/2)l_{eq}(r)}. \tag{3.86}$$

Substituting this expression into Eq. (3.85) we obtain an equation for the von Zeipel cylinder that crosses the equatorial plane at a given radial distance r_0

$$\begin{aligned} &l^2(r_0)[g_{tt}(r,\theta)g_{t\phi}(r_0,\pi/2) - g_{t\phi}(r,\theta)g_{tt}(r_0,\pi/2)] \\ &+l(r_0)[g_{tt}(r,\theta)g_{\phi\phi}(r_0,\pi/2) - g_{\phi\phi}(r,\theta)g_{tt}(r_0,\pi/2)] \\ &\quad +[g_{t\phi}(r,\theta)g_{\phi\phi}(r_0,\pi/2) - g_{\phi\phi}(r,\theta)g_{t\phi}(r_0,\pi/2)] = 0. \end{aligned} \tag{3.87}$$

In the more general case of a magnetized plasma, we get (by assuming $\Omega = \Omega(l)$)

$$\mathrm{d}\left(\ln(|u_t| + \int_0^p \frac{\mathrm{d}p}{w} - \int_0^l \frac{\Omega \mathrm{d}l}{1-\Omega l}\right) = -\frac{\mathrm{d}(\mathcal{L}b^2)}{2\mathcal{L}w}. \tag{3.88}$$

where the right-hand side is now a total differential. We define then $\tilde{w} = \mathcal{L}w$ and $\tilde{p}_m = \mathcal{L}p_m$ (with $p_m = b^2/2$ the magnetic pressure) and integrate Eq. (3.88)

$$\ln|u_t| + \int_0^p \frac{\mathrm{d}p}{w} - \int_0^l \frac{\Omega \mathrm{d}l}{1-\Omega l} + \int_0^{\tilde{p}_m} \frac{\mathrm{d}\tilde{p}_m}{\tilde{w}} = K_D, \tag{3.89}$$

where the integration constant K_D is computed by assuming a vanishing thermal and magnetic pressure at the disk's inner edge, i.e. at $r = r_{\rm in}$

$$K_D = \ln|u_{t\rm in}| - \int_0^{l_{\rm in}} \frac{\Omega {\rm d}l}{1-\Omega l}. \tag{3.90}$$

with $u_{t\rm in} = u_t(r_{\rm in})$ and $l_{\rm in} = l(r_{\rm in})$. Using Eq. (3.90) in Eq. (3.89)) we get

$$\ln|u_t| - \ln|u_{t\rm in}| - \int_{l_{\rm in}}^{l} \frac{\Omega {\rm d}l}{1-\Omega l} + \int_0^p \frac{{\rm d}p}{w} + \int_0^{\tilde{p}_m} \frac{{\rm d}\tilde{p}_m}{\tilde{w}} = 0. \tag{3.91}$$

It is convenient to introduce the total potential W defined as

$$W = \ln|u_t| + \int_l^{l_\infty} \frac{\Omega {\rm d}l}{1-\Omega l}, \tag{3.92}$$

where l_∞ is the limiting value of the angular momentum for $r \to \infty$, which is supposed to be finite. Hence, $u_{t\infty} = -1$ and $W_\infty = 0$. In the Newtonianlimit, W reduces to the sum of gravitational and centrifugal potential.
With these definitions we can finally express Eq. (3.91) as

$$W - W_{\rm in} + \int_o^p \frac{{\rm d}p}{w} + \int_0^{\tilde{p}_m} \frac{{\rm d}\tilde{p}_m}{\tilde{w}} = 0. \tag{3.93}$$

Let us now consider the case of a barotropic disk with constant angular momentum, i.e.

$$l = l_0, \tag{3.94}$$
$$p = K w^\varkappa, \tag{3.95}$$
$$\tilde{p}_m = K_m \tilde{w}^\zeta, \tag{3.96}$$

which allows us to rewrite Eq. (3.93) as

$$W - W_{\rm in} + \frac{\varkappa}{\varkappa - 1}\frac{p}{w} + \frac{\zeta}{\zeta - 1}\frac{p_m}{w} = 0, \tag{3.97}$$

where

$$W = \ln|u_t|. \tag{3.98}$$

Using the normalization condition of u^μ, we can express u_t in terms of l_0

$$-u_t = \sqrt{\frac{\mathcal{L}}{g_{tt}l_0^2 + 2g_{t\phi}l_0 + g_{\phi\phi}}} \equiv \sqrt{\frac{\mathcal{L}}{\mathcal{A}}}, \tag{3.99}$$

with $\mathcal{A} \equiv l_0^2 g_{tt} + 2l_0 g_{t\phi +} g_{\phi\phi}$. Inserting Eq. (3.99) into Eq. (3.98) we finally express the potential as a simple function of the metric coefficients and l_0 only

$$W(r,\theta) = \frac{1}{2}\ln\left|\frac{\mathcal{L}}{\mathcal{A}}\right|. \tag{3.100}$$

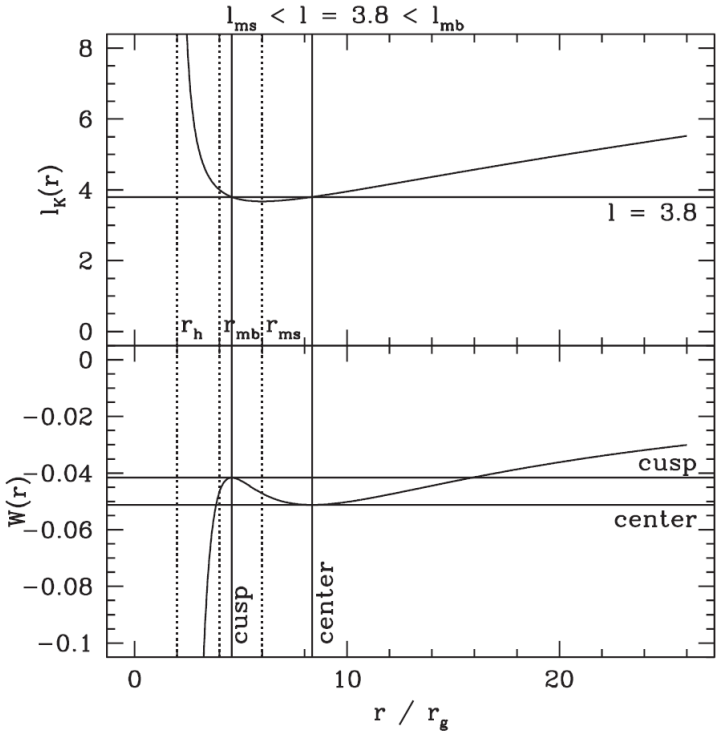

Figure 3.1.: Radial profiles of the Keplerian angular momentum $l_{\rm K}$ and the potential W on the equatorial plane $\theta = \pi/2$. (Font and Daigne, 2002)

This relation allows us to compute the total potential at any point of space for a given value of the angular momentum, while Eq. (3.97) represents the fundamental equation through which we will construct the whole magnetized disk. In the hydrodynamic case and for a non-constant distribution of angular momentum, once $l_{\rm eq}$ is known (and hence the von Zeipel cylinders specify l and Ω in the whole disk) it is possible to calculate the equipotential surfaces of $W(r,\theta)$ from Eq. (3.92).

Besides the parameters that so far characterize the model $(\varkappa, \zeta, l_0, W_{\rm in})$ two more are needed, namely the enthalpy w_c and the magnetization $\sigma_c \equiv p_m/p$ in a specific point of the disk that for symmetry reasons we take in the equatorial plane at a distance $r = r_c$.
From Eq. (3.97) we obtain the thermal pressure in the disk at the reference point

$$p_c = w_c(W_{\rm in} - W_c)\left(\frac{\varkappa}{\varkappa - 1} + \frac{\zeta}{\zeta - 1}\sigma_c\right)^{-1}, \tag{3.101}$$

and the magnetic pressure

$$p_{m_c} = \sigma_c p_c, \tag{3.102}$$

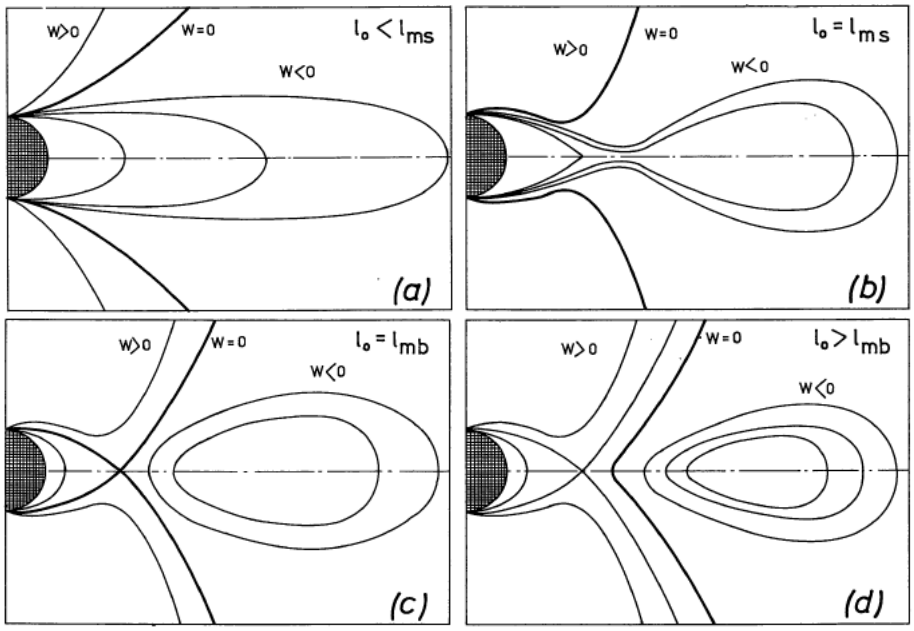

Figure 3.2.: Topology of the disk's equipotential surfaces for different values of l_0. (Abramowicz et al., 1978)

which we will use to calculate the proportionality constants of the barotropic relations

$$K = p_c/w_c^{\varkappa}, \tag{3.103}$$

$$K_m = \tilde{p}_c/\tilde{w}_c^{\zeta} = p_c/(\mathcal{L}^{\zeta-1}w_c^{\zeta}). \tag{3.104}$$

Following Abramowicz et al. (1978) we choose the so-called *disk's center* as reference point, i.e. the outer of the two points in the equatorial plane where l_0 equals the *Keplerian* angular momentum $l_{\rm K}$ (Fig. 3.1). To compute its value we replace into Eq. (3.79) the expression for the Keplerian angular velocity (Bardeen et al., 1972))

$$\Omega_{\rm K} = \pm\frac{M^{1/2}}{(r^{3/2} \pm aM^{1/2})}, \tag{3.105}$$

where the positive (negative) sign refers to prograde (retrograde) orbits. We get

$$l_{\rm K} = \frac{\pm(r^2 \mp 2ar^{1/2} + a^2)}{r^{3/2} - 2r^{1/2} \pm a}, \tag{3.106}$$

which we will use to infer the specific angular momentum of a disk with center at $r = r_c$. The other point where $l = l_{\rm K}$ is referred to as the *disk's cusp*. It is located at a distance $r_{\rm cusp} < r_c$ from the black hole.
The disk's surface, under the assumption of a barotropic EoS, is completely determined by the value of $W_{\rm in}$. It is also possible to demonstrate that the disk will be disconnected from the event horizon only if $|l_0| > |l_{\rm ms}|$ (Abramowicz et al., 1978),

where $l_{\rm ms}$ is the specific angular momentum at the marginally stable Keplerian orbit $r_{\rm ms}$ (Bardeen et al., 1972). Indicating with $l_{\rm mb}$ the angular momentum at the marginally bound Keplerian orbit, the disk will have a finite radial extension only if $W_{\rm in} < 0$ for $|l_0| \geq |l_{\rm mb}|$, while for $|l_{\rm ms}| < |l_0| < |l_{\rm mb}|$ the disk will be disconnected from the black hole only if $W_{\rm in} < W_{\rm cusp}$, where $W_{\rm cusp}$ is the value of the potential at the cusp (Abramowicz et al., 1978). Fig. 3.2 shows some examples of possible disk configurations for different values of its specific angular momentum. Once the potential W is known in all space, we can calculate the enthalpy density from Eq. (3.97), and the pressures p and p_m from the corresponding equations of state Eq. (3.95) and Eq. (3.96), while the four-velocity components will be given by

$$u^t = -\frac{1}{u_t(1-\Omega_0 l_0)}, \qquad u^\phi = \Omega_0 u^t, \tag{3.107}$$

where $\Omega_0 = \Omega(l_0)$ is computed from Eq. (3.80). The components of the magnetic field four-vector are

$$b^\phi = \pm\sqrt{\frac{2p_m}{\mathcal{A}}}, \qquad b^t = l_0 b^\phi. \tag{3.108}$$

Finally, although not necessary, we adopt in our study for simplicity the same value for the barotropic exponents $\varkappa$ and ζ. Both quantities are set equal to the specific heat ratio for a relativistic fluid $\Upsilon = 4/3$, i.e. we can rewrite Eq. (3.97) as

$$W - W_{\rm in} + 4\frac{p+p_m}{w} = 0. \tag{3.109}$$

4. Numerical methods

In this chapter we describe the numerical methods and algorithms used to construct and evolve our disk models. Our study main tool is the `ECHO` code (*Eulerian Conservative High Order scheme*) (Del Zanna and Bucciantini, 2002; Del Zanna et al., 2003, 2007), specifically developed to treat magnetohydrodynamics problems in a general relativistic framework.
We first introduce the original scheme used to solve the ideal GRMHD equations as presented in the original papers. Then we analyze the modifications necessary to include non-ideal effects such as turbulent resistivity and mean-field dynamo action (introduced in Chapter 2) and the corresponding numerical schemes required to solve the hyperbolic system. Finally, we present the main improvements on the parallelization scheme that allowed us to perform the highly expensive 3-dimensional computations that our studies required.

4.1. The code's original version

The goal of the code is to time-integrate the set of GRMHD equations described in Chapter 3, following the evolution of the fluid and electromagnetic quantities that determine the state of an astrophysical plasma.
Let us first consider the first five equations from set (3.29), postponing a discussion of the remaining ones to the sections concerned with the treatment of electric and magnetic fields. Assuming a stationary metric and expanding the covariant derivation operators, it is possible to rewrite them as (Del Zanna et al., 2007)

$$\frac{\partial \boldsymbol{u}}{\partial t} + \sum_{i=1}^{d} \frac{\partial \boldsymbol{f}^i(\boldsymbol{u})}{\partial x^i} = \boldsymbol{s}, \tag{4.1}$$

where d is the dimensionality of the problem and the vectors $\boldsymbol{u}$, $\boldsymbol{f}^i$, and $\boldsymbol{s}$ are given by

$$\boldsymbol{u} = \gamma^{1/2} \begin{bmatrix} D \\ S_j \\ U \\ E^j \\ B^j \end{bmatrix}, \tag{4.2}$$

$$\boldsymbol{f}^i = \gamma^{1/2} \begin{bmatrix} \alpha v^i D - \beta^i D \\ \alpha W^i_j - \beta^i S_j \\ \alpha S^i - \beta^i U \\ [jik](-\gamma^{-1/2}\alpha B_k + [klm]\beta^l E^m) \\ [jik](\gamma^{-1/2}\alpha E_k + [klm]\beta^l B^m) \end{bmatrix}, \tag{4.3}$$

$$\boldsymbol{s} = \gamma^{1/2} \begin{bmatrix} 0 \\ \frac{1}{2}\alpha W^{ik}\partial_j \gamma_{ik} + S_i \partial_j \beta^i - U\partial_j \alpha \\ \frac{1}{2} W^{ik}\beta^j \partial_j \gamma_{ik} + W_i{}^j \partial_j \beta^i - S^j \partial_j \alpha \\ q\beta^j - \alpha J^j \\ 0 \end{bmatrix}, \tag{4.4}$$

Eq. (4.1) is a set of hyperbolic partial differential equations (PDEs) where the elements of the vector $\boldsymbol{u}$ are referred to as the *conservative* variables, since their time evolution is controlled by a conservation law with fluxes $\boldsymbol{f}^i$ and source terms $\boldsymbol{s}$. The importance of the 3+1 decomposition of the covariant GRMHD equations (3.26) introduced in Chapter 3 is now evident, because the covariant formalism is not compatible with the traditional numerical schemes used to solve the classical MHD equations.

4.1.1. Discretization and time integration

Let us consider, for the sake of simplicity, the unidimensional case of (4.1) with $d = 1$ and divide the domain defined by the interval $[a, b]$ in N cells $I_i = [x_{i-1/2}, x_{i+1/2}]$. Let us assume that the intervalls have equal length $\Delta x = (b-a)/N$ and are each centered at the grid point

$$x_i = a + (i - 1/2)\Delta x \quad \text{with} \quad i = 1, \ldots, N. \tag{4.5}$$

Calling r the spatial accuracy order, the point value of a generic quantity $g(x)$ at a given time t is $g_i = g(x_i) + O((\Delta x)^r)$ and its interface values are $g_{i\pm1/2} = g(x_{i\pm1/2}) + O((\Delta x)^r)$.
We are now looking for a spatial discretization of (4.1) on this grid. For the moment we neglect the source terms, since they will not need to be discretized but they are computed at the cell centers x_i.

The discretization scheme implemented in ECHO is a so-called *finite difference* one. To calculate spatial derivatives of a flux we expand it into a Taylor series

$$\frac{\partial f}{\partial t}(x_i) = \frac{f_{i+1/2} - f_{i-1/2}}{\Delta x} + O((\Delta x)^2), \tag{4.6}$$

and express Eq. (4.1) as

$$\frac{\partial \boldsymbol{u}_i}{\partial t} = -\frac{\hat{\boldsymbol{f}}_{i+1/2} - \hat{\boldsymbol{f}}_{i-1/2}}{\Delta x}, \tag{4.7}$$

where $\hat{\boldsymbol{f}}_{i\pm1/2}$ represents an approximation of the primitive of physical flux function $\boldsymbol{f}(x)$ at the right (left) interface of the i-th cell. This means that the cell averages of $\hat{\boldsymbol{f}}$ must concide with the point value $\boldsymbol{f}_i$ of the flux $\boldsymbol{f}(x)$, to the given accuracy. This simple discretization provides a scheme of 2nd order accuracy. To achieve higher orders it is necessary to consider further terms in the expansion in Eq. (4.6). Once the quantities $\hat{\boldsymbol{f}}_{i\pm1/2}$ are known, it is possible to perform the time integration as described in Eq. (4.7), but it is clear from Eq. (4.3) that to compute the fluxes it is necessary to calculate the so-called *primitive* variables

$$\boldsymbol{p} = \{\rho, v^j, p, E^j, B^j\}, \tag{4.8}$$

where ρ, $\boldsymbol{v}$ and p are respectively the rest mass density, the velocity, and the pressure of the fluid, while $\boldsymbol{E}$ and $\boldsymbol{B}$ are the usual electric and magnetic fields. Since the code evolves the conservative variables $\boldsymbol{u}$, one has first to invert the relation between $\boldsymbol{u}$ and $\boldsymbol{p}$ by using Eq. (3.36).

The interface value of the primitive variables can be retrieved by means of polynomial interpolation during the *reconstruction* phase of the algorithm. As a consequence there will be in general two different states at both sides of each cell interface (as the fluid equations allow for discontinuous solutions) and at the lowest order we can identify them with $\boldsymbol{p}^L_{i+1/2} = \boldsymbol{p}_i$ and $\boldsymbol{p}^R_{i+1/2} = \boldsymbol{p}_{i+1}$. To achieve a higher accuracy it is necessary to compute the *left* and *right* states using *stencils* of grid points centered respectively at x_i and x_{i+1}. In this way the interface values are computed with high order accuracy in the sufficiently smooth regions of the computational domain, while in the presence of strong gradients the algorithm has to limit the interpolation to 1st order to ensure stability and avoid spurious oscillations. The ECHO code (in the original implementation of Del Zanna et al. (2007)) allows for a large number of different reconstruction schemes to be used, such as 2nd order TVD (*Total Variation Diminishing*, Harten (1983)), 3rd order CENO (*Convex Essentially Non-Oscillatory*, Liu and Osher (1998)), 3rd order PPM (*Piece-wise Parabolic Method*, Colella and Woodward (1984)) and 5th order MPE (*Minimal Polynomial Extrapolation*, Suresh and Huynh (1997)).

The discontinuities at the cell interfaces define a set of *local Riemann problems*. To better describe the structure of this problem, let us consider (4.1) rewritten as

$$\frac{\partial \boldsymbol{u}}{\partial t} + \frac{\partial \boldsymbol{f}}{\partial \boldsymbol{u}}\frac{\partial \boldsymbol{u}}{\partial x} = 0, \tag{4.9}$$

which is a hyperbolic system of n PDEs (where n coincides with the number of conservative variables) whose solution requires the computation of n real and distinct eigenvalues of the Jacobian $\partial \boldsymbol{f}/\partial \boldsymbol{u}$ (which in general depends on both the primitive and conservative variables). The eigenvalues are referred to as the *characteristic velocities of the system*, as they represent the speeds at which the information is transported by the fluid fluxes through the *characteristic waves* of the system, i.e. the eigenvectors.
Although there are algorithms that provide a numerically exact solution to this problem, their computational cost makes them unsuitable for the GRMHD context. A far more appropriate and affordable choice is the approximate Riemann solver HLL (Harten and van Leer, 1983) implemented in `ECHO`, since it only calculates the fastest and slowest characteristic velocity (respectively a^+ and a^-). It is still necessary though to ensure that the information propagates in the correct direction, a property that makes a scheme to be called *upwind*. The application of the HLL solver finally provides with the value of the flux at the cell interface (Londrillo and del Zanna, 2004)

$$\boldsymbol{f}^{HLL} = \frac{a^+ \boldsymbol{f}^L + a^- \boldsymbol{f}^R - a^+ a^- \left(\boldsymbol{u}^R - \boldsymbol{u}^L\right)}{a^+ + a^-}. \tag{4.10}$$

Finally we are ready to perform the time-integration of the conservative quantities, for instance with a 3$^{\text{rd}}$ order explicit Runge-Kutta scheme

$$\boldsymbol{u}^{(1)} = \boldsymbol{u}^n + \Delta t \mathfrak{L}[\boldsymbol{u}^n], \tag{4.11}$$
$$\boldsymbol{u}^{(2)} = \tfrac{3}{4}\boldsymbol{u}^n + \tfrac{1}{4}\boldsymbol{u}^{(1)} + \tfrac{1}{4}\Delta t \mathfrak{L}[\boldsymbol{u}^{(1)}], \tag{4.12}$$
$$\boldsymbol{u}^{n+1} = \tfrac{1}{3}\boldsymbol{u}^n + \tfrac{2}{3}\boldsymbol{u}^{(2)} + \tfrac{2}{3}\Delta t \mathfrak{L}[\boldsymbol{u}^{(2)}], \tag{4.13}$$

where the n index denotes the time step iteration, $\boldsymbol{u}^{(1)}$ and $\boldsymbol{u}^{(2)}$ are intermediate states, and $\mathfrak{L}[\boldsymbol{u}]$ is the member on the right-hand side of Eq. (4.7) plus the proper source term $\boldsymbol{s}$.

4.1.2. Magnetic field treatment

Contrary to the other variables evolved in time, the magnetic field $\boldsymbol{B}$ has also to fulfill at all times the constraint given by Eq. (3.29f), which formally could be regarded as an initial condition: the structure of the induction equation guarantees the analytical null divergence of $\boldsymbol{B}$. From a numerical perspective this is in general not true, since for upwind schemes the derivations in different directions are no longer commutable, so that spurious magnetic monopoles can appear during the computation. To properly deal with this problem the *Upwind Constrained Transport* scheme (UCT, presented by Londrillo and del Zanna (2004)) was implemented in `ECHO`.

For this method it is convenient to introduce the quantities

$$\mathcal{B}^i = \gamma^{1/2} B^i, \tag{4.14}$$
$$\mathcal{E}_i = \alpha E_i + \epsilon_{ijk}\beta^j B^k, \tag{4.15}$$

to rewrite (3.29d) and (3.29f) as

$$\partial_t \mathcal{B}^i + [ijk]\partial_j \mathcal{E}_k = 0, \tag{4.16}$$
$$\partial_i \mathcal{B}^i = 0. \tag{4.17}$$

We now integrate over the cell $I_{i,j,k}$ with center at the point $P_{i,j,k} \equiv (x_i, y_j, z_k)$, apply Stoke's theorem and assume for simplicity a 2^{nd} order accuracy, obtaining for the x-component of $\boldsymbol{\mathcal{B}}$

$$\frac{\mathrm{d}\mathcal{B}_x}{\mathrm{d}t} = -\frac{\Delta_y \mathcal{E}_z}{\Delta y} + \frac{\Delta_z \mathcal{E}_y}{\Delta z}, \tag{4.18}$$

where $\mathcal{B}_x$ is evaluated at the middle of the interface between cell $I_{i,j,k}$ and $I_{i+1,j,k}$ (i.e. at $P_{i+1/2,j,k}$), while $\mathcal{E}_z$ and $\mathcal{E}_y$ are evaluated respectively at $P_{i+1/2,j+1/2,k}$ and $P_{i+1/2,j,k+1/2}$. The operator Δ_x centered at $P_{i,j,k}$ is defined by

$$[\Delta_x f]_{i,j,k} = f_{i+1/2,j,k} - f_{i-1/2,j,k}. \tag{4.19}$$

Extending this calculation to the remaining two components of $\boldsymbol{\mathcal{B}}$ and considering the time derivative of the spatially discretized solenoidal constraint, we obtain

$$\frac{\mathrm{d}}{\mathrm{d}t}\left(\frac{\Delta_x \mathcal{B}_x}{\Delta x} + \frac{\Delta_y \mathcal{B}_y}{\Delta y} + \frac{\Delta_z \mathcal{B}_z}{\Delta z}\right) = 0, \tag{4.20}$$

which guarantees Eq. (4.17) to be algebraically satisfied for all times, assuming $\boldsymbol{\mathcal{B}}(t = 0)$ to be divergence free. For this reason the quantities evolved in time with the CT method (*Constrained Transport*) are the *staggered* components

$$[\mathcal{B}_x]_{i+1/2,j,k}, [\mathcal{B}_y]_{i,j+1/2,k}, [\mathcal{B}_z]_{i,j,k+1/2}, \tag{4.21}$$

which represent the point values of the components of $\boldsymbol{\mathcal{B}}$ evaluated respectively at $P_{i+1/2,j,k}$, $P_{i,j+1/2,k}$ and $P_{i,j,k+1/2}$, i.e. the centers of the interfaces orthogonal to the corresponding magnetic field component.
It can be shown (Londrillo and del Zanna, 2004) that the staggered components have the important property of being continuous along the normal to the interface on which they are defined. Hence, the *left* and *right* states coincide and need not to be reconstructed as the other variables for the fluxes calculation. The obvious drawback is that when the values of the magnetic field components are required at the cell center $P_{i,j,k}$ (for instance, when the data are written into an output file) they can be retrieved only by an interpolation step.

4.2. Electric field treatment

We now describe one of the main modifications applied to the original version of ECHO, which allows one to include a finite value of resistivity in the description of the astrophysical plasma.
In the original version of the code an explicit 3rd order Runge-Kutta algorithm, as described by Eq. (4.11)), (4.12) and (4.13), is used to perform the time integration of the spatially discretized GRMHD equations, which are therefore translated from the original system of hyperbolic PDEs to one of ODEs. Despite being a method commonly used in the solution of problems involving perfectly conducting plasmas, it is not suitable to deal with the introduction of magnetic resistivity in the GRMHD equations. In fact, if we consider Eq. (3.58), the evolution time scales in regions of high and low conductivity can significantly differ. The terms which are proportional to the inverse of η, in general, can be orders of magnitude larger than the flux term $\alpha\boldsymbol{B} - \boldsymbol{\beta} \times \boldsymbol{E}$ or the source term $(\alpha\boldsymbol{v} - \boldsymbol{\beta})q$ in those regions where the resistivity is sufficiently small, with negative consequences for the integration stability.
In order to provide stability and efficiency to the solution of the resistive GRMHD equations we introduce the *IMEX* Runge-Kutta schemes (Pareschi and Russo, 2005) (*IMplicit EXplicit*) in ECHO. These schemes were explicitly developed for the integration of *stiff* ODE, i.e. differential equations with terms that can evolve on very different time scales and hence lead to numerical instability.

4.2.1. Hyperbolic systems with stiff terms

A typical stiff differential equation may be written as

$$\partial_t \boldsymbol{U} = \boldsymbol{Q}(\boldsymbol{U}) + \boldsymbol{R}(\boldsymbol{U}), \tag{4.22}$$

where Q depends linearly on the first derivative of $\boldsymbol{U}$, while $\boldsymbol{R}$ does not include derivatives of $\boldsymbol{U}$ and is proportional to the reciprocal of the so-called relaxation time $\tau_{\rm rel}$. In the case of the resistive GRMHD equations, $\tau_{\rm rel}$ can be regarded as the resistivity η, $\boldsymbol{U}$ as the vector of conservative variables, $\boldsymbol{Q}$ as the sum of the divergence and the *non-stiff* source terms, while $\boldsymbol{R}$ represents the remaining *stiff* source terms proportional to the reciprocal of η.
For a perfectly non-conducting plasma (i.e. in the limit $\tau_{\rm rel} \to \infty$) the system is hyperbolic, and information propagation is limited by a characteristic speed c_h. Calling L the length-scale of the system, there will be a corresponding relaxation time defined by $\tau \equiv L/c_h$. On the contrary in the limit $\tau_{\rm rel} \to 0$ the system will be stiff, since the time scale of the term $\boldsymbol{R}$ is in general much smaller that the hyperbolic time scale τ_h. To provide numerical stability for an explicit integration scheme it will be necessary to set $\Delta t \leq \tau_{\rm rel}$, where Δt is the integration time step.

However, such a constraint can be far more restrictive than the usual Courant-Friederichs-Lewy (CFL) stability condition $\Delta t \leq \Delta x/c_h$ used in the non resistive case, since the minimum time step that allows for a stable integration will be reduced by up to a few orders of magnitude for sufficiently small values of η.

4.2.2. IMEX schemes

To integrate the stiff equations of resistive GRMHD without numerical instabilities with reasonable computing resources, we substitute the original explicit 3$^{\text{rd}}$ order Runge-Kutta algorithm with the IMEX scheme (Rezzolla and Zanotti, 2013).
Let us separate the conservative variables $\boldsymbol{U}$ into subgroups $\{\boldsymbol{X}, \boldsymbol{Y}\}$, where $\boldsymbol{X}$ represents variables whose evolution is governed by a stiff differential equation (in our case the vector $\gamma^{1/2}\boldsymbol{E}$), and $\boldsymbol{Y}$ stands for all other variables. We rewrite Eq. (4.22) for these two variables in the form

$$\partial_t \boldsymbol{Y} = \boldsymbol{Q}_Y(\boldsymbol{X}, \boldsymbol{Y}), \tag{4.23}$$

$$\partial_t \boldsymbol{X} = \boldsymbol{Q}_X(\boldsymbol{X}, \boldsymbol{Y}) + \boldsymbol{R}_X(\boldsymbol{X}, \boldsymbol{Y}), \tag{4.24}$$

where the operators $\boldsymbol{Q}_Y$ and $\boldsymbol{Q}_X$ contain spatial derivatives of the fluxes and the non-stiff source terms respectively of $\boldsymbol{Y}$ and $\boldsymbol{X}$, while $\boldsymbol{R}_X$ contains the stiff source terms which regulate $\boldsymbol{X}$. In the most general case of a resistive plasma with mean-field dynamo action, a comparison with Eq. (3.58) provides the following form for the latter operator

$$\boldsymbol{R}_X \equiv -\gamma^{1/2}\alpha\Gamma\{\boldsymbol{E} + \boldsymbol{v}\times\boldsymbol{B} - (\boldsymbol{E}\cdot\boldsymbol{v})\boldsymbol{v} - \xi[\boldsymbol{B} - \boldsymbol{v}\times\boldsymbol{E} - (\boldsymbol{B}\cdot\boldsymbol{v})\boldsymbol{v}]\}/\eta. \tag{4.25}$$

Each intermediate step of the IMEX Runge-Kutta method can now be divided in two parts:

1. First we explicitly calculate the intermediate values $\{\boldsymbol{X}_*^{(i)}, \boldsymbol{Y}_*^{(i)}\}$ for each intermediate step i according to

$$\boldsymbol{Y}_*^{(i)} = \boldsymbol{Y}^n + \Delta t \sum_{j=1}^{i-1} \tilde{a}_{ij} \boldsymbol{Q}_Y[\boldsymbol{U}^{(j)}], \tag{4.26}$$

$$\boldsymbol{X}_*^{(i)} = \boldsymbol{X}^n + \Delta t \sum_{j=1}^{i-1} \tilde{a}_{ij} \boldsymbol{Q}_X[\boldsymbol{U}^{(j)}] + \Delta t \sum_{j=1}^{i-1} a_{ij} \boldsymbol{R}_X[\boldsymbol{U}^{(j)}]. \tag{4.27}$$

   The summation up to the $(i-1)$-th term guarantees the absence of implicit terms, while $\tilde{\mathbb{A}} \equiv (\tilde{a}_{ij})$ and $\mathbb{A} \equiv (a_{ij})$ are $\nu \times \nu$ matrices whose dimensions and coefficients will depend on the specific accuracy of the scheme and the number of intermediate steps.

2. Then we perform the implicit integration. The non-stiff variables can be regarded as completely evolved (as far as the intermediate step is concerned) and having the same status as those on the left-hand side of Eq. (4.11) and Eq. (4.12)

$$\boldsymbol{Y}^{(i)} = \boldsymbol{Y}_*^{(i)}. \tag{4.28}$$

The stiff variables have to be integrated further

$$\boldsymbol{X}^{(i)} = \boldsymbol{X}_*^{(i)} + a_{ii}\Delta t \boldsymbol{R}_X(\boldsymbol{X}^{(i)}, \boldsymbol{Y}_*^{(i)}). \tag{4.29}$$

Since the vector $\boldsymbol{X}^{(i)}$ appears in the operator $\boldsymbol{R}_X$ it will be necessary at each intermediate step to invert this system to retrieve the value of the evolved stiff variable.

After computing in each intermediate step i the two vectors $\{\boldsymbol{X}^{(i)}, \boldsymbol{Y}^{(i)}\}$, the final value of the conservative variable $\boldsymbol{U}$ at the time $t + \Delta t$ is given by

$$\boldsymbol{U}^{n+1} = \boldsymbol{U}^n + \Delta t \sum_{i=1}^{\nu} \tilde{\omega}_i \boldsymbol{Q}(\boldsymbol{U}^{(i)}) + \Delta t \sum_{i=1}^{\nu} \omega_i \boldsymbol{R}(\boldsymbol{U}^{(i)}), \tag{4.30}$$

where ω_i and $\tilde{\omega}_i$ are constant coefficients that along with the matrices $\mathbb{A}$ and $\tilde{\mathbb{A}}$ completely define the specific numerical scheme.
There are a large number of possible IMEX schemes in the literature, which differ in the number of intermediate steps, and their spatial and temporal order of accuracy. In the case of `ECHO` we implemented three different IMEX schemes of SSP type (*Strong Stability Preserving*, see Spiteri and Ruuth (2003)), which are high-order schemes for the integration of semi-discretized hyperbolic differential equations that preserve strong stability and avoid spurious oscillations. Each scheme is identified by the standard notation SSP$k(s, \sigma, p)$, where k represents the order of the SSP scheme, s is the number of implicit steps, σ is the number of explicit steps and p is the order of the IMEX scheme (Pareschi and Russo, 2005). To display all the coefficients that define a particular scheme we use the following notation (which is a modified version of the standard notation by Butcher (2000))

$$\text{SSP}k(s,\sigma,p)\text{:}\ \begin{array}{c|c} \tilde{\mathbb{A}} & \mathbb{A} \\ \hline \tilde{\boldsymbol{\omega}} & \boldsymbol{\omega} \end{array}.$$

SSP2(2,2,2):

0	0	μ	0
1	0	1-2μ	μ
1/2	1/2	1/2	1/2

SSP3(3,3,2):

0	0	0	μ	0	0
1	0	0	1-2μ	μ	0
1/4	1/4	0	1/2-μ	0	μ
1/6	1/6	2/3	1/6	1/6	2/3

SSP3(4,3,3):

0	0	0	0	δ	0	0	0
0	0	0	0	$-\delta$	δ	0	0
0	1	0	0	0	1-δ	δ	0
0	1/4	1/4	0	ζ	λ	$1/2-\zeta-\lambda-\delta$	δ
0	1/6	1/6	2/3	0	1/6	1/6	2/3

$$\mu \equiv 1 - 1/\sqrt{2}$$
$$\delta \equiv 0.24169426078821$$
$$\zeta \equiv 0.06042356519705$$
$$\lambda \equiv 0.12915286960590$$

Figure 4.1.: Coefficient tables for the three IMEX schemes implemented in ECHO.

If we, for instance, choose the IMEX SSP2(2,2,2) scheme (see Fig. 4.1), the sequence of integration steps is

$$\begin{aligned}
\boldsymbol{Y}^{(1)} &= \boldsymbol{Y}^n, && (4.31)\\
\boldsymbol{X}^{(1)} &= \boldsymbol{X}^n + \Delta t \mu \boldsymbol{R}_X(\boldsymbol{Y}^{(1)}, \boldsymbol{X}^{(1)}), && (4.32)\\
\boldsymbol{Y}^{(2)} &= \boldsymbol{Y}^n + \Delta t \boldsymbol{Q}_Y(\boldsymbol{Y}^{(1)}, \boldsymbol{X}^{(1)}), && (4.33)\\
\boldsymbol{X}^{(2)} &= \boldsymbol{X}^n + \Delta t \boldsymbol{Q}_X(\boldsymbol{Y}^{(1)}, \boldsymbol{X}^{(1)}), && (4.34)\\
&\quad + \Delta t \left[(1-2\mu)\boldsymbol{R}_X(\boldsymbol{Y}^{(1)}, \boldsymbol{X}^{(1)}) + \mu \boldsymbol{R}_X(\boldsymbol{Y}^{(2)}, \boldsymbol{X}^{(2)})\right], && (4.35)\\
\boldsymbol{Y}^{n+1} &= \boldsymbol{Y}^n + \tfrac{\Delta t}{2}\left[\boldsymbol{Q}_Y(\boldsymbol{Y}^{(1)}, \boldsymbol{X}^{(1)}) + \boldsymbol{Q}_Y(\boldsymbol{Y}^{(2)}, \boldsymbol{X}^{(2)})\right], && (4.36)\\
\boldsymbol{X}^{n+1} &= \boldsymbol{X}^n + \tfrac{\Delta t}{2}\left[\boldsymbol{Q}_X(\boldsymbol{Y}^{(1)}, \boldsymbol{X}^{(1)}) + \boldsymbol{Q}_X(\boldsymbol{Y}^{(2)}, \boldsymbol{X}^{(2)})\right], && (4.37)\\
&\quad + \tfrac{\Delta t}{2}\left[\boldsymbol{R}_X(\boldsymbol{Y}^{(1)}, \boldsymbol{X}^{(1)}) + \boldsymbol{R}_X(\boldsymbol{Y}^{(2)}, \boldsymbol{X}^{(2)})\right]. && (4.38)
\end{aligned}$$

If we finally consider the IMEX-SSP3(4,3,3) scheme, it is interesting to verify how its explicit integration phase coincides with the traditional explicit 3$^{\text{rd}}$ order Runge-Kutta scheme adopted in the original version of ECHO. The explicit

intermediate steps of this IMEX scheme are given by

$$\begin{aligned}
\boldsymbol{U}^{(1)} &= \boldsymbol{U}^n, && (4.39)\\
\boldsymbol{U}^{(2)} &= \boldsymbol{U}^n, && (4.40)\\
\boldsymbol{U}^{(3)} &= \boldsymbol{U}^n + \Delta t \boldsymbol{Q}_U(\boldsymbol{U}^{(1)}), && (4.41)\\
\boldsymbol{U}^{(4)} &= \boldsymbol{U}^n + \Delta t \left[\tfrac{1}{4}\boldsymbol{Q}_U(\boldsymbol{U}^{(2)}) + \tfrac{1}{4}\boldsymbol{Q}_U(\boldsymbol{U}^{(3)})\right], && (4.42)\\
\boldsymbol{U}^{(n+1)} &= \boldsymbol{U}^n + \Delta t \left[\tfrac{1}{6}\boldsymbol{Q}_U(\boldsymbol{U}^{(2)}) + \tfrac{1}{6}\boldsymbol{Q}_U(\boldsymbol{U}^{(3)}) + \tfrac{2}{3}\boldsymbol{Q}_U(\boldsymbol{U}^{(4)})\right], && (4.43)
\end{aligned}$$

and from Eq. Eq. (4.42) we get

$$\tfrac{1}{6}\Delta t \boldsymbol{Q}_U(\boldsymbol{U}^{(3)}) = \tfrac{2}{3}\boldsymbol{U}^{(4)} - \tfrac{2}{3}\boldsymbol{U}^n - \tfrac{1}{6}\Delta t \boldsymbol{Q}_U(\boldsymbol{U}^{(2)}). \tag{4.44}$$

If we replace Eq. (4.44) into Eq. (4.43) we obtain

$$\boldsymbol{U}^{(n+1)} = \tfrac{1}{3}\boldsymbol{U}^n + \tfrac{2}{3}\boldsymbol{U}^{(4)} + \tfrac{2}{3}\Delta t \boldsymbol{Q}_U(\boldsymbol{U}^{(4)}), \tag{4.45}$$

which exactly corresponds to Eq. Eq. (4.13) once we rename $\boldsymbol{U}^{(3)} \to \boldsymbol{U}^{(1)}$ and $\boldsymbol{U}^{(4)} \to \boldsymbol{U}^{(2)}$.

4.2.3. Implicit step

We now analyze in detail the implicit integration performed in the IMEX schemes to compute the evolution of the electric field $\boldsymbol{E}$.
First we perform a 1st order discretization of the time derivative in Eq. (3.58). We evaluate the non-stiff terms at the initial time t of the integration procedure (explicit discretization) using the index $^{(0)}$. The quantities in the stiff terms are calculated at the time $t + \Delta t$ (implicit discretization) and labeled with $^{(1)}$. Expanding in components we get

$$\begin{aligned}
E^{i(1)} = \; & Q^{i(0)} \\
& - \left[\Gamma^{(1)} E^{i(1)} + \epsilon^{ijk}\tilde{v}_j^{(1)} B_k^{(1)} - \left(E^{k(1)}\tilde{v}_k^{(1)}\right)\tilde{v}^{i(1)}/\Gamma^{(1)}\right]/\tilde{\eta} \\
& + \xi\left[\Gamma^{(1)} B^{i(1)} - \epsilon^{ijk}\tilde{v}_j^{(1)} E_k^{(1)} - \left(B^{k(1)}\tilde{v}_k^{(1)}\right)\tilde{v}^{i(1)}/\Gamma^{(1)}\right]/\tilde{\eta},
\end{aligned} \tag{4.46}$$

where we should actually write $\tilde{\eta} = \tilde{\eta}^{(1)}$ and $\tilde{\xi} = \tilde{\xi}^{(1)}$, since these coefficients may depend on quantities such as temperature, density, or magnetic field. The other quantities in Eq. (4.46) are

$$\begin{aligned}
\tilde{v}^i &= \Gamma v^i, && (4.47)\\
\tilde{v}_i &= \Gamma v_i, && (4.48)\\
\Gamma^2 &= 1 + \tilde{v}_i\tilde{v}^i, && (4.49)\\
Q^i &= E^i + \Delta t\left[-(\alpha v^i - \beta^i)q + \epsilon^{ijk}\partial_j\left(\alpha B_k - \epsilon_{klm}\beta^l E^m\right)\right], && (4.50)\\
q &= \gamma^{-1/2}\partial_k(\gamma^{1/2}E^k), && (4.51)\\
1/\tilde{\eta} &= \Delta t\alpha/\eta. && (4.52)
\end{aligned}$$

Solving Eq. (4.46) for E^i, we obtain after some lengthy algebraic calculation

$$\begin{aligned} E^i[\Gamma + \tilde{\eta} + \xi^2(\Gamma^2 - 1)/(\Gamma + \tilde{\eta})] = \\ & -\epsilon^{ijk}\tilde{v}_j B_k + \tilde{\eta}\left[Q^i + \left(Q^k\tilde{v}_k\right)\tilde{v}^i/(1+\tilde{\eta}\Gamma)\right] \\ & +\xi\left[\Gamma B^i - \tilde{\eta}\left(B^k\tilde{v}_k\right)\tilde{v}^i/(1+\tilde{\eta}\Gamma)\right] \\ & -\xi\left[(\Gamma^2-1)B^i - \left(B^k\tilde{v}_k\right)\tilde{v}^i + \tilde{\eta}\epsilon^{ijk}\tilde{v}_j Q_k\right]/(\Gamma+\tilde{\eta}) \\ & -\xi^2\left[\Gamma\epsilon^{ijk}\tilde{v}_j B_k\right]/(\Gamma+\tilde{\eta}) \\ & +\xi^2\left[\tilde{\eta}\Gamma\left(Q^k\tilde{v}_k\right) + \xi\left(B^k\tilde{v}_k\right)\right]\tilde{v}^i/[(1+\tilde{\eta}\Gamma)(\Gamma+\tilde{\eta})], \end{aligned} \tag{4.53}$$

where we renamed $Q^{i(0)} \to Q^i$ and dropped the $^{(0)}$ and $^{(1)}$ labels for simplicity. In the case of pure resistive GRMHD ($\xi = 0$) many terms can be neglected, and Eq. (4.53) reduces to

$$E^i(\Gamma + \tilde{\eta}) = -\epsilon^{ijk}\tilde{v}_j B_k + \tilde{\eta}\left[Q^i + \left(Q^k\tilde{v}_k\right)\tilde{v}^i/(1+\tilde{\eta}\Gamma)\right], \tag{4.54}$$

and if we consider a perfectly conducting plasma ($\eta = 0$) we are left with the usual relation $E^i = -\epsilon^{ijk}\tilde{v}_j B_k$.
With the aid of Eq. (4.53) we can finally perform the implicit integration Eq. (4.29). Since the primitive variables appear in the expression for the computation of the electric field but are available only at the end of the intermediate integration step, Eq. (4.53) will need to be solved at the same time as the inversion from conservative to primitive variables is performed:

$$\{D, S_i, U, E^i, B^i\} \Rightarrow \{\rho, v^i, p, E^i, B^i\}. \tag{4.55}$$

For this reason it will be necessary to adopt an iterative numerical procedure (Palenzuela et al., 2009; Bucciantini et al., 2012):

- First we choose as a guess for the velocity the value from the previous step, i.e. $\boldsymbol{v}_0 = \boldsymbol{v}^n$.
- Next we retrieve its current value by inversion of the relation defining the momentum density in Eq. (3.37), i.e. we need to find the zeros of the functions

  $$f_i(\boldsymbol{v}) = \rho h \Gamma^2 v_i + \epsilon_{ijk} E^j B^k - S_i, \tag{4.56}$$

  where the index i runs from 1 to 3. We select as equation of state a standard *polytropic law* for a perfect gas

  $$p(\rho, \epsilon) = (\Upsilon - 1)\rho\epsilon, \tag{4.57}$$

  where we set the adiabatic index $\Upsilon = 4/3$, as it is appropriate for a relativistic fluid. This allows us to express the specific enthalpy solely in terms of density and pressure

  $$h = 1 + \frac{\Upsilon}{\Upsilon - 1}\frac{p}{\rho}. \tag{4.58}$$

Considering now the definition of relativistic energy density from Eq. (3.38), after some algebra we can express Eq. (4.56) in terms of the velocity components and the conservatives variables only, that is

$$f_i(\boldsymbol{x}) = \frac{\Gamma[U - \frac{1}{2}(E^2 + B^2)] - \frac{\Upsilon - 1}{\Upsilon} D}{\Gamma^2 - \frac{\Upsilon - 1}{\Upsilon}} x_i + \epsilon_{ijk} E^j B^k - S_i, \tag{4.59}$$

where we introduced the variables $x_i = (1 - v^2)^{1/2} v_i$, since their value can range from $-\infty$ to $+\infty$ providing a numerically more stable procedure.

- To find the roots of Eq. (4.59) we use a multidimensional Newton-Raphson scheme. After computing the Jacobian matrix $J_{ik} = \partial f_i / \partial x_i$ we perform a LU decomposition to invert it, and we calculate a new guess by

$$x_i' = x_{0i} + J_{ik}^{-1} f_k(\boldsymbol{x}_0). \tag{4.60}$$

- For each new guess of x_i we compute the electric field according to Eq. (4.53). The iteration is stopped when a tolerance of $|\delta \boldsymbol{x}| < 10^{-10}$ is reached.

- From the converged value of the velocity $\boldsymbol{v}$, we compute the final values for density and pressure

$$\rho = \frac{D}{\Gamma}, \tag{4.61}$$

$$p = \frac{U - \frac{1}{2}(E^2 + B^2) - \Gamma^2 \rho}{\frac{\Gamma^2 \Upsilon}{\Upsilon - 1} - 1}. \tag{4.62}$$

The inversion from conservative to primitive variables is usually the most delicate and computationally expensive part of a standard GRMHD code. During this procedure it is possible for the numerical algorithm to fail in providing physically acceptable values for the gas pressure, i.e. non-negative ones. As we can see from Eq. (4.62), this may happen whenever the magnetization value in the grid cell is so high that the magnetic energy density $U_{\rm em} = \frac{1}{2}(E^2 + B^2)$ almost matches the total energy density U. In these cases there could be a numerical overshooting in the evaluation of the quantity $U - U_{\rm em}$ that could lead to a negative pressure. To avoid this, `ECHO` evolves along with the standard GRMHD equations also the conservation law for the entropy density:

$$\nabla_\mu (\rho s u^\mu) = 0 \tag{4.63}$$

where $s = p/\rho^\Upsilon$. The adiabatic condition Eq. (4.63) is equivalent to the total energy conservation in absence of shocks or other sources of dissipation, and hence it is used whenever the use of the energy equation fails. We found that this procedure solved the vast majority of numerical issues related to this part of the algorithm. In the very few cases when this solution does not work either, we simply reset the primitives to their values at the previous time step.

4.3. Parallelization scheme

The latest development of the numerical algorithms in ECHO concerns a significant upgrade of its parallelization scheme, whose design and implementation has been worked out in collaboration with Dr. Fabio Baruffa and Dr. Markus Rampp at the *Max Planck Computing and Data Facility* (MPCDF) and the *AstroLab* group at the *Leibniz Rechenzentrum* (LRZ), Garching.
The main motivation behind this improvement were the computational costs of three-dimensional simulations, which are required to investigate non-axisymmetric modes in magnetized thick tori around black holes. The original version of ECHO included only the possibility to parallelize along one axis of the numerical domain (along x for Cartesian grids, along r for cylindrical and spherical ones), since most of the simulations performed with the code were restricted to two-dimensional domains. This choice allows for a maximum number of MPI tasks which is limited by the grid resolution along the direction to be parallelized, and proved to be unsuitable for our study because of the following reason.
The minimum resolution required by properly resolved magnetized models is $\sim 256^3$ grid points. A one-dimensional MPI decomposition, as in the original version of ECHO, would allow for a maximum number of MPI tasks given by

$$N_{\max}^{\mathrm{MPI}} = \frac{N_x}{n_{\mathrm{g}}}, \tag{4.64}$$

where N_x is the number of grid points along x (including ghost zones), and n_{g} is the number of ghost cells required by the interpolation and reconstruction routines. In practice, Eq. (4.64) gives an overestimate, since a significant amount of time is spent by the code communicating the boundaries between MPI tasks, making the effective maximum number of MPI tasks quite small. In the case of a 256^3 grid, $N_{\max}^{\mathrm{MPI}} \sim 20$, which proves to be inadequate to perform a series of sufficiently long 3D GRMHD simulations, especially when a resistive plasma is considered.

4.3.1. Multidimensional MPI domain-decomposition

The main improvement introduced in ECHO's parallelization scheme is the implementation of a multidimensional MPI domain-decomposition. This allows us to increase the maximum number of MPI tasks that can efficiently be used for a given grid resolution and to reduce the time spent during the communication between neightbouring cells. Finally, this provided a mean to greatly reduce the total runtime of a production run, i.e. it made it possible to perform a significant number of tests and actual simulations.
The starting point of the parallelization scheme is the definition of the topology

of the Cartesian grid of MPI tasks, whose dimensionality can range from 1 to 3. Via standard MPI Fortran routines each processor is given a specific rank and coordinates in such a grid along with a portion of the numerical domain (or *sub-domain*) to work on.
As long as the code does local calculations (e.g. Runge-Kutta integration, inversion from conservative to primitive variables, etc.) each processor does not need to interact with the others. When the primitives need to be reconstructed at the cell interfaces or the staggered magnetic field components need to be interpolated, the calculations require appropriate boundary informations from the ghost cells. The ghost zones that lay at the borders of the numerical domain represent the real *physical boundaries*, and they are filled with different values depending on the particular physical condition required.
For example, let us consider a generic quantity $Q = Q(x_i) \equiv Q_i$ and the problem of selecting the correct values at the inner boundary along the x axis ($i = 1$). The ghost zones will correspond then to the grid points x_{1-i} (where $i = 1, \ldots, n_g$), and we may apply one of the following different prescriptions:

- Positive reflecting boundary:

$$Q_{1-i} = Q_i. \tag{4.65}$$

  Example: the velocity component parallel to a reflective wall.

- Negative reflecting boundary:

$$Q_{1-i} = -Q_i. \tag{4.66}$$

  Example: the velocity component perpendicular to a reflective wall.

- Fixed boundary:

$$Q_{1-i} = \tilde{Q}. \tag{4.67}$$

  Example: the pressure at the surface of a star (which would have $\tilde{Q} = 0$).

- Open boundary (with different accuracy):

$$Q_{1-i} = \begin{cases} Q_1 & \text{(constant extrapolation)} \\ 2Q_{1-i} - Q_{2-i} & \text{(linear extrapolation)} \\ 3(Q_{1-i} - Q_{2-i}) + Q_{3-i} & \text{(quadratic extrapolation)} \end{cases} \tag{4.68}$$

  Example: every quantity that is allowed to flow outside the boundary.

If the ghost zones are within the numerical domain due to the domain decomposition (or in the special case of periodic boundaries), then each MPI task will have to communicate with all its neighbors to send the values needed by the others MPI tasks for their ghost zones, and in return receive the values to fill its

own boundaries. This *communication phase* is performed along all axis of the numerical domain for each MPI task anytime the boundary values are required. This can take a non-negligible amount of computing time (with respect of the total run-time of the application). Although a multidimensional decomposition allows for a larger maximum number of MPI tasks, it is still recommended to check how computationally expensive (in term of CPU time) the communication phase is. A reasonable metric to evaluate a priori whether or not a particular MPI decomposition is of advantage can be obtained by computing the ratio between the volume of data that need to be communicated and the volume of data that form the local sub-domain. Let us consider a grid resolution N^3, n_g ghost cells per boundary, and an MPI domain decomposition into $\mathcal{N}$ total tasks. Let us call n_x, n_y and n_z, respectively, the number of MPI tasks along the x, y, and z direction, which may differ one from each other, and is equal to 1 in case that direction is not split by the decomposition. The total data-volume that each MPI task will need to communicate for a given dimensionality d is

$$V_\mathrm{ghost} = 2n_\mathrm{g}N^2 \times \begin{cases} 1 & \text{for } d=1 \\ \left(\frac{1}{n_y}+\frac{1}{n_z}\right) & \text{for } d=2 \\ \left(\frac{1}{n_x n_y}+\frac{1}{n_x n_z}+\frac{1}{n_y n_z}\right) & \text{for } d=3 \end{cases} \tag{4.69}$$

where we assumed a 1-dimensional decomposition done along the z axis and the 2-dimensional one along the y and z axis [1]. If we now divide V_ghost by the data-volume of the local domain $V_\mathrm{dom} = N^3/\mathcal{N}$ we obtain

$$\chi \equiv \frac{V_\mathrm{ghost}}{V_\mathrm{dom}} = \frac{2n_\mathrm{g}}{N} \times \begin{cases} n_z & \text{for } d=1 \\ (n_y+n_z) & \text{for } d=2 \\ (n_x+n_y+n_z) & \text{for } d=3 \end{cases} \equiv \frac{2n_\mathrm{g}}{N}\sum_{i=1}^{d} n_i \tag{4.70}$$

The volume of all communicated ghost zones for a given local domain can equal at most the volume of the domain times twice the dimensionality of the decomposition. If the domain size is shrunk even further, there would not be enough grid points to communicate to the nearest neighbors. Therefore, we define the quantity

$$\tilde{\chi} = \frac{n_g}{Nd}\sum_{i=1}^{d} n_i, \tag{4.71}$$

which is normalized to 1 for any decomposition dimensionality. For the parallelization setup to be effective, the value of $\tilde{\chi}$ has to be sufficiently small, otherwise the code will start being *communication dominated* instead of *computation dominated*, i.e. a large fraction of the run-time will be used to exchange the boundary conditions between MPI tasks instead of performing actual computations.

[1] This choice is suggested by the way the Fortran language stores arrays in the computer memory.

4.3.2. Parallel I/O

Another bottleneck that has to be considered when performing 3D MHD simulations is the handling of data output. For a typical non-ideal GRMHD run on a 256^3 grid a single output file has to contain 11 variables defined on the whole domain $(\rho, \boldsymbol{v}, p, \boldsymbol{E}, \boldsymbol{B})$, which for a single precision floating-point accuracy means a file-size of $\sim$ 740 MB. An attempt to write the whole file in a serial fashion using a single *master* MPI task that collects all the data and outputs them into a file will lead to two major practical problems:

- The local memory accessible by the processor may not be large enough to store all the data, since at the same time the code has a large number of quantities that need to be kept in memory for the next computation steps.
- Writing on file such an amount of data with a single processor may considerably affect the performance of the code, requiring first a communication phase between all the MPI tasks to collect the data and then the actual writing phase.

For these reasons we decided to fully take advantage of the parallelization scheme used during the code's computation and let each MPI task individually write out its data on the same file. To achieve this goal we adopted the `HDF5`[2] standard to write our output files (instead of the original plain unformatted binary files) and made use of the `HDF5-MPI` library. The `HDF5` standard is a tool that allows storing data in *structured* binary files, i.e. files that are compact as binary files but whose content is organized in groups and datasets that can be easily accessed by simple terminal commands. Such an approach allows each MPI task to write its own data on a particular slab of the output file in parallel, significantly decreasing the amount of time that the code spends dealing with the output phase of the simulation.

4.3.3. Scaling

To quantify the performance of the parallelization scheme, we ran a scaling test with increasing number of MPI tasks, also increasing the grid resolution.
There are two important characteristics of a well-behaved parallel code that we are interested in:

- *Strong scaling*: ideally the value of run-time per iteration should be inversely proportional to the number of cores used. Deviations from this trend can be due to a non-optimal implementation of the communication routines.

[2] `https://www.hdfgroup.org`

We note that there is always a saturation point beyond which the code becomes communication-dominated, which we mentioned when introducing the $\tilde{\chi}$ parameter.

- *Weak scaling*: ideally the value of run-time per iteration should stay constant for the same ratio of number of grid zones N^3 over number of cores $\mathcal{N}$. This statement represents the expectation that when the volume of workload is increased by a certain factor, increasing accordingly the number of MPI tasks working on it should compensate for it. Deviations from this behavior are usually a good indicator for margins of improvement in the scheme.

We run two different tests, the first on the Hydra[3] cluster hosted by the *Max Planck Computing and Data Facility* (MPDCF), and the second one on SuperMuc[4] at the *Leibniz Rechenzentrum* (LRZ). Both tests involved the solution of a standard MHD problem, i.e. the propagation of an Alfvèn wave through a 3-dimensional domain.
On Hydra we used two different resolutions (256^3 and 512^3 grid points) running on a number of cores that ranged from 20 (corresponding to a single node) up to 5120 (hence 256 nodes) using a 2D MPI domain decomposition. Concerning the numerical algorithms, we opted for a 3$^{\text{rd}}$ order Runge-Kutta scheme coupled to an MPE5 reconstruction (requiring three ghost cells) and an HLL Riemann solver. The results for the test on the Hydra cluster are shown in Fig. 4.2. For the lower resolution run the code proved to have a perfect strong scaling up to 160 cores, but started to be communication dominated for larger numbers of cores. The same sort of saturation is exhibited by the high-resolution run, although for a smaller relative number of cores. Overall we obtained a good weak scaling for a ratio of grid points to number of cores down to $N^3/\mathcal{N} = 256^3/160 \simeq 10^5$, then the high-resolution run started to be communication dominated.
On SuperMuc we performed the same physical test but with a few differences. To match the setup of the productions runs involving the evolution of magnetized disks, we used a 2$^{\text{nd}}$ order Runge-Kutta scheme coupled to a PPM reconstruction (still requiring 3 ghost cells). Furthermore, in addition to the two-dimensional domain decomposition (2DD) tested on Hydra we also checked the performance of the more recent three-dimensional one (3DD). The number of cores ranged from 128 (8 nodes) to 8196 (512 nodes, corresponding to one full island). As we can see from Fig. 4.3, the 3DD provides overall faster computation than the 2DD, allowing a nearly perfect weak scaling up to 4096 cores. The runs on the 256^3

[3]The main part of the cluster, which was used for our tests, consists in $\sim$ 3500 nodes with 20 Intel Ivy Bridge cores @ 2.8 GHz and 64 GB memory each. Visit `www.mpcdf.mpg.de/services/computing/hydra/` for more details.

[4]The tests were launched on the *Phase 1 Thin nodes* of the cluster. Each node mounts 16 Intel Sandy Bridge cores @ 2.7 GHz and 32 GB of memory. More info on `https://www.lrz.de/services/compute/supermuc/systemdescription/`.

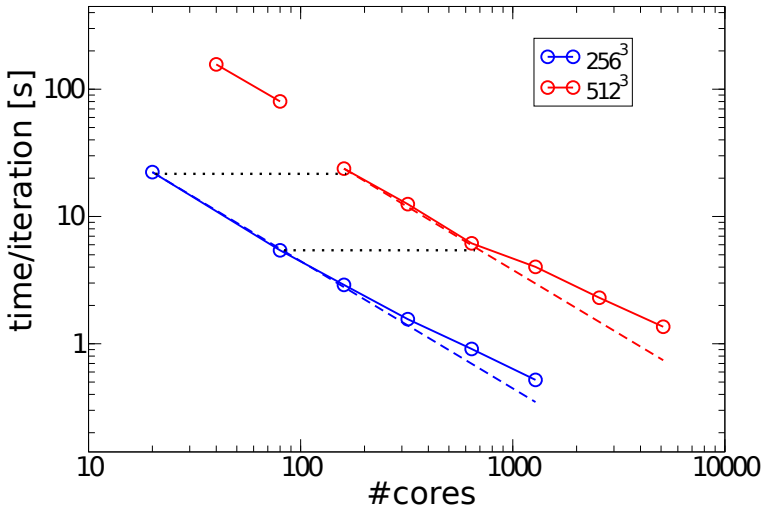

Figure 4.2.: Scaling plot on the Hydra cluster for the Alfvèn wave test with a 2D MPI domain decomposition. The blue curve refers to a 256^3 grid and the red curve to a 512^3 grid. The dashed lines represent the ideal *strong* scaling, while the dotted ones correspond to the ideal *weak* scaling.

grid show very little saturation up to 2048 cores, beyond which the $\tilde{\chi}$ parameter reaches values greater than ~ 0.25 for the 2DD and leads to a significant deviation from the strong scaling limit.

As further metric for the good behavior of the code, we computed for each run the quantity

$$\varepsilon = \frac{IN^3}{\mathcal{N}t}, \tag{4.72}$$

where I is the number of iterations and t is the runtime of the simulation. Ideally, the ratio between the number of *zone cycles* (IN^3) and the *CPU-time* ($\mathcal{N}t$) should be a constant of the code, independent of the particular problem or parallelization scheme. For this reason the parameter ε can be referred to as the *code efficiency*. As shown in Fig. 4.4, the value of ε for the 3DD varies much less than in the 2DD case. Apart from the lat run at 8196 cores, the 3DD provided a mean value of $\varepsilon \sim 3.7 \times 10^4$ with variations on at most $\delta\varepsilon \sim 5\%$.

It is important to notice that with a one-dimensional MPI domain decomposition the maximum number of cores at disposal would have been at most 85 and 170 respectively (for the two resolutions considered). In addition to this, the performance would be extremely poor for such a configuration, since each task would have to communicate the whole domain of the neighbour; this clearly shows how important the improvement of the parallelization scheme has been, and in general how a higher dimensionality in the domain decomposition leads to systematic better performances of the code.

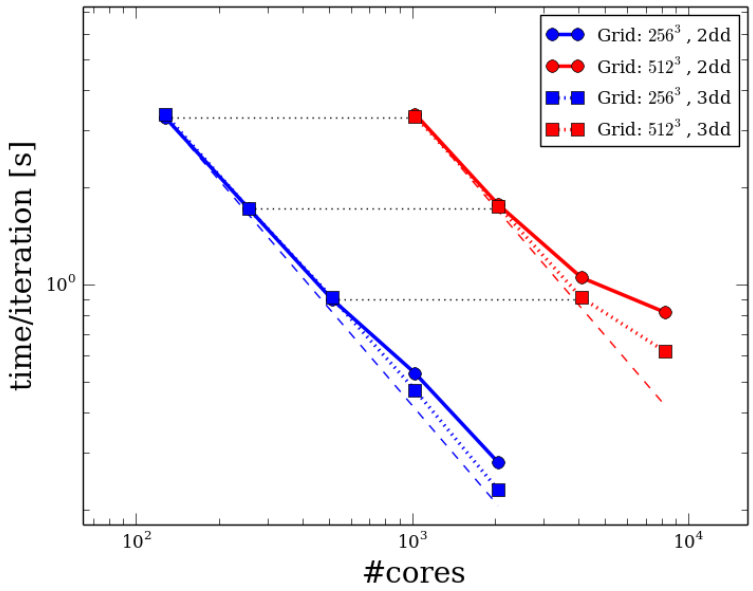

Figure 4.3.: Scaling plot on the SuperMuc cluster for the Alfvèn wave problem with both a 2D (circles) and 3D (squares) MPI domain decomposition. The blue curves refer to a 256^3 grid and the red curves to a 512^3 grid. The dashed lines represent the ideal *strong* scaling, while the dotted ones correspond to the ideal *weak* scaling.

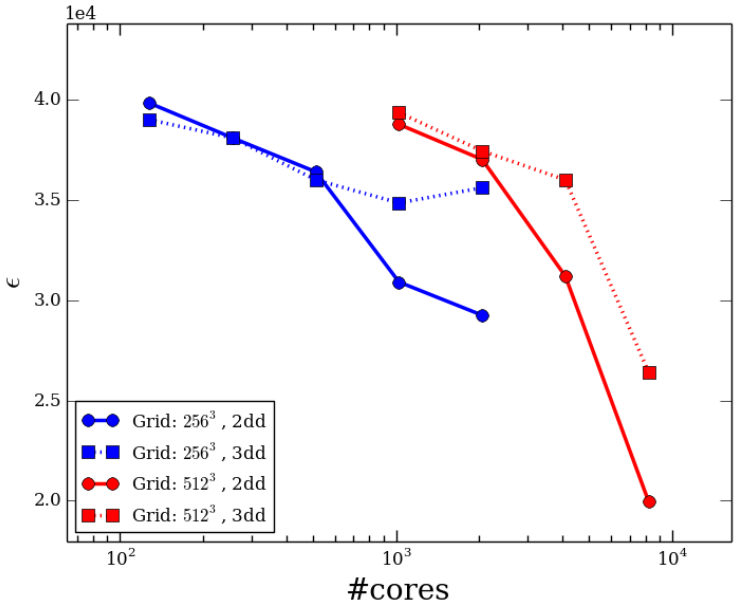

Figure 4.4.: Plot of the code's efficiency ϵ vs the number of cores for a 2D (circles) and 3D (squares) MPI domain decomposition. The blue curves refer to a 256^3 grid and the red curves to a 512^3 grid.

5. Numerical simulations

We finally present the results from two different sets of numerical simulations, which employed respectively the non-ideal covariant Ohm's closure described in Chapter 3 and the novel parallelization scheme mentioned in Chapter 4. The former study tackles the problem of magnetic field amplification in accretion disks and was conducted in the kinematic regime in axisymmetry. The goal of the latter is instead to analyze the fully dynamical non-axisymmetric behavior of thick magnetized accretion disks in absence of non-ideal effects, in order to assess the mutual interaction between PPI and MRI. Although addressing different problems, they both consider the same thick magnetized disk models that we constructed in Chapter 3, and therefore they can be considered as complementary to each other.

5.1. Kinematic $\alpha\Omega$-dynamo in thick disks

The first application of the covariant non-ideal Ohm's law closure (3.56) in the context of accretion disks is a study of the kinematic $\alpha\Omega$-dynamo in thick disks in axisymmetry. This work has been published during the course of my doctoral studies:
M. Bugli, L. Del Zanna, and N. Bucciantini. "Dynamo action in thick discs around Kerr black holes: high-order resistive GRMHD simulations". *MNRAS*, 440:L41–L45, may 2014.
The restriction to the kinematic regime means that we keep the fluid quantities ρ, $\boldsymbol{v}$, and p fixed in time, and we neglect the back-reaction of the evolution of the e.m. fields on them. Hence, we only integrate Maxwell equations and focus on the linear growth phase of the magnetic field. For this study we used the high-order $SSP3(4,3,3)$ IMEX scheme, coupled to the HLL Riemann solver and the MPE5 reconstruction algorithm. The simulations performed for this study had an extremely low computational cost (in fact, they were carried out on a personal laptop with dual-core processor).

Table 5.1.: Setups of the $\alpha\Omega$-dynamo models.

	Initial $\boldsymbol{B}$	η_{disk}	ξ_{disk}
Model 1	$\boldsymbol{B}_T$	10^{-3}	10^{-3}
Model 2	$\boldsymbol{B}_T$	10^{-3}	-10^{-3}
Model 3	$\boldsymbol{B}_T$	10^{-3}	5×10^{-3}
Model 4	$\boldsymbol{B}_T$	10^{-3}	2×10^{-4}
Model 5	$\boldsymbol{B}_T$	5×10^{-3}	5×10^{-3}
Model 6	$\boldsymbol{B}_T$	2×10^{-4}	2×10^{-4}
Model 7	$\boldsymbol{B}_P$	10^{-3}	10^{-3}
Model 8	$\boldsymbol{B}_P$	10^{-3}	5×10^{-3}
Model 9	$\boldsymbol{B}_P$	10^{-3}	2×10^{-4}
Model 10	$\boldsymbol{B}_P$	10^{-3}	-10^{-3}

5.1.1. Initial setup

The initial model is a magnetized thick torus, as described in Chapter 3, orbiting around a Kerr black hole of mass M and spin $a = 0.99$. The disk's inner edge and center are at $r_{\rm in} = 3\ M$ and $r_{\rm c} = 5\ M$, respectively. Since we are adopting the *Cowling approximation*, i.e. neglecting the self gravity of the disk, we are also disregarding any change in the central black hole mass due to accretion and hence we can freely rescale the density to an arbitrary value. To avoid numerical underflows we set the central density of the disk to $\rho_{\rm c} = 1$, while the atmosphere is initialized as an isentropic stationary gas of density $\rho_{\rm atm} = 10^{-5}$.
We use Boyer-Lindquist spherical coordinates and a two-dimensional computational domain that extends in the radial direction $r \in [r_{\rm h} + 1.5, 25]M$ and polar direction $\theta \in [\pi/4 - 0.2, 3\pi/4 + 0.2]$. A modest resolution of 120^2 grid points was enough to capture the dynamics of the system with sufficient accuracy. Further runs at higher resolution (200^2 grid points) delivered the same qualitative and quantitative results. The numerical grid is uniform along θ but refined along r, that is we used a finer grid close to the black hole and coarser one towards the outer radial edge of the domain. This was achieved by defining the radial coordinates r_i of the grid points as

$$r_i = r_{min} + \frac{(r_{max} - r_{min})}{\psi} \tan\left(m_i \arctan \psi\right), \tag{5.1}$$

where

$$m_i = \frac{x_i - r_{min}}{r_{max} - r_{min}}. \tag{5.2}$$

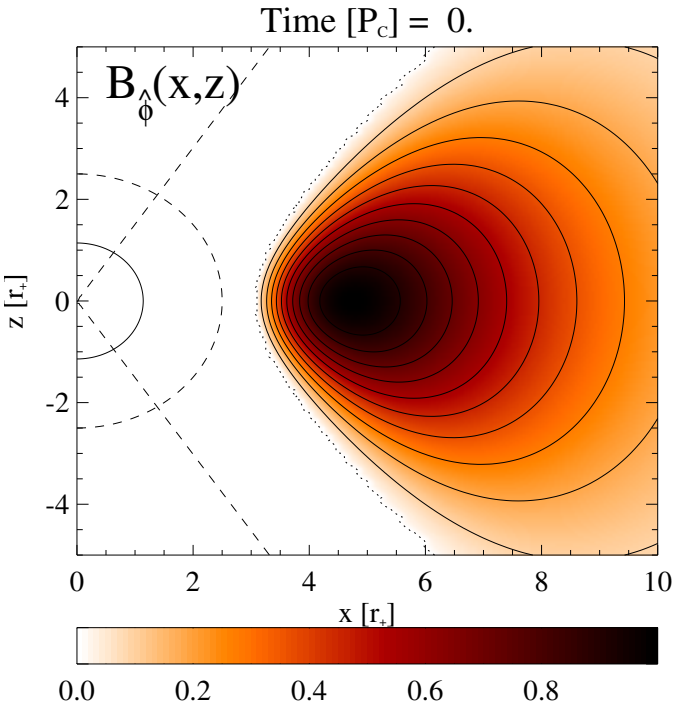

Figure 5.1.: Initial profile of $B_{\hat{\phi}}$ for the models initialized with a purely toroidal magnetic field, normalized by the maximum of $|\boldsymbol{B_T}| \equiv |B_{\hat{\phi}}|$. The solid semi-circle represents the black hole event horizon $r_+ = 1\ M$, while the dashed curves are the boundaries of the numerical domain. Finally, the dotted line represents the disk's edge, identified as the region beyond which the density decreases below a value $\rho_* = 10^{-4}\rho_c$.

In these expressions $r_{min} = r_+ + 1.5$, $r_{max} = 25$, x_i are the values of the cell centers for a uniform grid and ψ is a *stretching* factor whose value is set to 10.

We used two different magnetic configurations. Some disks were initialized according to the model by Komissarov (2006) with a purely toroidal field $\boldsymbol{B}_T$ with central magnetization $\sigma_c = 1$ (Fig. 5.1). This choice for σ_c was made to ensure a better numerical stability required by the high-order schemes we used, but it is clearly in contrast with the assumption of kinematic regime. In fact it leads to a magnetic pressure equal to the thermal one. However, since we only integrate Maxwell's equations, σ_c only sets the initial value of the magnetic field and our results, appropriately normalized, provide an accurate estimate of the behavior of the magnetic field. Some models were instead initialized with a poloidal magnetic field. To construct it we considered an azimuthal vector potential of the form $\boldsymbol{A} = A\hat{\boldsymbol{e}}_\phi$, with $A \propto p^2$ and p as the fluid pressure (Fig. 5.2). The magnitude of the toroidal and poloidal magnetic fields can be expressed in

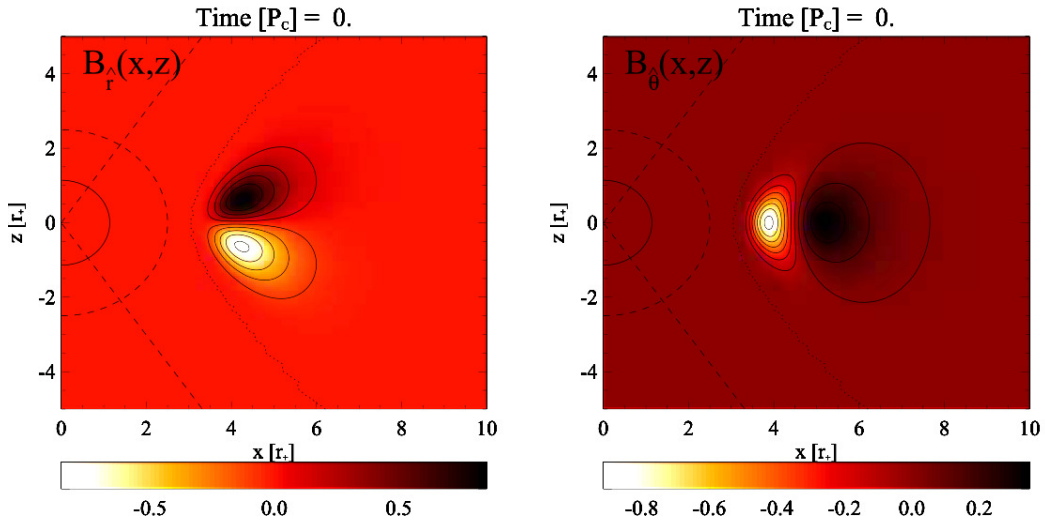

Figure 5.2.: Initial profiles of $B_{\hat{r}}$ and $B_{\hat{\theta}}$ for the models initialized with a purely poloidal magnetic field, normalized by the maximum of $|\boldsymbol{B_P}| \equiv \sqrt{B_{\hat{r}}^2 + B_{\hat{\theta}}^2}$.

terms of the orthonormal components as

$$B_T = B_{\hat{\phi}}, \tag{5.3}$$

$$B_P = \sqrt{B_{\hat{r}}^2 + B_{\hat{\theta}}^2}, \tag{5.4}$$

while the initial electric field $\boldsymbol{E}$ is set for all models to the ideal MHD value, i.e. $\boldsymbol{E} = -\boldsymbol{v} \times \boldsymbol{B}$.
Concerning the resistivity η, instead of imposing a constant value across the whole domain, we decided to modulate it so concentrate the diffusion within the disk and let the atmosphere behave as an ideal conducting fluid. For a given value of resistivity $\eta_{\rm disk}$ at the density maximum $\rho_{\rm max}$, we defined

$$\eta(r,\theta) = \eta_{\rm disk}\mathcal{S}_\eta(r,\theta), \tag{5.5}$$

where

$$\mathcal{S}_\eta(r,\theta) = \frac{\sqrt{\rho(r,\theta)} - \sqrt{\rho_{\rm min}}}{\sqrt{\rho_{\rm max}} - \sqrt{\rho_{\rm min}}}, \tag{5.6}$$

ρ is the disk rest mass density, and $\rho_{\rm min}$ is the density minimum reached in the atmosphere. The use of the IMEX schemes prevents us from explicitly imposing a vanishing resistivity in the atmosphere, since η appears in the denominator in Eq. (3.58). For this reason we imposed a constant value $\eta_{\rm atmo} = 10^{-5}$ in the atmosphere, which was low enough to match the code's numerical diffusion (for the given numerical setup) and hence provide the same results as in the ideal GRMHD case.

We now consider the spatial dependence of the dynamo parameter ξ. Eq. (2.98) requires that the sign of α changes at the passage through the equatorial plane, i.e. $\xi(r, \pi/2 + \theta) = -\xi(r, \pi/2 - \theta)$. Hence, given the value of the dynamo parameter at the density maximum $\xi_{\rm disk}$, we set

$$\xi(r, \theta) = \xi_{disk} \mathcal{S}_\xi(r, \theta), \tag{5.7}$$

where

$$\mathcal{S}_\xi(r, \theta) = \frac{\rho(r, \theta) \cos\theta}{(\rho \cos\theta)_{max}}, \tag{5.8}$$

and $(\rho \cos\theta)_{\rm max}$ is the maximum of the quantity $\rho \cos\theta$ in the computational domain. Once again, we want to confine the action of the mean-field dynamo within the disk. Therefore, we set $\xi_{\rm atmo} = 0$ in the atmosphere (since a vanishing ξ is compatible with Eq. (3.58)).

5.1.2. Results

Table 5.1 shows the models considered in this study and their parameters (initial magnetic field topology, resistivity and dynamo parameter).
Let us focus in detail on Model 1, which presents an initial toroidal field $\boldsymbol{B}_T$, $\eta_{\rm disk} = 10^{-3}$ and $\xi_{\rm disk} = 10^{-3}$. Fig. 5.3, Fig. 5.4 and Fig. 5.5 show the profiles at different times of the orthonormal components $B_{\hat{\phi}}$, $B_{\hat{r}}$, and $B_{\hat{\theta}}$. After an initial transient, all three components present an oscillatory pattern that drifts from the equatorial plane towards higher latitudes, i.e. an eigenmode of the system. We note that $B_{\hat{r}}$ and $B_{\hat{\theta}}$ start from a vanishing value and grow due to the α-effect. In Fig. 5.6 is displayed the evolution in time of the magnitude of the toroidal and poloidal components of $\boldsymbol{B}$. Both $\boldsymbol{B}_T$ and $\boldsymbol{B}_P$ increase exponentially with time at the same growth rate $\gamma_{\alpha\Omega} \simeq 0.39\ P_c^{-1}$. It is interesting to note that the toroidal field first decreases slightly before its exponential growth. This is due to the effect of the resistivity which diffuses $\boldsymbol{B}_T$, while the system starts to select the dominant eigenmode.
To quantify the periodicity and length-scale of the eigenmodes selected by the system, we construct so-called *butterfly diagrams*. We first parametrize the trajectory along which the fields drift, which are essentially half lines with origin at a point P_0 in the equatorial plane and inclined with respect to the equator by an angle χ_0. In terms of the horizontal and vertical coordinates (x, z) introduced in Figs. 5.3-5.5, we have

$$x = P_0 + |s| \cos\chi_0, \tag{5.9}$$
$$z = s \sin\chi_0, \tag{5.10}$$

where the parameter s has positive (negative) values for $\theta < \pi/2$ ($\theta > \pi/2$). We select values of P_0 and χ_0 for which the half lines cut the wave pattern in correspondence of the toroidal magnetic field peaks, and store the value of B_T as a function of s. We finally constructed the diagram by normalizing each one of these *slices* by the instantaneous maximum of the toroidal component and displaying them in chronological order. The result of this procedure is reported in Fig. 5.7. The migration of the toroidal field from the equatorial plane towards higher latitudes is self-evident, with a well-defined periodicity of $P_{\alpha\Omega} \simeq 9\, P_c$ and a regular inversion of the magnetic field polarity with time. Model 2, which shares the same parameters with Model 1 but has a reversed sign for $\xi_{\rm disk} < 0$, presents a different scenario (right panel of Fig. 5.7): the direction of migration of the patterns is opposite, since they form off the equator and drift towards it. This is consistent with the work of Roberts (1972), which relates the direction of the drift with the sign of the quantity $\alpha d\Omega/dr$, where Ω is the disk's angular velocity. Model 3 and 4 have the same value of η as Model 1, but a larger and smaller value for $\xi_{\rm disk}$ respectively. Hence, they have a different C_ξ than the original Model 1 we analyzed. The resulting butterfly diagrams show that for a more (less) effective mean-field dynamo action, the *dynamo waves* have a shorter (longer) period and develop on a smaller (larger) scale (see top row panels of Fig. 5.8).
In Model 5 and 6 (second row in Fig. 5.8) we varied C_Ω but kept C_ξ fixed, therefore modifying only the efficiency of the Ω-effect. For a higher (lower) value of $\eta_{\rm disk}$ the resulting eigenmode has a faster (slower) phase velocity, but it also diffuses more (less) across the disk. We initialized another four Models with a purely poloidal field $\boldsymbol{B}_P$, the same value $\eta_{\rm disk} = 10^{-3}$ as in Model 1 and different values for the dynamo parameter $\xi_{\rm disk}$ (see last four panels of Fig. 5.8). Differently from the previous models, they show an equatorial antisymmetry of the azimuthal magnetic field. The toroidal component produced by the initial dipolar $\boldsymbol{B}_P$ shows itself a dipolar symmetry, which is retained throughout the whole simulation. The same goes for the previous models: the initial symmetry of the magnetic field is left unchanged by the system.
These results show that, once the values of η and ξ are chosen, the system selects an eigenmode that conserves the initial parity of the magnetic field: from a field with dipolar symmetry ($\boldsymbol{B}_P$ in Fig. 5.2) we obtain a mode with symmetric components $B_{\hat{r}}$, and $B_{\hat{\theta}}$ and an antisymmetric component $B_{\hat{\phi}}$, while a quadrupolar field ($\boldsymbol{B}_T$ in Fig. 5.1) leads to the opposite.
The overall dependence on the magnitude and sign of $\xi_{\rm disk}$ is consistent with that of Models 1 to 4: higher ξ lead to faster waves on smaller scales, and viceversa.

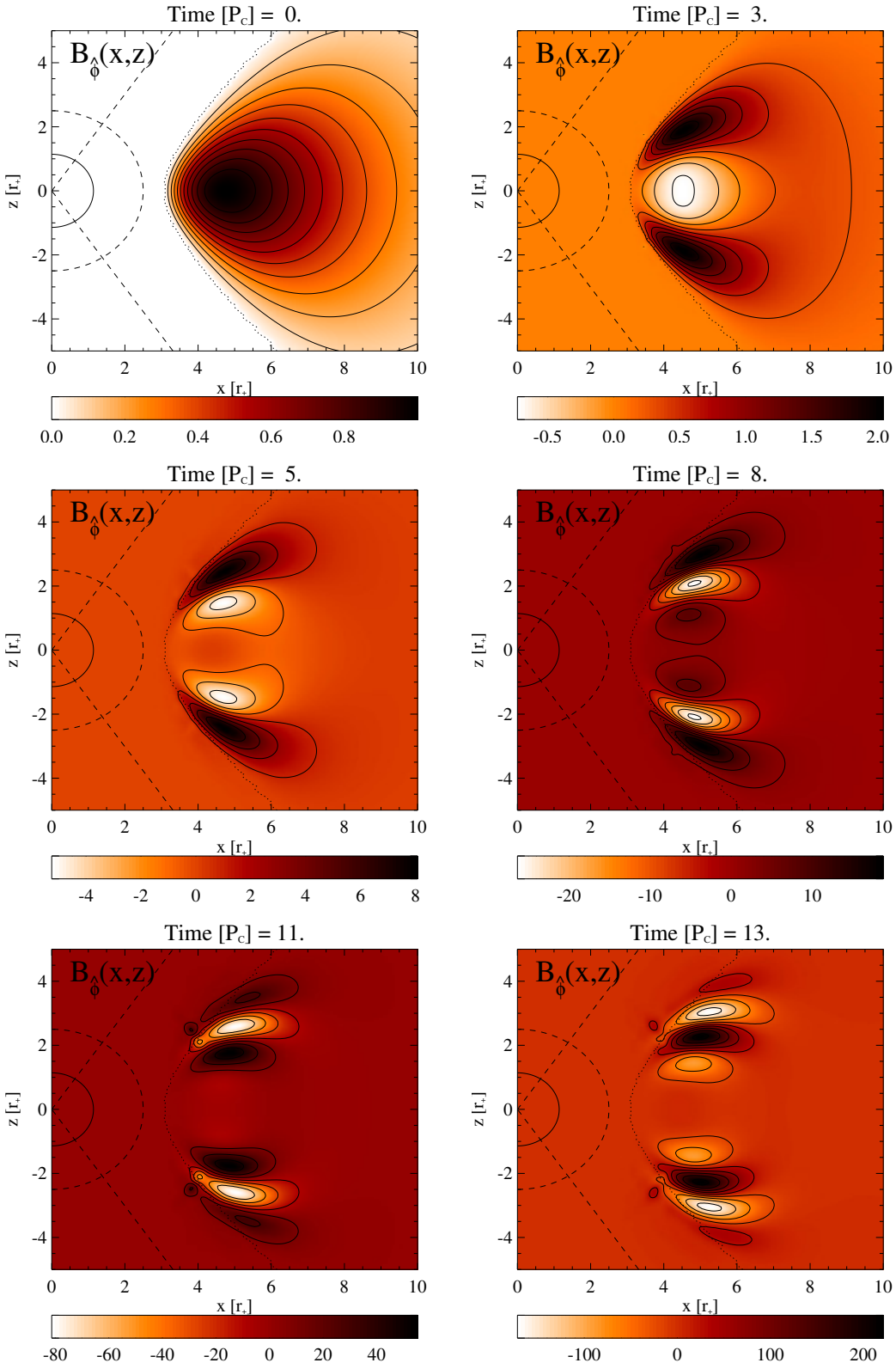

Figure 5.3.: Evolution of the $B_{\hat{\phi}}$ component in Model 1.

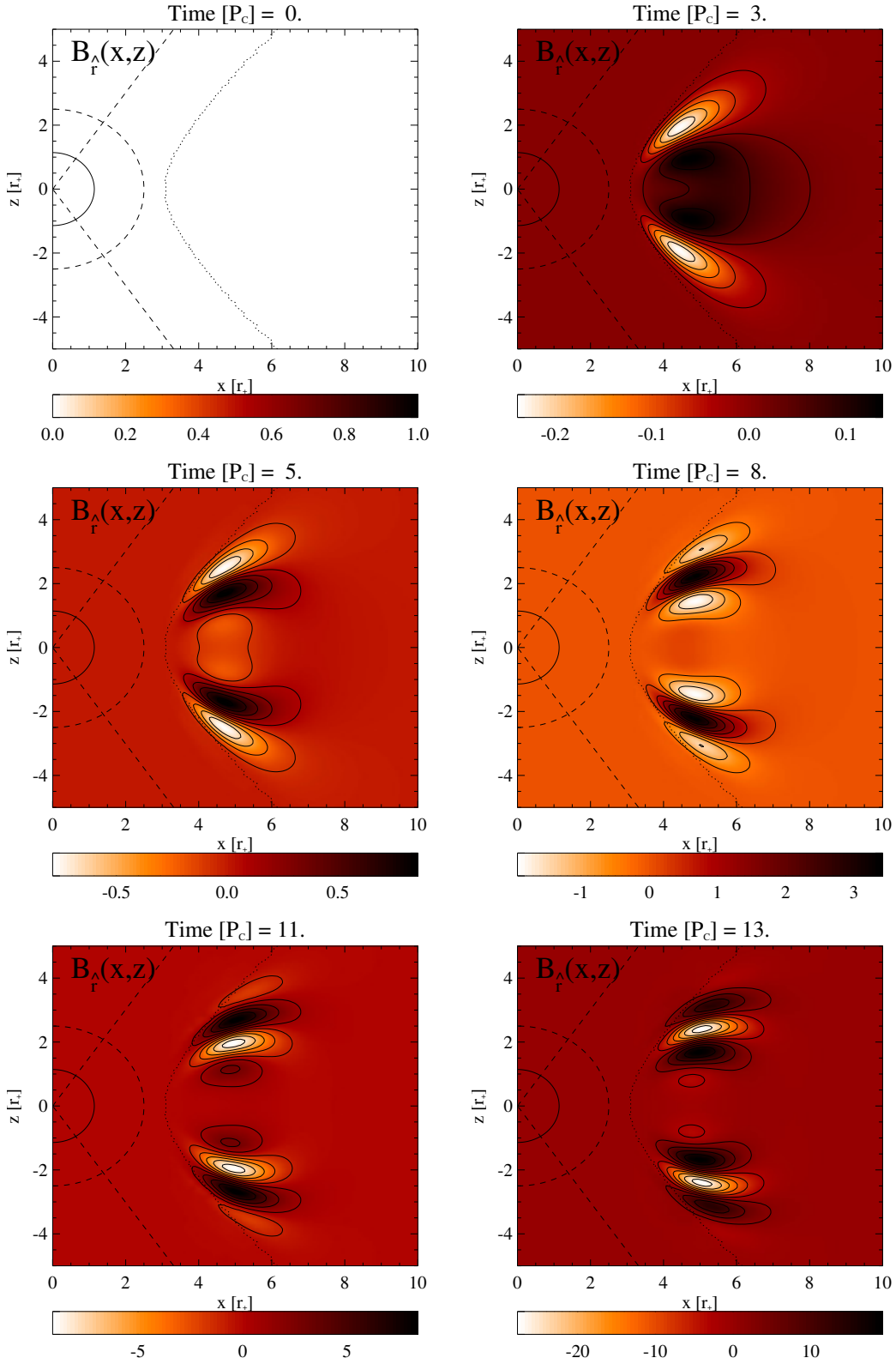

Figure 5.4.: Evolution of the $B_{\hat{r}}$ component in Model 1.

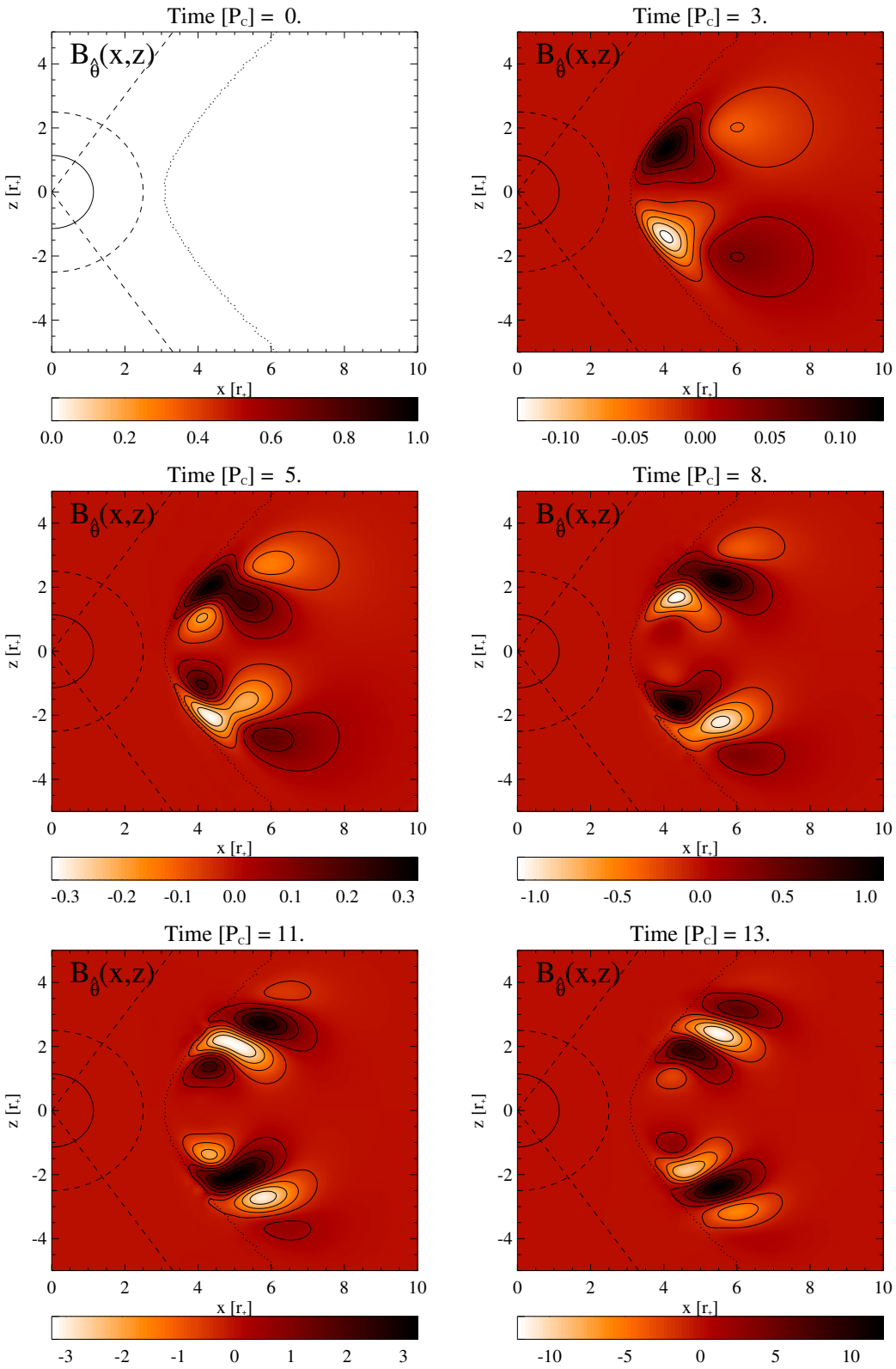

Figure 5.5.: Evolution of the $B_{\hat{\theta}}$ component in Model 1.

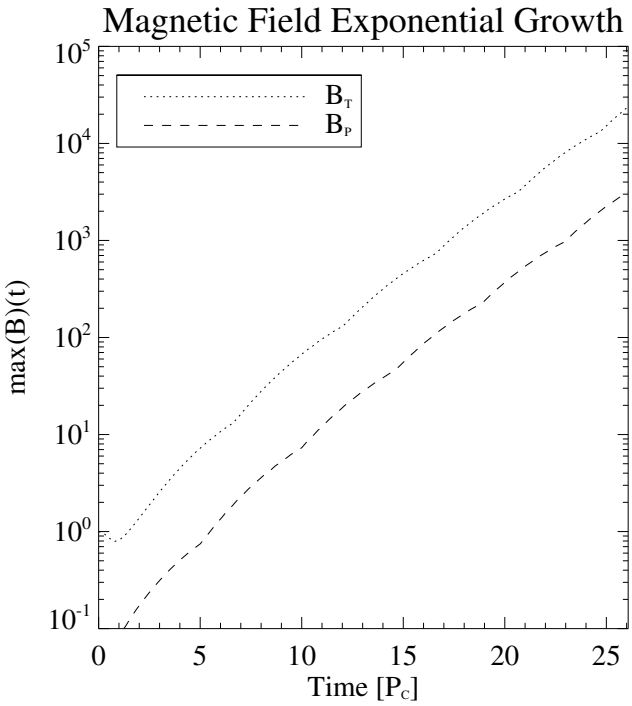

Figure 5.6.: Growth of the maximum values of $\boldsymbol{B}_T$ and $\boldsymbol{B}_P$ in Model 1. Both values are normalized to the maximum of the initial toroidal field $\boldsymbol{B}_T$, while time is reported in units of the disk's center orbital period P_c.

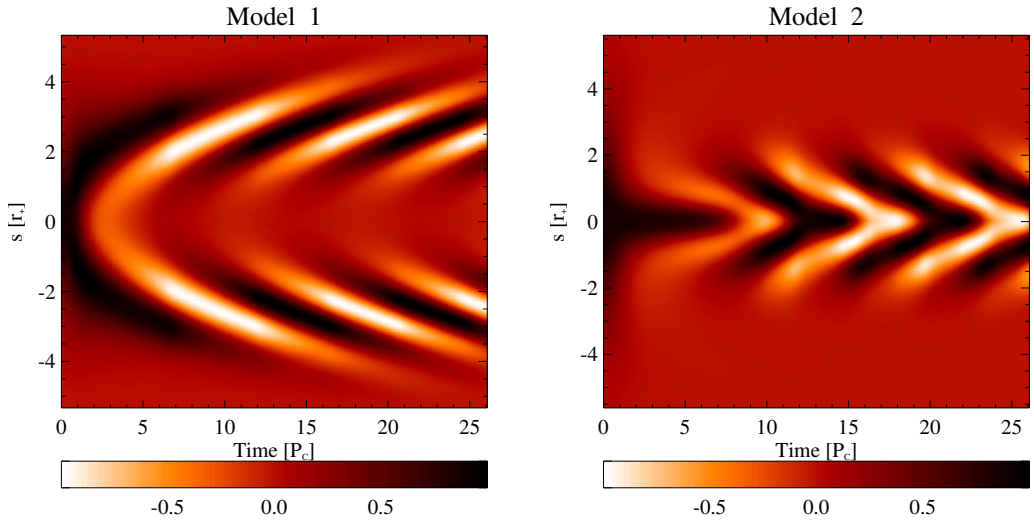

Figure 5.7.: Butterfly diagrams for Models 1 and 2, where is reported the value of $B_{\hat{\phi}}$ in corrispondence of the curve defined by Eq. (5.9), and normalized by its maximum at every time. Time is measured in units of P_c, while s is defined by Eq. (5.9).

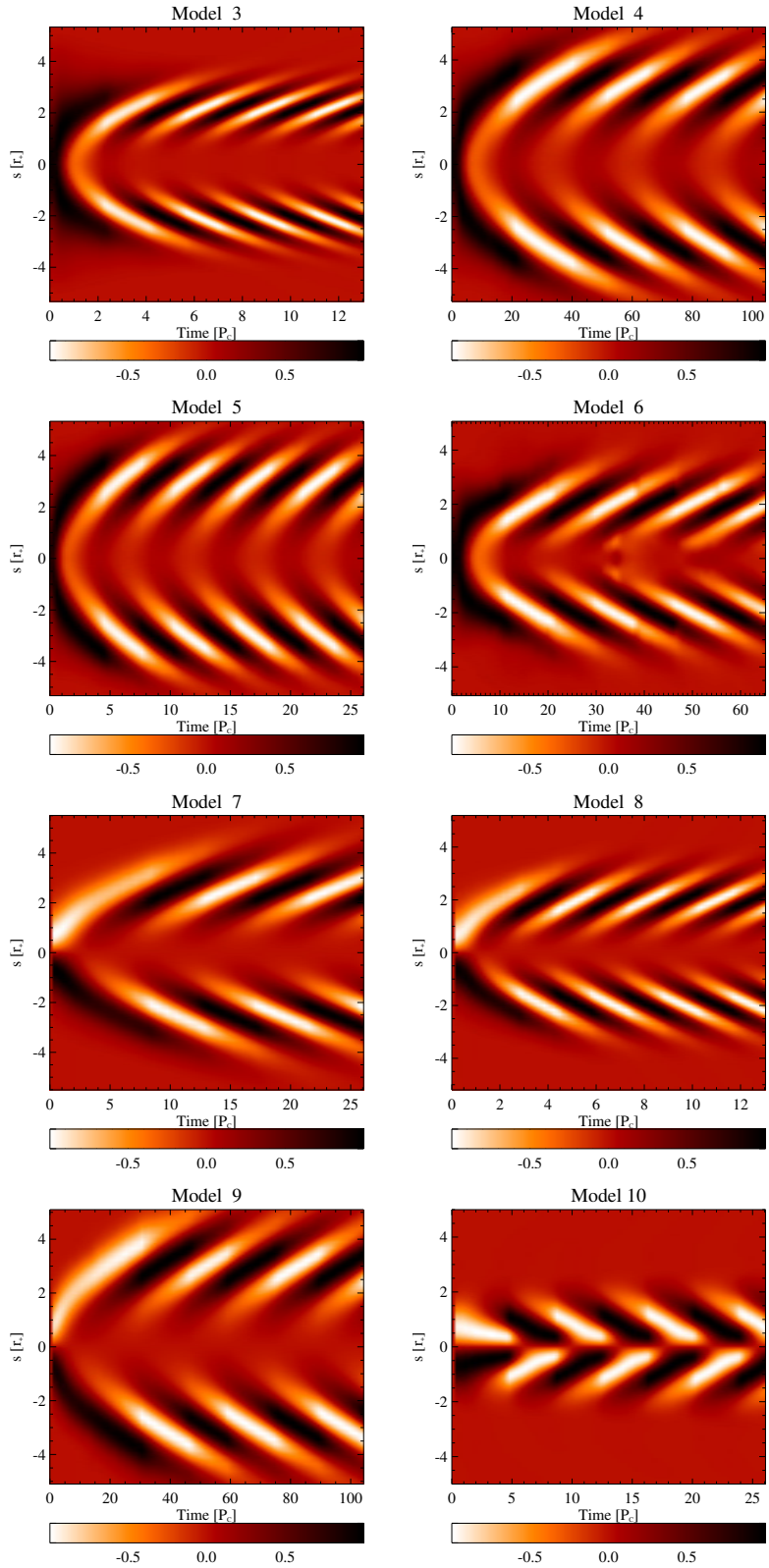

Figure 5.8.: Butterfly diagrams of Models 3 to 10, showing the value of $B_{\hat{\phi}}$ along s, implicitly defined by Eq. (5.9). The field is normalized by its maximum at every time, while time is measured in units of P_c.

Table 5.2.: Results from the $\alpha\Omega$-dynamo study.

	C_ξ	C_Ω	$\gamma_{\alpha\Omega}$	$P_{\alpha\Omega}$	s_{max}	$(B_P)_{max}/(B_T)_{max}$
Model 1	5	400	0.39	8.43	2.41	0.13
Model 2	-5	400	0.21	8.17	0.04	0.13
Model 3	25	400	1.58	2.77	2.05	0.42
Model 4	1	400	0.07	26.38	2.63	0.04
Model 5	5	80	0.39	5.79	3.35	0.22
Model 6	5	2000	0.22	16.46	1.82	0.06
Model 7	5	400	0.36	8.43	2.18	0.13
Model 8	25	400	1.48	2.77	1.83	0.37
Model 9	1	400	0.07	29.50	2.63	0.04
Model 10	-5	400	0.31	7.90	0.70	0.13

5.2. Three-dimensional magnetized tori

We describe now the results from a different set of simulations, which considered the same type of thick disk models as in the previous section. The main difference is that we used again an ideal Ohm's law (Eq. (3.48)) for a perfectly conducting plasma in absence of mean-field dynamo action, but evolved the full set of GRMHD equations (3.29) in a three-dimensional domain. This allows one to compare the dynamics of the PPI (inherently dynamic and non-axisymmetric) and the MRI (which is also a non-kinematic phenomenon). We first analyze the behavior of an unmagnetized disk to characterize the standard development of the hydrodynamic instability. We then add to the initial equilibrium a toroidal magnetic field of different strength and study the growth of non-axisymmetric global modes.

5.2.1. Disk model and numerical setup

In the following simulations we consider a Schwarzschild black hole of mass M and spin $a = 0$ in a spherical coordinate system (r, θ, ϕ), surrounded by a thick torus whose inner edge and center are located at $r_{\rm in} = 6.16\ M$ and $r_{\rm c} = 10.17\ M$, respectively. This choice sets the specific angular momentum of the disk to $l = 3.97$. The orbital period at the disk center is $P_c \sim 207\ M$. As for the previous models, we set the density at $r_{\rm c}$ to $\rho_{\rm c} = 1$ to avoid numerical underflows.
For the magnetized tori we initialize our simulations with the stationary solution provided by Komissarov (2006), keeping the same parameters as in the hydrodynamical models for black hole spin, disk inner edge and center location and density normalization. We vary the value of the central magnetization σ_c to investigate the role of the magnetic field strength on the system stability.
The atmosphere is initialized as a Michel's radial inflow (Michel, 1972), a stationary solution in the Schwarzschild metric determined by the adiabatic index $\Upsilon = 4/3$ and the value of the atmospheric density at distance $r_{\rm c}$, which we set to a value $\rho_{\rm atm} = 10^{-6}$. To provide stability for the integration, we set a numerical floor value for the density equal to $\rho_{\rm fl} = 10^{-9}$.
We adopt Kerr-Schild coordinates (McKinney and Gammie, 2004) to allow for an inner radial boundary inside the black hole event horizon located at a radius $r_h = 2\ M$, thus preventing numerical artifacts due to boundary effects that could otherwise propagate through the domain and affect the simulation at $r > r_h$. In radial direction the numerical domain ranges from $r_{\rm min} = 0.97 r_h$ to $r_{\rm max} = 100\ M$, with outflow boundary conditions applied at both radial extrema. The radial mesh is refined to increase the resolution towards the black hole event horizon as described by Eq. (5.1) with $\psi = 10$.
The polar domain extends from $\theta_{\rm min} = 0.001$ to $\theta_{\rm max} = \pi - 0.001$ with imposed

reflecting boundaries. We made this choice because we are now considering a dynamical problem: we can no longer restrict our domain to a small box containing the whole disk and excluding a large fraction of the atmosphere as in the kinematic simulations. To better resolve the disk, the polar mesh is refined towards the equatorial midplane by relating the variable y_i evenly spaced in the range $[0, 1]$ and the actual polar grid points θ_i as

$$\theta_i = \frac{\pi}{2}[1 + (1 - \zeta)(2y_i - 1) + \zeta(2y_i - 1)^n], \tag{5.11}$$

where $\zeta = 0.6$ and $n = 29$. This gives a roughly constant and fine grid spacing across the disk and a rapidly decreasing resolution towards the rotational axis (Noble et al., 2010).
Finally, we consider the full azimuthal range $\phi \in [0, 2\pi]$ with uniformly distributed cells and periodic boundaries to be able to resolve global azimuthal modes with mode number $m = k_\phi r = 1$, which are expected to develop and to be also the fastest growing modes for the PPI in our disk model.
To trigger the growth of non-axisymmetric modes we introduce a small perturbation $\delta v^{\hat{\phi}}$ of the equilibrium azimuthal velocity $v_0^{\hat{\phi}}$, with either random noise or cosine waves of the form:

$$\delta v^{\hat{\phi}} = A v_0^{\hat{\phi}} \cos(m\phi), \tag{5.12}$$

with $m = 1, ..., 5$ and amplitudes A ranging from 10^{-6} to 10^{-2} depending on the simulation.
To perform the computationally very expensive 3D simulations we make use of the three-dimensional `MPI` domain-decomposition scheme introduced in Chapter 4. The batch jobs were run in parallel on (up to) 1728 cores, which leads to subdomains of $\sim 20^3$ grid points for a grid resolution of 256^3. For these simulations we employed both the Hydra and SuperMuc clusters, using the HLL Riemann solver coupled to a PPM reconstruction algorithm and a 2^{nd} order explicit Runge-Kutta integration scheme. The overall lower accuracy order (with respect to the kinematic simulations) proved to be necessary in order to complete a sufficient number of runs for a sufficiently long integration time.

5.2.2. Diagnostics

We now introduce the quantities that we calculate from each simulation to probe the dynamical evolution of the models and determine the relative importance of the PPI and MRI in these models.

Table 5.3.: List of the models considered in our study, where N_ϕ is the number of grid points in azimuthal direction, $A(v^{\hat{\phi}})$ is the amplitude of the initial perturbations in $v^{\hat{\phi}}$, and σ_c is the initial value of the magnetization at the center of the disk. The last four models are at the center of the discussion in Section 5.

	N_ϕ	$A(v^{\hat{\phi}})$	Excitation	$\sigma_c/10^{-2}$
H64r3	64	10^{-3}	Random	0
H256r4	256	10^{-4}	Random	0
H32m14	32	10^{-4}	m=1	0
H64m14	64	10^{-4}	m=1	0
H128m14	128	10^{-4}	m=1	0
H256m14	256	10^{-4}	m=1	0
H64m22	64	10^{-2}	m=2	0
H64m32 8	64	10^{-2}	m=3	0
H64m42 9	64	10^{-2}	m=4	0
H64m52 10	64	10^{-2}	m=5	0
H256r3	256	10^{-3}	Random	0
T256r3s12	256	10^{-3}	Random	1
T256r3s32	256	10^{-3}	Random	3
T256r3s11	256	10^{-3}	Random	10

Power of azimuthal modes

For any given azimuthal number m we calculate the power contained in an azimuthal mode for a general quantity Q as

$$\mathcal{P}_{m,Q}(r,\theta,t) = \left| \frac{1}{2\pi} \int_0^{2\pi} Q e^{im\phi} \mathrm{d}\phi \right|^2 , \tag{5.13}$$

We then average the power over both the polar angle θ and the radial direction across the whole computational domain:

$$\mathcal{P}_{m,Q}(t) = \langle \langle P_{m,Q} \rangle_\theta \rangle_r . \tag{5.14}$$

We weigh these averages by the rest mass density ρ for $Q \in \{u^{\hat{\phi}}, u_A^{\hat{\phi}}\}$, to avoid overestimating the contribution of the rarefied atmosphere enveloping the disk and at the same time computing quantities that relate respectively to the azimuthal components of kinetic energy and magnetic energy. We use different normalizations depending on the specific quantity considered. For $Q = \rho$ we normalize by $\langle \mathcal{P}_{0,\rho} \rangle (t = 0)$, i.e. the initial power in the axisymmetric density mode, while for $Q \in \{u^{\hat{\phi}}, u_A^{\hat{\phi}}\}$ we use $\langle P_{0,c_s} \rangle (t = 0)$, where

$$c_s = \frac{\Upsilon p}{\rho h} \tag{5.15}$$

is the relativistic sound speed. This represents a more natural unit for both the fluid and the Alfvén velocity than their initial values.
With these diagnostics we estimate growth rates and saturation levels. To visualize the time evolution of the relative importance of the various length-scales resolved by the numerical simulations we also construct spectrograms. At any given time t, we consider the power (Eq. (5.14)) of modes with azimuthal number up to $m = 50$ by plotting it in a m vs. time diagram. By averaging over the full duration of the simulations, we also compute Fourier spectra to characterize the power distribution.
To collect information on the frequency components present in the fastest growing PPI mode we also construct frequency-radius diagrams. We consider the complex amplitude of the $m = 1$ mode of the density in the equatorial plane (since most of the dynamics takes place in this region). For each radius r we compute the Fourier transform in the frequency domain, obtaining the $\omega - r$ diagrams shown in Fig. 5.17.

Turbulence and accretion

To keep track of the development of turbulence in the system we consider the evolution of the turbulent kinetic energy density, defined as the difference between the total kinetic energy density and the component due to the mean orbital motion of the fluid. Integrating this quantity over the computational volume V we obtain:

$$K_{\mathrm{turb}} = \int_V \rho(u - \langle u^{\hat{\phi}} \rangle_\phi)^2 \, \mathrm{d}V, \tag{5.16}$$

where the operator $\langle\rangle_\phi$ represents an average over the azimuthal angle ϕ and $\mathrm{d}V = \sqrt{\gamma}\, \mathrm{d}r\, \mathrm{d}\theta\, \mathrm{d}\phi$ is the covariant volume element.
Another set of quantities useful to probe the dynamical evolution of the system are the $r - \phi$ components of the Reynolds and Maxwell stress tensors, defined respectively as:

$$W^{\hat{r}\hat{\phi}}_{\mathrm{Re}} = \rho\, \delta u^{\hat{r}}\, \delta u^{\hat{\phi}}, \tag{5.17}$$

$$W^{\hat{r}\hat{\phi}}_{\mathrm{Ma}} = B^{\hat{r}}\, B^{\hat{\phi}}. \tag{5.18}$$

We compute their volume averages by considering only those regions of the computational domain where the rest mass density ρ exceeds a threshold value set to $\rho_{\mathrm{th}} = \sqrt{\rho_{\mathrm{c}}\, \rho_{\mathrm{atm}}}$ to track the dynamics of the disk and exclude that of the atmosphere.
Still related to the stresses, we compute the disk α parameter (not to be confused with the lapse function) as the ratio of the volume average of the total stress

$W^{\hat{r}\hat{\phi}}_{\rm tot} = W^{\hat{r}\hat{\phi}}_{\rm Re} + W^{\hat{r}\hat{\phi}}_{\rm Ma}$ and the volume average of the thermal pressure:

$$\alpha = \frac{\langle W^{\hat{r}\hat{\phi}}_{\rm tot}\rangle_V}{\langle p\rangle_V}. \tag{5.19}$$

As a further diagnostics of the efficiency of angular momentum transport in the disk, and thus of the overall accretion process, we also monitor the evolution of the radial distribution of the disk orbital angular velocity Ω. The radial dependence of Ω is usually described with a power-law:

$$\Omega \propto r^{-q}, \tag{5.20}$$

where the parameter q can range from 3/2 (for a Keplerian disc) to 2 (constant specific angular momentum). However, in the relativistic case and for a non-rotating black hole $\Omega = -l g_{tt}/g_{\phi\phi} = l(r-2)/r^3$, and the value $q = 2$ can be assumed only if the disk extends sufficiently far from the black hole. Since our disk model extends from $r_{\rm in} = 6.16\ M$ to $r_{\rm out} = 21.6\ M$, the initial local value of the slope ranges from $q(r_{\rm in}) = -1.52$ to $q(r_{\rm out}) = -1.90$. For this reason, instead of q we monitor the evolution of the quantity:

$$\tilde{q} = 2 - \left|\frac{{\rm d}\log l}{{\rm d}\log r}\right|, \tag{5.21}$$

which is evaluated performing a least-squares fit of the power law describing the radial dependence of the specific angular momentum l.

Convergence

An important aspect to consider in any numerical experiment is its convergence, i.e. whether or not the results depend on the grid resolution.
For a simulation involving magnetized accretion flows the key aspect that needs to be properly resolved is the MRI turbulence that appears whenever a differentially rotating fluid is threaded by a magnetic field of any topology. Following Hawley et al. (2011) we define two quality metrics as ratios of the characteristic wavelength of the MRI mode $\lambda_{\rm MRI} = 2\pi|u_{\rm A}|/\Omega$ (which corresponds to the distance traveled by an Alfvén wave during an orbital period) and the grid zone size, that is:

$$Q_\theta = \frac{\lambda_{\rm MRI}}{\Delta x^{\hat{\theta}}} = \frac{2\pi|u_{{\rm A}z}|}{\Omega\Delta\theta\sqrt{\gamma_{\theta\theta}}}, \tag{5.22}$$

$$Q_\phi = \frac{\lambda_{\rm MRI}}{\Delta x^{\hat{\phi}}} = \frac{2\pi|u_{{\rm A}\phi}|}{\Omega\Delta\phi\sqrt{\gamma_{\phi\phi}}}, \tag{5.23}$$

where $u_{\rm A} = B/\rho h$ is the Alfvénspeed. Hawley et al. (2011) suggest that $Q_\theta \gtrsim 10$ and $Q_\phi \gtrsim 20$ should provide a sufficiently good description of the non-linear

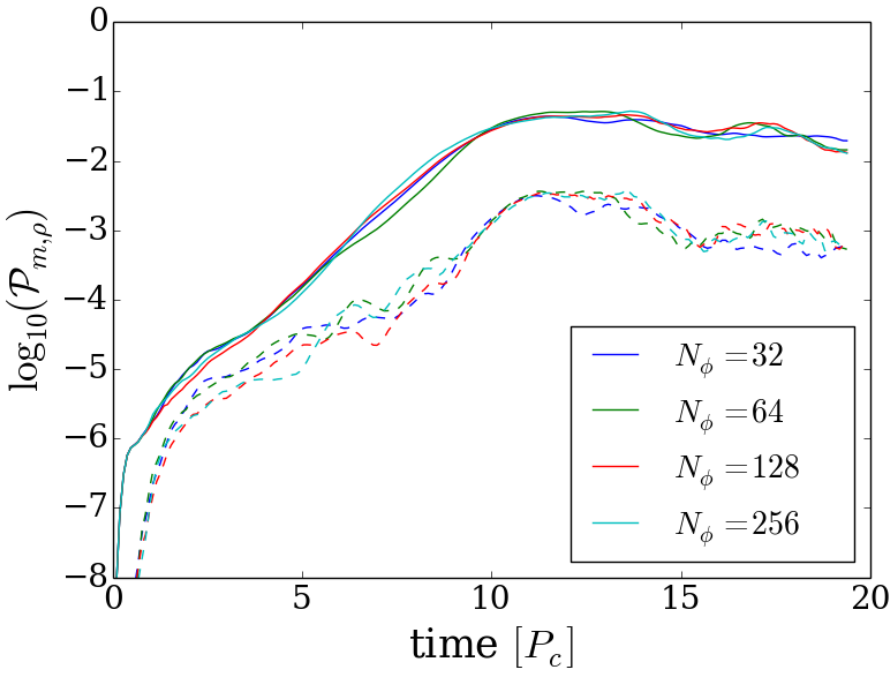

Figure 5.9.: Time evolution of the power in density for the $m = 1$ (solid curves) and $m = 2$ (dashed curves) modes, as computed from Eq. (5.14) for models H32m14 to H128m14.

phase of MHD turbulence. Since we use the Harten-Lax-van Leer Riemann-solver instead of the more dissipative Lax-Friedrichs scheme, we expect to have good convergence behavior even for those simulations that marginally fulfill these above criteria. Note, however, that the recent stratified shearing box simulations of Ryan et al. (2017) suggest that none of the current simulations may actually be converged, even at much higher resolution than achievable in a global model.

5.2.3. Results and discussion

Hydrodynamic disk

We first focus on the development and saturation of the PPI in absence of magnetic fields to have an initial benchmark for a later comparison with the results from magnetized models. As shown in Table 5.3, we performed a set of simulations that differ by resolution in the azimuthal direction, and amplitude and spectrum of the initial perturbation. We followed the evolution of these models up to 20 orbital periods at the disk center, which was enough time for the hydrodynamical instability to reach saturation in terms of azimuthal mode power.
Our results show that the $m = 1$ azimuthal mode is the fastest growing one.

Therefore it was selected by the system independently of the initial perturbation spectrum. Whether we started by exciting a specific mode ($m = 1, 2, 3, 4, 5$) or with a random perturbation, the $m = 1$ mode always ended up being the fastest growing one and having the highest saturation level.
We ran a series of simulations with the same monochromatic $m = 1$ perturbation but with different resolutions in the azimuthal direction (model H32m14 to H256m14). Fig. 5.9 shows the time-evolution of the azimuthal power in density for the $m = 1$ and $m = 2$ modes. Even with a modest resolution of 32 points, `ECHO` is capable of capturing the dynamical evolution of the PPI, since the most unstable mode has a quite large wavelength. Fig. 5.9 also shows the linear phase of the instability during the first ten orbital periods, and the different growth rates and saturation levels for the two modes. Particularly evident is the large ratio of the final powers in the $m = 1$ and $m = 2$ modes.
The minimum resolution required to properly resolve the fastest growing mode

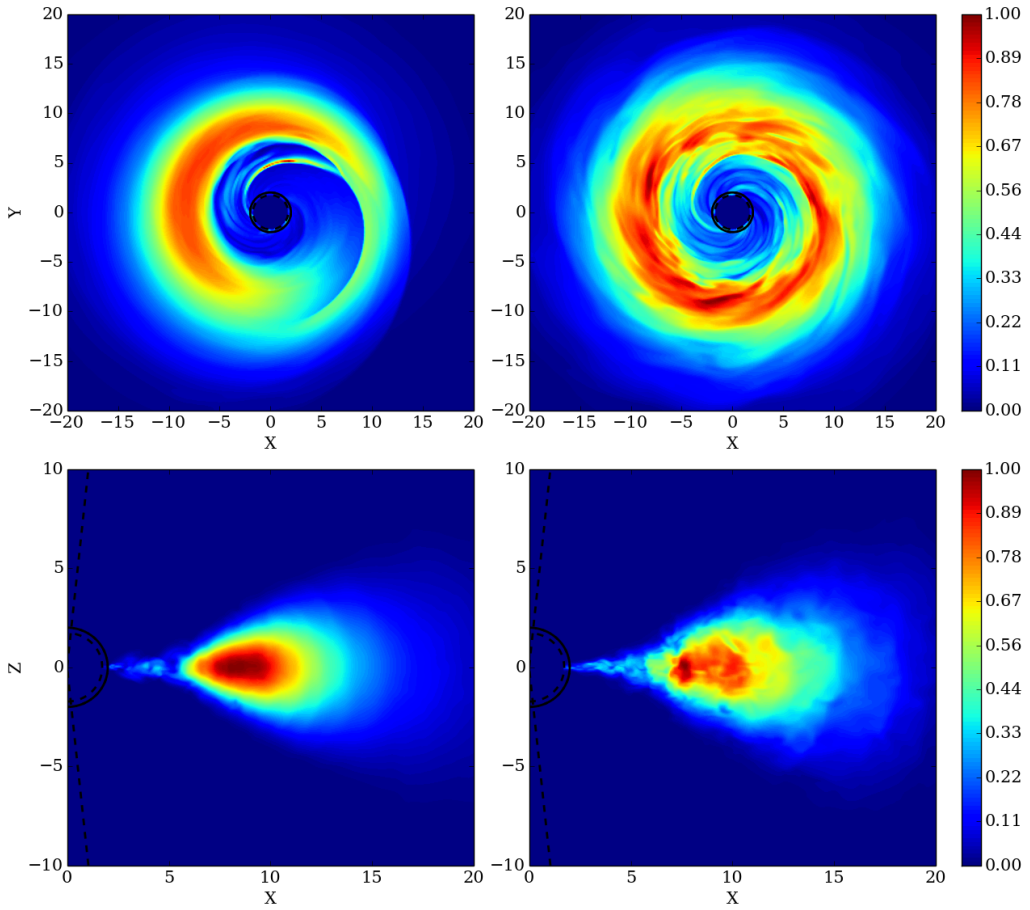

Figure 5.10.: Equatorial (top) and meridional (bottom) cuts of the rest mass density ρ for model H256r3 (left) and T256r3s12 (right) at $t = 3000 \simeq 15\ P_c$. The value of ρ is normalized to 1 in each plot.

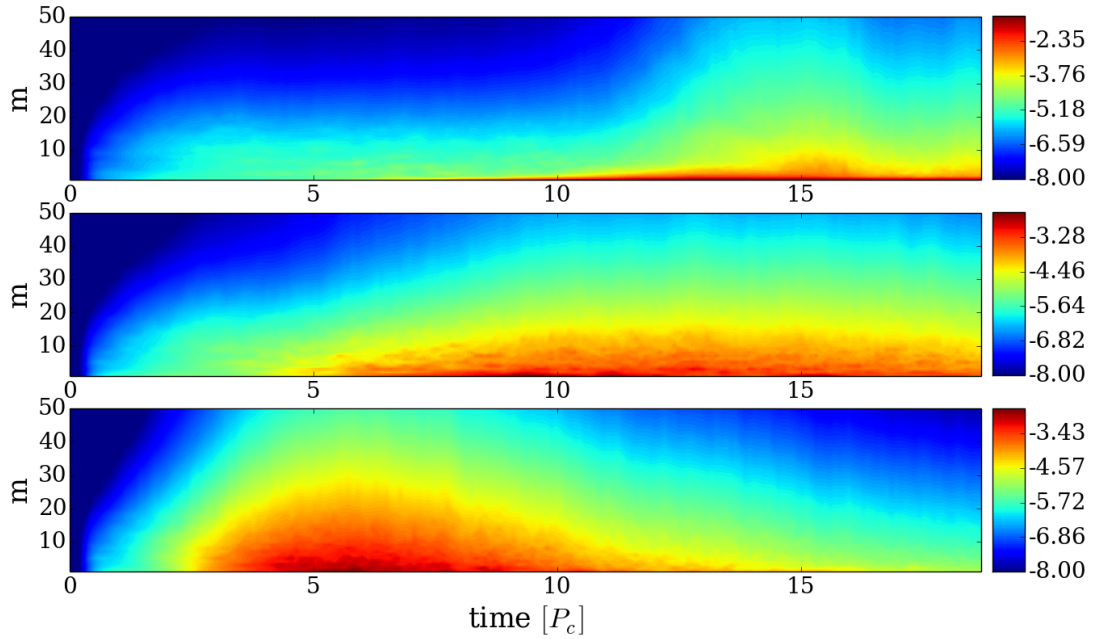

Figure 5.11.: Rest mass density spectrograms of the azimuthal mode power, color-coded in logarithmic scale. The upper panel refers to model H256r3 , the middle one to model T256r3s12 , and the bottom one to model T256r3s11 .

of the PPI turns out to be much higher in radial direction than in azimuthal direction (i.e. higher than 32 points), because the $m = 1$ mode developing from our wide torus model is not (as in the case of slender tori) the *principal mode*. It is instead the outcome of the interaction between a pressure wave in the outer part of the disk and an edge wave from the interior, i.e. it is a *compressible mode*. As a consequence, this mode presents multiple nodes in radial direction which require an adequate radial resolution. If one does not have sufficient resolution, one systematically underestimates the instability growth rates (see Blaes and Hawley (1988) for a detailed discussion).
Fig. 5.10 (top left panel) shows an equatorial slice of the rest mass density for model H256r3 after about 15 orbital periods. The dominant $m = 1$ mode is clearly visible as an overdensity that corotates with the disk, while the flow still maintains overall a smooth profile. The region in between the black hole horizon and the disk's inner edge is relatively depleted of mass, apart from an inspiraling flow that detached from the main body of the disk.
From the spectrogram in Fig. 5.11 (first panel) it is clear that the $m = 1$ mode dominates over the others since very early times, and no other small-scale perturbation grows as much during the linear phase of the instability. After 10 orbital periods, a further deposition of energy on smaller scales occurs presumably because of a non-linear interaction, but the $m = 1$ mode remains the most

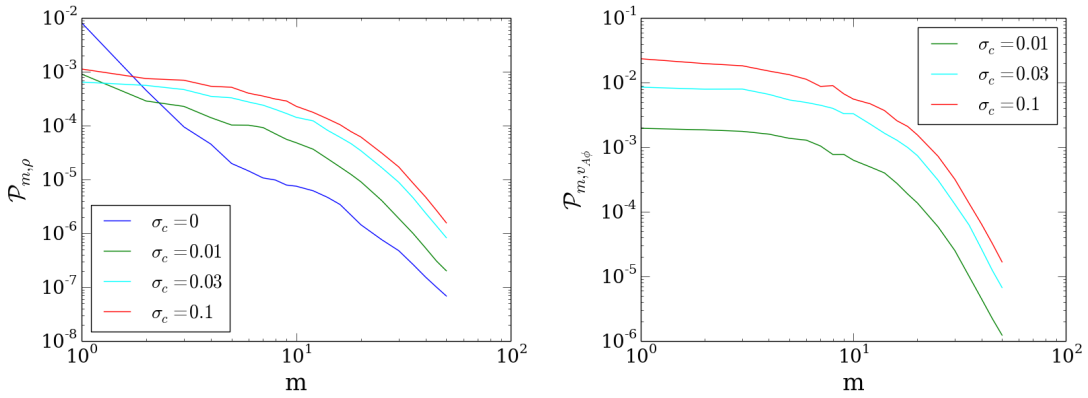

Figure 5.12.: Time-averaged equatorial rest mass density (left panel) and azimuthal Alfvén velocity (right panel) spectra as a function of azimuthal number m.

important one. This interpretation is confirmed by the density power spectrum in the left panel of Fig. 5.12, which shows also a clear excess of power in low order modes, peaking at m=1.

Magnetized discs

We now consider the effect of a weak toroidal magnetic field. In order to avoid transients, we chose the analytical solution provided by Komissarov (2006) instead of superimposing a magnetic field to the hydrodynamical solution. The drawback of such an approach is that the profile of gas density and pressure depends on the strength of the initial magnetic field. We checked that differences in these quantities between initially magnetized models and unmagnetized ones never exceeded a few percents in gas density and pressure for all our models. Therefore we consider the differences to be dynamically insignificant.
As illustrated by the right panels of Fig. 5.10, the distribution of rest mass density in the magnetized models is much less smooth than in the hydrodynamic models, and it does not show a self-evident type overdensity. The flow consists of much smaller scales in the magnetic models, and both the equatorial and meridional slices indicate MHD turbulence triggered by the MRI.
The time-evolution of the azimuthal mode power (Fig. 5.13) in the magnetized models (green, red and cyan curves with increasing magnetic field strength) reveals an earlier growth of low order modes, without a clear distinction between the $m = 1$ and $m = 2$ modes as in the hydrodynamic case. This behavior is confirmed by the spectrograms in Fig. 5.11, that show a much broader range of excited large-scales modes in the magnetized case.

The time-averaged density spectra shown in the left panel of Fig. 5.12 provide a more quantitative confirmation of this trend. The hydrodynamic model H256r3 develops predominantly large-scale modes, with a steep power-law decline

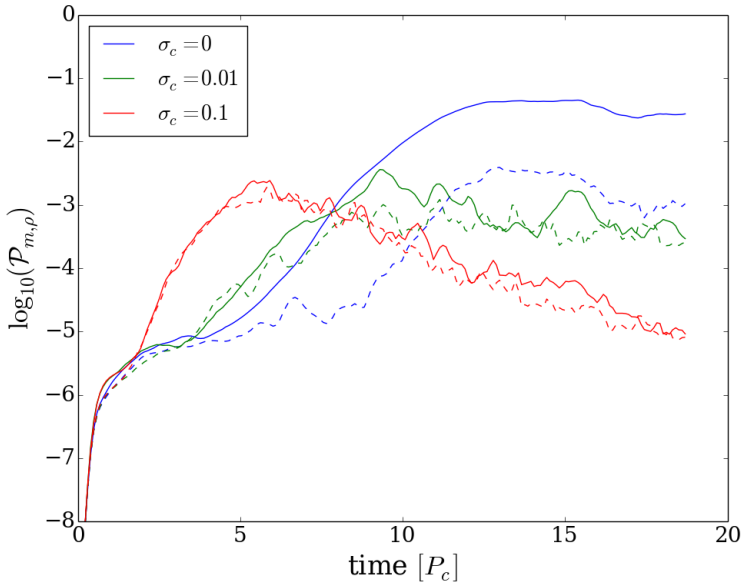

Figure 5.13.: Power in density for the $m = 1$ (solid curves) and $m = 2$ (dashed curves) modes for models H256r3 (blue), T256r3s12 (green) and T256r3s11 (red).

from the $m = 1$ mode to $m \approx 5$, followed by a shallower decline up to $m = 10$ and again a steep drop. The magnetized models have no strong excess of power at large scales, but they also show a fall for $m \gtrsim 10$. Only in the model with a magnetization of $\sigma_c = 10^{-2}$ there is still a small excess of power in the $m = 1$ mode, but otherwise the spectrum behaves quite similarly to the ones of the other magnetized discs. The spectra computed from the orbital Alfvén velocity show instead no appreciable difference in their shape for different values of the magnetization (right panel of Fig. 5.12), but they display a systematic shift of the curves with the magnetic field strength.
All the models we considered produce accretion onto the central black hole, but at different times and in different ways. In the hydrodynamic disk the development of the PPI is the sole responsible for angular momentum transport, hence accretion. After 10 orbital periods, when the $m = 1$ mode approaches its maximum amplitude, the kinetic energy and stresses are large (Fig. 5.14), which consequently leads to a significant redistribution of angular momentum (see the evolution of the parameter q in Fig. 5.15) and mass loss (almost 30% of the disk initial mass). A space-time diagram of the radial profile of the specific angular momentum l at the equator (top panel in Fig. 5.16) clearly shows that the waves that constitute the unstable mode are increasing l outside the corotation radius and decreasing it in the inner region of the disk, in a non-local fashion.

The situation is quite different in the magnetized models. The accretion is triggered at much earlier times (after only 2 orbital periods for the highly mag-

netized model) with a steeper increase of turbulent kinetic energy and stresses. In model T256r3s12 the Reynolds and Maxwell stresses are at the beginning of their rise quite similar, but then the magnetic component takes over. For model T256r3s11 Maxwell stresses dominate from the very beginning and during the whole simulation. Consequently, accretion is enhanced and a higher mass loss

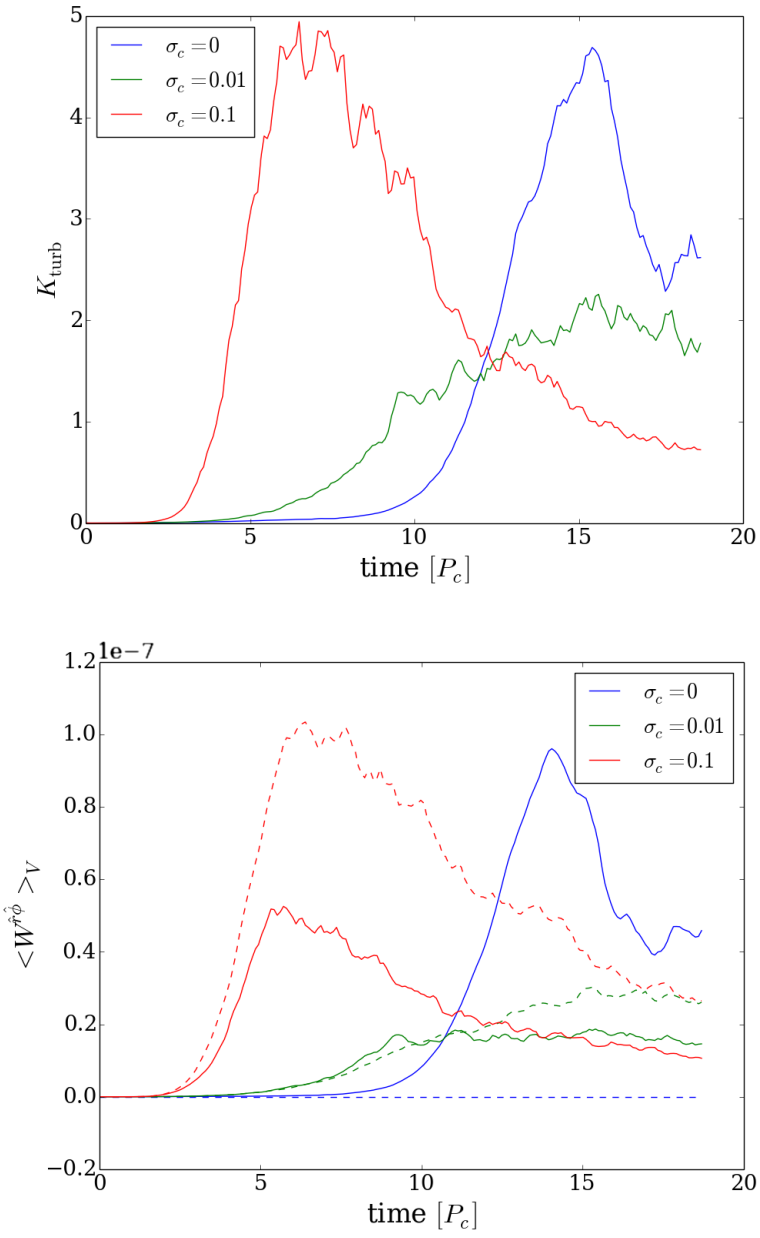

Figure 5.14.: Turbulent kinetic energy (top panel) and stresses (bottom panel, Reynolds in solid curve, Maxwell in dashed curve) for models H256r3 , T256r3s12 and T256r3s11 (blue, green, and red as in the previous figure).

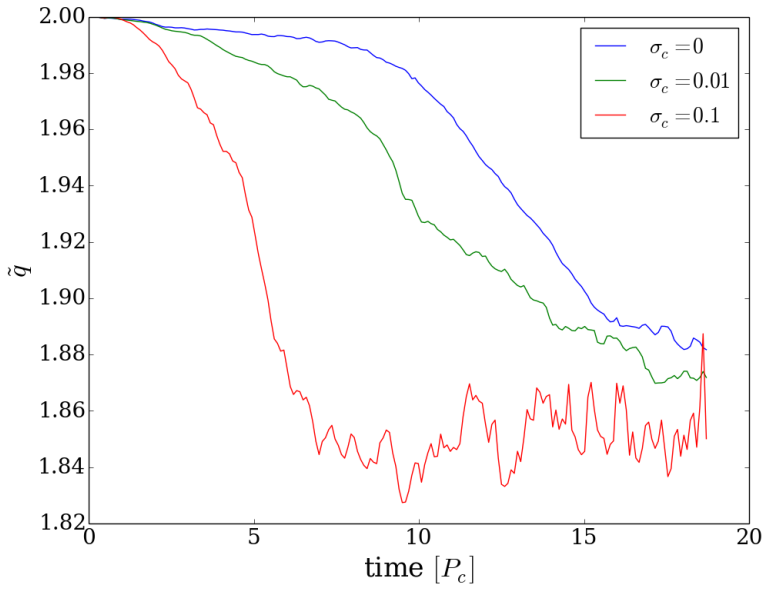

Figure 5.15.: Slope parameter $\tilde{q}$ in the equatorial plane for models H256r3 , T256r3s12 and T256r3s11 .

results, leading in the highly magnetized model to a dramatic decrease of the disk mass down to 30% of its initial value. This strong mass loss is responsible for the drop in power of the azimuthal modes in density shown in Fig. 5.13 (red curves).
Concerning the angular momentum distribution, Fig. 5.15 validates these findings by showing a faster and earlier decrease of $\tilde{q}$ (see Eq. (5.21)) and also a lower saturation value with respect to the hydrodynamic case. Space-time diagrams (middle and bottom panels of Fig. 5.16) show how angular momentum is transported outwards from the inner regions of the disk much faster than in the absence of a magnetic field. There is no substantial trace of a global deposition of angular momentum starting from the outer region of the disk and proceeding inwardly (apart once again for the low magnetization model T256r3s12 , where after 7 orbital periods there in a small increase of l starting at the outer edge of the disc).

Mode frequency

As we have seen in Chapter 2, the mode selected by the PPI as the fastest growing one is characterized not just by the azimuthal number $m = 1$, but also by a specific angular frequency ω, which we can measure and directly compare with the disk rotation rate Ω.

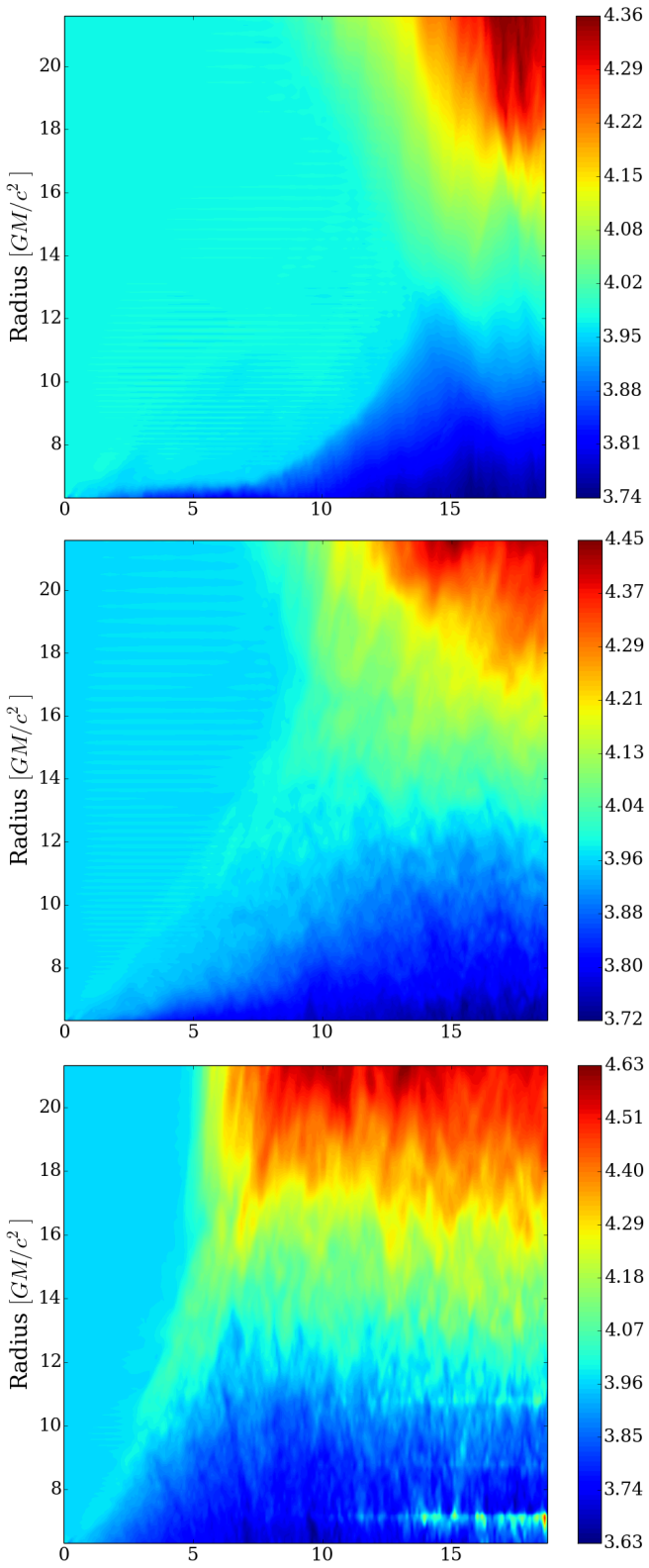

Figure 5.16.: Space-time diagrams of the azimuthally averaged equatorial radial distribution of the specific angular momentum l for models H256r3 (top), T256r3s12 (middle) and T256r3s11 (bottom).

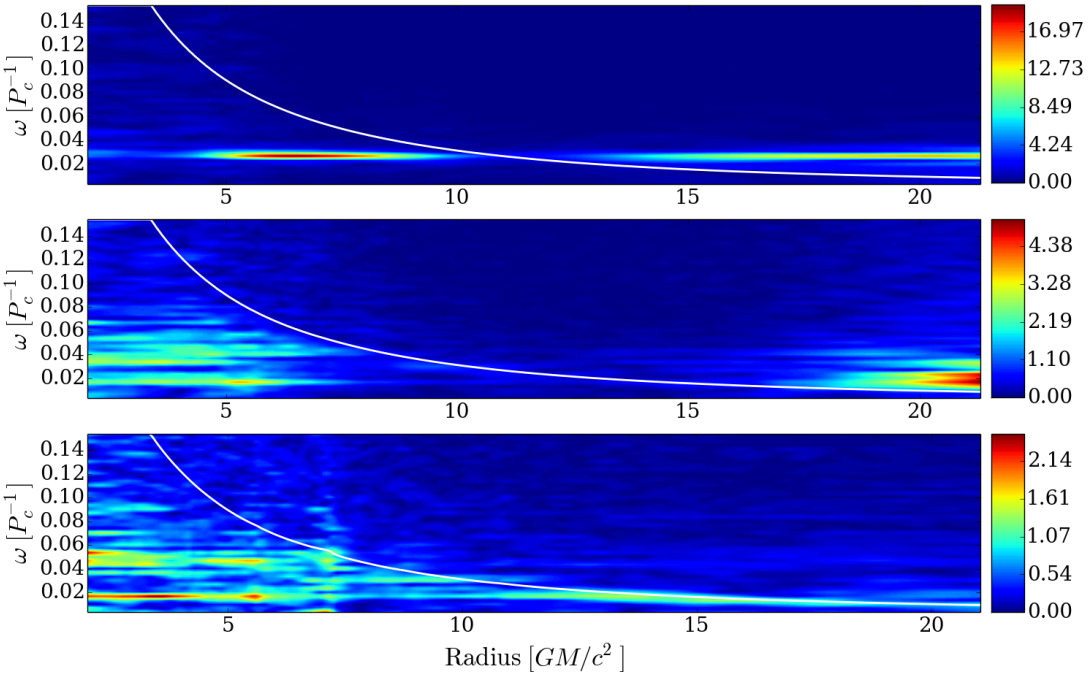

Figure 5.17.: Amplitude of the $m = 1$ mode frequency components in a ω vs. radius diagram calculated from the rest mass density ρ. The white curve represents the azimuthally and time averaged equatorial orbital frequency profile. All quantities are computed from the last nine orbital periods of the disk.

The first panel of Fig. 5.17 shows clearly the presence of a specific spectral component at $\omega_0 \simeq 0.03\ P_c^{-1}$ in the hydrodynamic model, which represents the $m = 1$ mode selected by the PPI. Both positive and negative energy waves are present, and they interact through the corotational radius $r_c \simeq 12$, identifiable as the intersection between the mode frequency and the disk's orbital frequency (drawn as the white curve across the diagram). As expected, the two waves cannot propagate through a narrow forbidden region nearby the corotation radius, but they can still be transmitted by tunneling.
In the magnetized case, the diagrams show a broader range of excited frequencies instead of the narrow selection of the hydrodynamic model, and in the highly magnetized disk there seems to be a lack of positive energy waves across the disk. Only the region of the diagram with $\omega < \Omega$ is populated, and the fundamental mechanism responsible for the onset of the PPI does not appear to be in action. In the weakly magnetized model there are some positive energy components, but their amplitudes are still significantly smaller than in the hydrodynamic case.

Interaction between the two instabilities

From the previous analysis it seems clear that the inclusion of a toroidal magnetic field deeply affects the development of the PPI, even when the field is highly sub-thermal. The low magnetization model proved to be quite interesting, since it provides a sort of conjunction between the hydrodynamic one, where the PPI dominates the disk dynamics and leads to fast growth and saturation of the $m = 1$ mode, and the highly magnetized disk, where instead there are no clear signs of PPI development.
Considering both azimuthal and frequency spectra for $\sigma = 10^{-2}$, we noted a small excess of power in the $m = 1$ mode and the presence of positive energy perturbation outside the corotation radius that are absent for higher values of σ. These results suggest that for low magnetizations the PPI may still undergo a phase of linear growth, which then is stopped by the onset of the MRI. In particular, early accretion triggered by MHD turbulence leads to a faster redistribution of angular momentum across the disk. The free energy stored in the shearing flow decreases and the edge waves that should reach the corotation radius and transport energy are not efficient enough to sustain the unstable $m = 1$ mode. The signature of a depressed growth of this mode is nevertheless imprinted in the flow. It may be that for even lower values of the magnetic field strength the final excess of power in the $m = 1$ mode could continuously approach the hydrodynamic value.
Although the redistribution on angular momentum represents a possible explanation for the PPI suppression, another possible cause may be the MHD turbulence itself that, providing a turbulent viscosity, could damp the waves that constitute the PPI mode and lead to a less effective growth. Finally, the possible loss of the inner reflective boundary (once again due to accretion) may also inhibit the PPI growth (Hawley, 1991), while the study by Dwarkadas and Balbus (1996) argues that the stabilizing effect of an accretion flow is due more to the dynamics of the corotation point that changes in the presence of a radial velocity.
To confirm that for strong enough magnetic fields the disk dynamics is completely dominated by the MRI, we performed a run with the exact setup used in model T256r3s11 but reduced the azimuthal range to $[0, \pi]$ (model T256r3s11pi). The resulting dynamics was essentially equivalent to that when considering the full azimuthal range $[0, 2\pi]$. Since the artificial exclusion of the $m = 1$ mode did not significantly affect the results, we conclude that at least for a high enough magnetization value the PPI is effectively damped and cannot develop significantly because of the early influence of the MRI on the local environment.
This results may seem to be in disagreement with what was reported by Fu and Lai (2011), who performed an analytical study on the influence of magnetic fields (in both toroidal and poloidal configurations) on the stability on accretion tori. They found that a sufficiently strong toroidal magnetic field can further destabilize the disk and enhance PPI development. However, they assumed incompressibility in their analysis, and therefore they excluded all those modes that instead

of being the outcome of the interaction between two surface gravity waves (i.e. the principal branch of the instability) are instead the result of a pressure wave outside the corotation radius coupled to an internal edge wave. The nature of the mode and the measured growth rate in the hydrodynamic case are consistent with the analysis by Blaes and Hawley (1988).

5.3. Resistive models

We finally present some preliminary results involving models with a finite value of the magnetic resistivity η (see Table 5.4). We selected models T256r3s12 , and T256r3s11 and evolved them in a non-ideal framework, i.e. setting the plasma resistivity in the disk's center to $\eta_{\rm disk} = 10^{-3}$ and modulating it according to Eq. (5.5). This value of $\eta_{\rm disk}$ is well above the code's numerical dissipation (estimated to be $\sim 10^{-6}$), and represents therefore the action of a physical turbulent resistivity which damps the magnetic field but not the fluid velocity field.

As we saw in Section 5.2.3, compared to the hydrodynamic results the magnetized models deeply reshape the disk's structure and the distribution of power in non-axisymmetric modes. The $m = 1$ mode is suppressed, the overdensity that characterizes Model H256r3 does not develop, and the overall distribution of power among azimuthal modes appears more homogeneous. The only difference between models T256r3s12 and T256r3s11 is that the former exhibits a residual excess of power in the $m = 1$ mode, suggesting that the PPI can still undergo some growth for sufficiently small magnetic fields.
Fig. 5.18 shows the evolution in time of the power in the $m = 1$ and $m = 2$ modes of models H256r3 , T256r3s12 and T256r3s12e3. The introduction of the turbulent resistivity leads to a linear growth of the $m = 1$ mode that closely resembles that of the unmagnetized model, although the power saturates at a lower value. The $m = 2$ mode, on the other hand, exhibits a similar growth and saturation level to the magnetized model without resistivity. If we look at the spectra as a function of m (Fig. 5.19) we can clearly see how the lowly magnetized model is deeply affected by the turbulent resistivity, as the average density spectrum

	N_ϕ	$A(v^{\hat\phi})$	Excitation	$\sigma_c/10^{-2}$	$\eta_{\rm disk}$
T256r3s12e3	256	10^{-3}	Random	1	10^{-3}
T256r3s11e3	256	10^{-3}	Random	10	10^{-3}

Table 5.4.: List of the resistive models considered in our study, where N_ϕ is the number of grid points in azimuthal direction, $A(v^{\hat\phi})$ is the amplitude of the initial perturbations in $v^{\hat\phi}$, σ_c is the initial value of the magnetization at the center of the disk, and $\eta_{\rm disk}$ is the maximum resistivity.

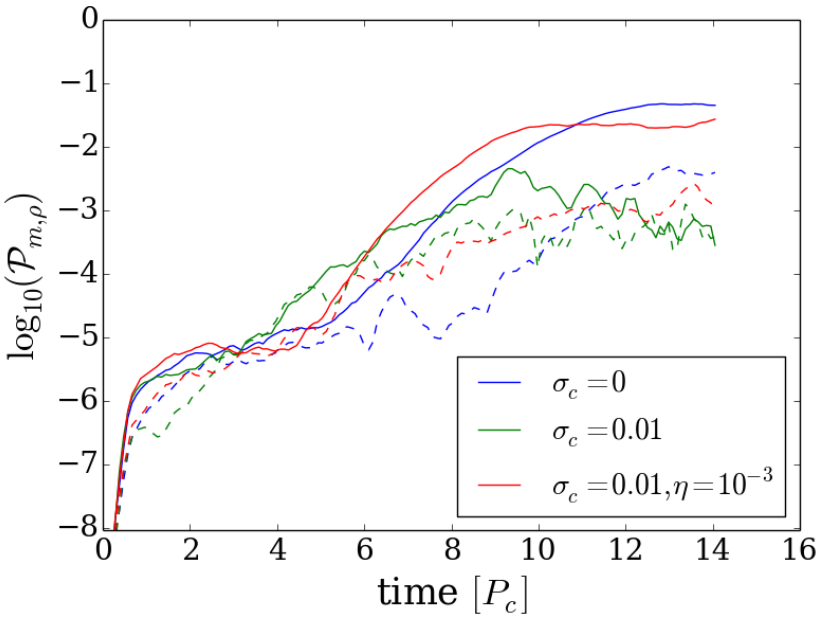

Figure 5.18.: Power in density for the $m = 1$ (solid curves) and $m = 2$ (dashed curves) modes for models H256r3 (blue), T256r3s12 (green) and T256r3s12e3 (red).

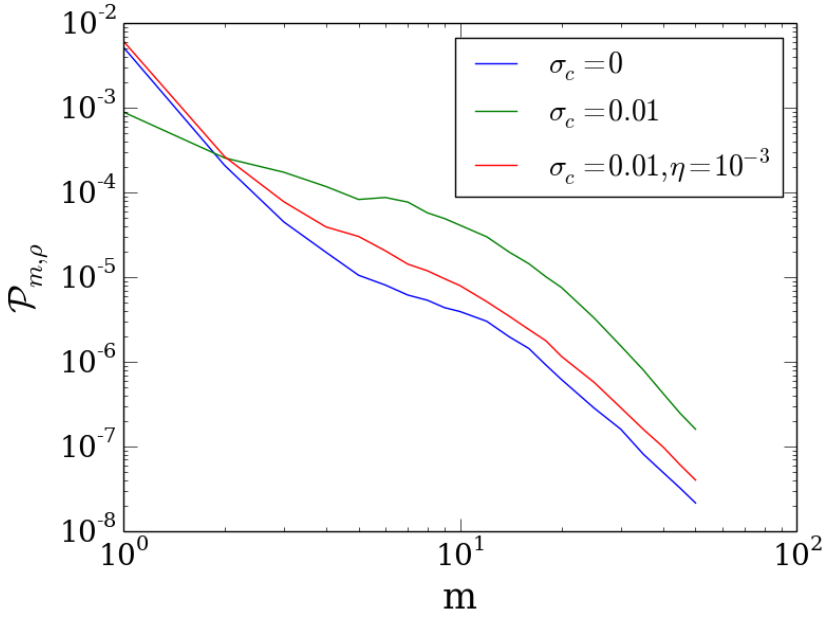

Figure 5.19.: Time-averaged equatorial rest mass density spectra as a function of azimuthal number m, comparing Model H256r3 (in blue) with models T256r3s12 (green) and T256r3s12e3 (red).

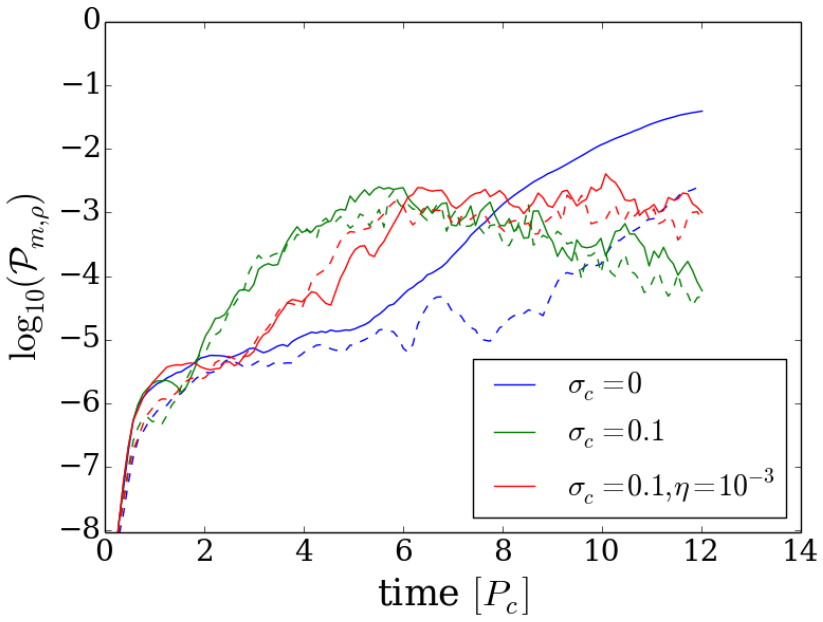

Figure 5.20.: Power in density for the $m = 1$ (solid curves) and $m = 2$ (dashed curves) modes for models H256r3 (blue), T256r3s11 (green) and T256r3s11e3 (red).

matches very well the one for the hydrodynamic case. The shapes of the spectra of models H256r3 (in blue) and T256r3s12e3 (in red) show the same behavior for $m < 3$ and $m > 10$, with a shallower slope at intermediate scales due to some residual action of the MRI.
The highly magnetized model ($\sigma_c = 0.1$) has a different response to the addition of resistivity. The initial growth of the $m = 1$ and $m = 2$ modes is delayed with respect to Model T256r3s11 (red curve in Fig. 5.20), but the later evolution matches quite well the ideal GRMHD case, with no clear separation between the two modes, and showing similar peak values. The fact that the power does not decrease as in the ideal case results from the finite dissipation of the field due to resistivity, which leads to less efficient accretion and less severe mass loss for the disk. A comparison of the spectra (Fig. 5.21) shows that resistivity does not drastically change the spectrum's shape. The power contained in the $m = 1$ mode is unaffected by a finite value of η, while dissipation significantly reduces the power in higher order modes.

Overall these results suggest that if the magnetic field is dissipated at a sufficiently high rate (because the field is weak enough or because the resistivity is high enough), the suppression of the PPI by the MRI becomes less effective. Hence, the hydrodynamic global instability has a chance to significantly develop and ultimately lead to the growth of a dominant $m = 1$ mode. Moreover, the whole power spectrum approaches the shape of the hydrodynamic case for Model T256r3s12e3, where the increased power of modes with $m > 2$ is due to a residual

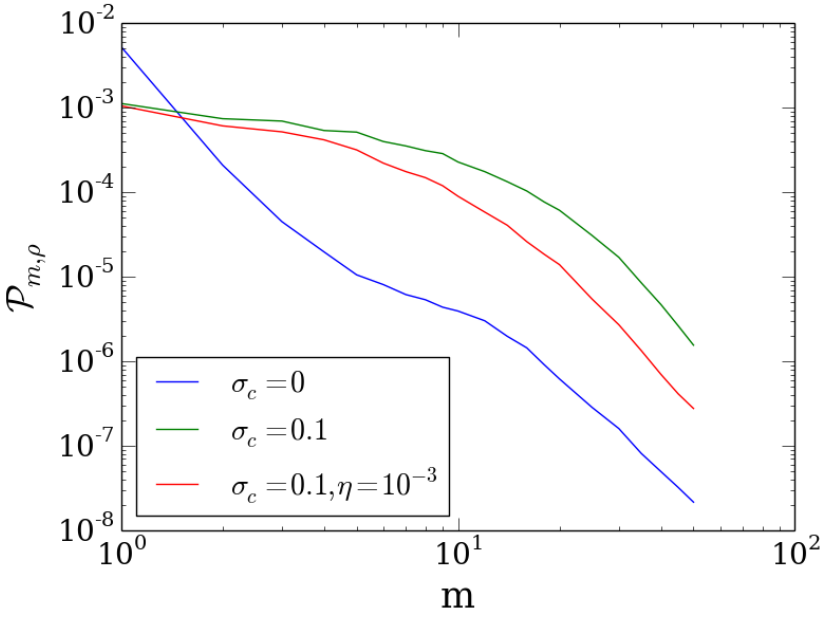

Figure 5.21.: Time-averaged equatorial rest mass density spectra as a function of azimuthal number m, comparing Model H256r3 (in blue) with models T256r3s11 (green) and T256r3s11e3 (red).

action of the MRI. Magnetic dissipation can not only restore the conditions for the onset of the PPI, but it also affects the power distribution throughout all scales, in particular reducing the excitation of higher order modes due to MRI.
The set of resistive simulations performed by us is very limited. We only considered two different magnetized models and applied the same turbulent resistivity to see how they would be affected by it. To better understand the response of the system to magnetic dissipation, it will be necessary to simulate the same magnetized models we considered so far for a significantly large range of values of η. Considering that the code's numerical dissipation (for the setup we used) is estimated to be $\sim 10^{-6}$, it will be important to adequately sample the range $\eta \in \{10^{-6}, 10^{-3}\}$ to check whether there is a smooth transition between the ideal GRMHD regime and the limit where the hydrodynamic results are recovered. Different spatial profiles for the magnetic resistivity need to be investigated too. Eq. (5.5) implies that most dissipation occurs at the disk's density maximum, hence close to the equatorial plane. However, this naive prescription appears to be incompatible with local measurements of turbulent transport coefficients in local shearing box simulations (Gressel, 2010), which on the contrary suggest that turbulent viscosity has a minimum in the equatorial plane and reaches a maximum at higher latitudes. We intend to investigate these effects in a forthcoming work.

6. Conclusions

We have presented a series of numerical simulations that investigate some of the fundamental physical mechanisms that take place in thick disks accreting onto black holes. The numerical tool used for this work is the GRMHD code `ECHO` (Del Zanna et al., 2007) in its most recent version developed during the last 4 years. Besides providing a fully covariant Ohm's law closure which allows one to evolve resistive astrophysical plasmas subjected to a mean-field dynamo mechanism, the code was also improved concerning its parallelization. The novel multidimensional `MPI` domain-decomposition made it possible to carry out computationally expensive three-dimensional GRMHD simulations, which were required by our goal to study the onset of non-axisymmetric instabilities in thick accretion disks.

As a test of the implementation of the non-ideal Ohm's closure (Bucciantini et al., 2012) we presented a kinematic study of an axisymmetric $\alpha\Omega$-dynamo in thick tori (Bugli et al., 2014). The classical mean-field theory (Moffatt, 1978b) provides a simple way to include the effect of unresolved small-scale turbulent motions to the evolution of large-scale quantities. The two most important phenomena that this formalism describes are the dissipation of magnetic field by *turbulent resistivity* and its amplification through the *α-effect*.
In the context of accretion disks, the inclusion of such non-ideal effects allows one to overcome the magnetic dissipation and close a *dynamo cycle*: poloidal magnetic field is produced by the mean-field dynamo (α-effect), while toroidal magnetic field is amplified by the flow's shear (Ω-effect).
In our study we show that the combined action of turbulent resistivity and α-effect produces regular patterns (i.e. dynamo waves) that drift through the disk (towards the equator or higher latitudes, depending on the sign of the dynamo parameter ξ) and ultimately dissipate. In the kinematic regime the values of resistivity η and ξ define the characteristics of the fastest growing mode selected by the system. Butterfly diagrams characterize the pattern's period and length-scale, which for higher values of ξ prove to be shorter and smaller respectively (and vice versa). The eigenmode's parity is determined by the initial magnetic field and remains unchanged during the system's evolution.
In a subsequent study we intend to investigate the evolution of the system beyond the linear phase, i.e. when the growth of the magnetic field is such that the dynamical effect of Lorentz force on the charged particles that constitute the

plasma can no longer be neglected. Therefore, to study the dynamics of an $\alpha\Omega$-dynamo it is necessary to integrate the full set of GRMHD equations, i.e. relax the kinematic approximation that we adopted. However, the α-effect as implemented in our scheme is not sensitive to the strength of the magnetic field, and a naive model coupling the plasma dynamics to an ever-growing dynamo mechanism would lead to unphysical results. In fact, the mean-field dynamo is expected to be *quenched* by the back-reaction of the disk's dynamics on the magnetic field. Although it is still a matter of debate how effective such a quenching mechanism would be (Brandenburg and Subramanian, 2005), one simple way to implement this effect is to assume that the dynamo parameter $\xi_{\rm disk}$ decreases as the magnetic energy $B^2/2$ reaches equipartition with the flow's kinetic energy $\rho v^2/2$, that is

$$\xi_{\rm disk} = \frac{\xi_0}{1 + B^2/\rho v^2}, \tag{6.1}$$

where ξ_0 is the value of the dynamo parameter in the linear phase of the growth. As the magnetic field gets stronger, the efficiency of the dynamo decreases and the system does not reach unphysically high magnetic energy values.
It would be important to further improve the modeling of the spatial dependence of the turbulent resistivity η and the parameter ξ on the local state of the plasma. The profiles that we used in our study, given by Eq. (5.6) and Eq. (5.8), are simple approximations based on our assumptions that the non-ideal effects should be confined within the disk and be more efficient in the high-density regions of the disk. As we mentioned in the last section of Chapter 5, these assumptions are in contrast with recent results of local shearing box simulations, which show that turbulent transport coefficients actually increase far from the equator as the density drops (Gressel, 2010). Taking into account a more accurate spatial profile for η and ξ would represent therefore a significant step forward in filling the gap between local and global simulations of accretion disks.

The main results of this thesis have been produced by performing a series of three-dimensional GRMHD simulations of magnetized thick accretion disks to estimate the interaction between two important instabilities that develop in these systems: the Papaloizou-Pringle instability (PPI) and the Magnetorotational instability (MRI). Both dynamical processes have been studied in great detail in the last 30 years, but to this date it is unclear how they interact and whether one dominates over the other. It is well known that wide unmagnetized tori are PPI unstable. This instability leads generally to the fast growth and dominance of a characteristic $m = 1$ azimuthal mode, which can leave an observable signature in the gravitational wave emission from all those sources that consist of a black-hole-torus system.
We find that in the presence of a weak toroidal field the growth of the non-axisymmetric $m = 1$ mode is significantly damped. While in the hydrodynamic case a large-scale smooth overdensity formation (sometimes referred to

as a *planet*) quickly forms after a few orbital periods of the disk, such a structure is mostly absent in our magnetized models, and the mass distribution appears more turbulent.
The inclusion of toroidal magnetic fields excites higher order modes, thus smaller length-scales, in contrast of the strong dominance of the $m = 1$ mode in the purely hydrodynamic case. A small excess of power in the $m = 1$ mode is still noticeable for our model with the lowest magnetization ($\sigma_c = 10^{-2}$) but not for stronger magnetic fields, suggesting therefore that the mode growth has been suppressed by the action of MRI. Our magnetized models show a significant increase in turbulent kinetic energy at stages earlier than the hydrodynamic one, and the significant Maxwell stresses introduced by the magnetic field trigger the accretion process faster than the PPI. Starting from a constant specific angular momentum profile (that represents the most PPI unstable configuration for an accretion disk), the unmagnetized disk is subject to angular momentum transport due to the PPI, which takes place in a non-local fashion across the disk and involving the inner and the outer regions at the same time. The introduction of MRI leads to a stronger and faster redistribution of angular momentum across the disk, consistently with the higher values of stresses and accretion rates found in the magnetized models.
A wave that drifts in the azimuthal direction with a particular frequency can in general either move faster or slower with respect to the surrounding medium. In the former case the wave is said to carry *positive energy*, otherwise it carries *negative energy*. The fundamental mechanism responsible for the growth of the PPI is the interaction of positive and negative energy waves at the corotation radius, i.e. where the angular velocity of the pattern matches the local orbital frequency of the disk. When magnetic fields are included, we find almost no trace of waves beyond the corotation radius, suggesting that the PPI has been suppressed. This could be due to a redistribution of angular momentum driven by MRI that drives the disk to a PPI stable configuration, or it could be the effect of MHD turbulence that damps the waves taking part in the process.

Our results suggest that for sufficiently strong magnetic fields the dominance of the $m = 1$ mode (with respect to higher order ones) due to PPI should not be present in thick tori, but there are some caveats that need to be addressed. First, we have neglected the self-gravity of the disk. This is expected to be a good approximation for example in X-ray binaries, but not in the case of the remnant of a NS-NS merger that produces a black-hole-torus system. It has been shown by **?** that the gravitational interaction between the disk and the central black hole can excite the $m = 1$ mode, hence leading to a different outcome than the one we find in our analysis by including a magnetic field.
Another important aspect is the role of turbulent resistivity. We performed a limited number of simulations with a finite value of η for the magnetized models

with lowest and highest magnetization. In the former model, the $m = 1$ mode is dominant throughout the whole simulation, resembling quite closely the hydrodynamic case and in strong contrast to the ideal GRMHD model. On the other hand, the highly magnetized model did not exhibit such a behavior, and the overall structure of its disk and power spectra remained quite similar to the case of an ideally conducting plasma. These findings suggest that when magnetic fields are sufficiently dissipated, the suppression of the PPI by the MRI becomes less effective and the hydrodynamic scenario of a dominant $m = 1$ mode can develop once again. To draw more definitive conclusions on this matter, though, it will be necessary to perform a larger number of simulations. In particular, it would be important to assess whether, for a given magnetized model, there is a threshold value of resistivity beyond which the PPI can still develop or instead there is a continuous transition between the two regimes.

As for the $\alpha\Omega$-dynamo study, a more accurate prescription of the spatial profile of resistivity could be crucial. In our study the regions of high magnetization coincide with those of high density, hence the magnetic field dissipation was particularly effective. Implementing a more physical profile that implies stronger turbulent motions away from the equator could lead to a very different damping of the MRI action and maybe even to a revival of PPI suppression, which was almost completely eliminated in our resistive low magnetization model.

It remains also to be seen what happens for even weaker magnetic fields than the ones we considered; our findings suggest that there may be a smooth transition between the $m = 1$ dominated hydrodynamic case and the turbulent scenario produced by MRI activity, so that for higher values of β the excess in the $m = 1$ mode power could approach the one produced by the PPI. Alternatively, for weaker initial fields the MRI could tend toward a state independent of the initial field that is able to suppress the action of the PPI. To answer this question higher resolution simulations are required, since the characteristic length of the fastest growing MRI mode shrinks with the strength of the magnetic field.

Furthermore, we considered only the presence of a toroidal magnetic field, while a more complete analysis should include a poloidal magnetic field component as well. This component would excite so-called *channel modes* (Balbus and Hawley, 1998) and possibly lead to significantly different results. The size of the torus may also play a role, as the stability to the PPI of a thick disk depends quite strongly to the location of the inner and outer boundaries.

Ultimately, we cannot draw conclusive statements on the faith of the PPI in magnetized disks, as the number of decisive factors involved in the problem appears to be significantly high. What we could do was to identify the role played by non-axisymmetric MRI modes, and formulate some general statements on the influence of magnetic fields once a particular disk model and field topology were selected. Forthcoming studies should be able to give a better understanding of magnetized disk's stability and the underlying fundamental physical mechanisms.

Bibliography

M. Abramowicz, M. Jaroszynski, and M. Sikora. Relativistic, accreting disks. *A&A* , 63:221–224, February 1978.

M. A. Abramowicz and P. C. Fragile. Foundations of Black Hole Accretion Disk Theory. *Living Reviews in Relativity*, 16:1, December 2013. doi: 10.12942/lrr-2013-1.

M. Alcubierre. *Introduction to 3+1 Numerical Relativity*. Oxford University Press, UK, 2008. ISBN 978-0-19-920567-7.

M. A. Aloy, E. Mueller, J. M. Ibanez, J. M. Marti, and A. MacFadyen. Relativistic Jets from Collapsars. *ArXiv Astrophysics e-prints*, October 1999.

R. L. Arnowitt, S. Deser, and C. W. Misner. *Canonical analysis of general relativity*, page 127. 1962.

S. A. Balbus and J. F. Hawley. A powerful local shear instability in weakly magnetized disks. I - Linear analysis. II - Nonlinear evolution. *ApJ*, 376:214–233, July 1991. doi: 10.1086/170270.

S. A. Balbus and J. F. Hawley. A Powerful Local Shear Instability in Weakly Magnetized Disks. IV. Nonaxisymmetric Perturbations. *ApJ*, 400:610–621, December 1992. doi: 10.1086/172022.

S. A. Balbus and J. F. Hawley. Instability, turbulence, and enhanced transport in accretion disks. *Reviews of Modern Physics*, 70:1–53, January 1998. doi: 10.1103/RevModPhys.70.1.

J. M. Bardeen, W. H. Press, and S. A. Teukolsky. Rotating Black Holes: Locally Nonrotating Frames, Energy Extraction, and Scalar Synchrotron Radiation. *ApJ*, 178:347–370, December 1972. doi: 10.1086/151796.

O. M. Blaes and W. Glatzel. On the stability of incompressible constant angular momentum cylinders. *MNRAS*, 220:253–258, May 1986. doi: 10.1093/mnras/220.2.253.

O. M. Blaes and J. F. Hawley. Nonaxisymmetric disk instabilities - A linear and nonlinear synthesis. *ApJ*, 326:277–291, March 1988. doi: 10.1086/166089.

R. D. Blandford and R. L. Znajek. Electromagnetic extraction of energy from Kerr black holes. *MNRAS*, 179:433–456, May 1977.

T. J. M. Boyd and J. J. Sanderson. *The Physics of Plasmas*. January 2003.

A. Brandenburg and K. Subramanian. Astrophysical magnetic fields and nonlinear dynamo theory. *Physics Reports*, 417:1–209, October 2005. doi: 10.1016/j.physrep.2005.06.005.

N. Bucciantini, B. D. Metzger, T. A. Thompson, and E. Quataert. Short gamma-ray bursts with extended emission from magnetar birth: jet formation and collimation. *MNRAS*, 419:1537–1545, January 2012. doi: 10.1111/j.1365-2966.2011.19810.x.

M. Bugli, L. Del Zanna, and N. Bucciantini. "Dynamo action in thick discs around Kerr black holes: high-order resistive GRMHD simulations". *MNRAS*, 440:L41–L45, may 2014.

J. C. Butcher. Numerical methods for ordinary differential equations in the 20th century. *Journal of Computational and Applied Mathematics*, 125:1–29, December 2000. doi: 10.1016/S0377-0427(00)00455-6.

S. Chandrasekhar. The Stability of Non-Dissipative Couette Flow in Hydromagnetics. *Proceedings of the National Academy of Science*, 46:253–257, February 1960. doi: 10.1073/pnas.46.2.253.

P. Colella and P. R. Woodward. The Piecewise Parabolic Method (PPM) for Gas-Dynamical Simulations. *Journal of Computational Physics*, 54:174–201, September 1984. doi: 10.1016/0021-9991(84)90143-8.

T. G. Cowling. *Magnetohydrodynamics*. Hilger, 1976.

J.-P. De Villiers and J. F. Hawley. Three-dimensional Hydrodynamic Simulations of Accretion Tori in Kerr Spacetimes. *ApJ*, 577:866–879, October 2002. doi: 10.1086/342238.

L. Del Zanna and N. Bucciantini. An efficient shock-capturing central-type scheme for multidimensional relativistic flows. I. Hydrodynamics. *A&A* , 390: 1177–1186, August 2002. doi: 10.1051/0004-6361:20020776.

L. Del Zanna, N. Bucciantini, and P. Londrillo. An efficient shock-capturing central-type scheme for multidimensional relativistic flows. II. Magnetohydrodynamics. *A&A* , 400:397–413, March 2003. doi: 10.1051/0004-6361:20021641.

L. Del Zanna, O. Zanotti, N. Bucciantini, and P. Londrillo. ECHO: a Eulerian conservative high-order scheme for general relativistic magnetohydrodynamics and magnetodynamics. *A&A* , 473:11–30, 2007. doi: 10.1051/0004-6361:20077093.

V. V. Dwarkadas and S. A. Balbus. Gasdynamical Stability of Shear Flow in Spiral Arms of Disk Galaxies. *ApJ*, 467:87, August 1996. doi: 10.1086/177586.

R. P. Fender, T. M. Belloni, and E. Gallo. Towards a unified model for black hole X-ray binary jets. *MNRAS*, 355:1105–1118, December 2004. doi: 10.1111/j.1365-2966.2004.08384.x.

J. A. Font and F. Daigne. The runaway instability of thick discs around black holes - I. The constant angular momentum case. *MNRAS*, 334:383–400, August 2002. doi: 10.1046/j.1365-8711.2002.05515.x.

F. Foucart, M. D. Duez, L. E. Kidder, M. A. Scheel, B. Szilagyi, and S. A. Teukolsky. Black hole-neutron star mergers for $10M_{\odot}$ black holes. *Physical Review D*, 85(4):044015, February 2012. doi: 10.1103/PhysRevD.85.044015.

P. C. Fragile and A. Sadowski. On the Decay of Strong Magnetization in Global Disc Simulations with Toroidal Fields. *ArXiv e-prints*, January 2017.

J. Frank, A. King, and D. Raine. *Accretion Power in Astrophysics*. Cambridge University Press, 2002. ISBN 9780521629577. URL `https://books.google.de/books?id=GGM_t-xn8ocC`.

W. Fu and D. Lai. Papaloizou-Pringle instability of magnetized accretion tori. *MNRAS*, 410:1617–1630, January 2011. doi: 10.1111/j.1365-2966.2010.17544.x.

W. Glatzel. On the stability of compressible differentially rotating cylinders. *MNRAS*, 225:227–255, March 1987. doi: 10.1093/mnras/225.2.227.

P. Goldreich, J. Goodman, and R. Narayan. The stability of accretion tori. I - Long-wavelength modes of slender tori. *MNRAS*, 221:339–364, July 1986. doi: 10.1093/mnras/221.2.339.

O. Gressel. A mean-field approach to the propagation of field patterns in stratified magnetorotational turbulence. *MNRAS*, 405:41–48, June 2010. doi: 10.1111/j.1365-2966.2010.16440.x.

A. Harten. High Resolution Schemes for Hyperbolic Conservation Laws. *Journal of Computational Physics*, 49:357–393, March 1983. doi: 10.1016/0021-9991(83)90136-5.

P. D. Harten, A. Lax and B. van Leer. On Upstream Differencing and Godunov-Type Schemes for Hyperbolic Conservation Laws. *SIAM Rev.*, 25:35, 1983.

J. F. Hawley. Three-dimensional simulations of black hole tori. *ApJ*, 381:496–507, November 1991. doi: 10.1086/170673.

J. F. Hawley, X. Guan, and J. H. Krolik. Assessing Quantitative Results in Accretion Simulations: From Local to Global. *ApJ*, 738:84, September 2011. doi: 10.1088/0004-637X/738/1/84.

S. Kato, editor. *Oscillations of Disks*, volume 437 of *Astrophysics and Space Science Library*, 2016. doi: 10.1007/978-4-431-56208-5.

R. P. Kerr. Gravitational Field of a Spinning Mass as an Example of Algebraically Special Metrics. *Physical Review Letters*, 11:237–238, September 1963. doi: 10.1103/PhysRevLett.11.237.

K. Kiuchi, Y. Sekiguchi, M. Shibata, and K. Taniguchi. Exploring Binary-Neutron-Star-Merger Scenario of Short-Gamma-Ray Bursts by Gravitational-Wave Observation. *Physical Review Letters*, 104(14):141101, April 2010. doi: 10.1103/PhysRevLett.104.141101.

K. Kiuchi, M. Shibata, P. J. Montero, and J. A. Font. Gravitational Waves from the Papaloizou-Pringle Instability in Black-Hole-Torus Systems. *Physical Review Letters*, 106(25):251102, June 2011. doi: 10.1103/PhysRevLett.106.251102.

S. S. Komissarov. Magnetized tori around Kerr black holes: analytic solutions with a toroidal magnetic field. *MNRAS*, 368:993–1000, May 2006. doi: 10.1111/j.1365-2966.2006.10183.x.

M. Kozlowski, M. Jaroszynski, and M. A. Abramowicz. The analytic theory of fluid disks orbiting the Kerr black hole. *A&A* , 63:209–220, February 1978.

P. Kumar and B. Zhang. The physics of gamma-ray bursts & relativistic jets. *Physics Reports*, 561:1–109, February 2015. doi: 10.1016/j.physrep.2014.09.008.

G. Lesur and P.-Y. Longaretti. On the relevance of subcritical hydrodynamic turbulence to accretion disk transport. *A&A* , 444:25–44, December 2005. doi: 10.1051/0004-6361:20053683.

X.-D. Liu and S. Osher. Convex ENO High Order Multi-dimensional Schemes without Field by Field Decomposition or Staggered Grids. *Journal of Computational Physics*, 142:304–330, May 1998. doi: 10.1006/jcph.1998.5937.

P. Londrillo and L. del Zanna. On the divergence-free condition in Godunov-type schemes for ideal magnetohydrodynamics: the upwind constrained transport method. *Journal of Computational Physics*, 195:17–48, March 2004. doi: 10.1016/j.jcp.2003.09.016.

D. Lynden-Bell. Galactic Nuclei as Collapsed Old Quasars. *Nature*, 223:690–694, August 1969. doi: 10.1038/223690a0.

D. Lynden-Bell and J. E. Pringle. The evolution of viscous discs and the origin of the nebular variables. *MNRAS*, 168:603–637, September 1974. doi: 10.1093/mnras/168.3.603.

A. I. MacFadyen and S. E. Woosley. Collapsars: Gamma-Ray Bursts and Explosions in "Failed Supernovae". *ApJ*, 524:262–289, October 1999. doi: 10.1086/307790.

A. Marconi, G. Risaliti, R. Gilli, L. K. Hunt, R. Maiolino, and M. Salvati. Local supermassive black holes, relics of active galactic nuclei and the X-ray background. *MNRAS*, 351:169–185, June 2004. doi: 10.1111/j.1365-2966.2004.07765.x.

J. C. McKinney and R. D. Blandford. Stability of relativistic jets from rotating, accreting black holes via fully three-dimensional magnetohydrodynamic simulations. *MNRAS*, 394:L126–L130, March 2009. doi: 10.1111/j.1745-3933.2009.00625.x.

J. C. McKinney and C. F. Gammie. A Measurement of the Electromagnetic Luminosity of a Kerr Black Hole. *ApJ*, 611:977–995, August 2004. doi: 10.1086/422244.

F. C. Michel. Accretion of Matter by Condensed Objects. *Ap&SS*, 15:153–160, January 1972. doi: 10.1007/BF00649949.

H. K. Moffatt. *Magnetic field generation in electrically conducting fluids*. Cambridge, England, Cambridge University Press, 1978. 353 p., 1978a.

H. K. Moffatt. *Magnetic field generation in electrically conducting fluids*. Cambridge, 1978b.

R. Narayan and I. Yi. Advection-dominated Accretion: Underfed Black Holes and Neutron Stars. *ApJ*, 452:710, October 1995. doi: 10.1086/176343.

S. C. Noble, J. H. Krolik, and J. F. Hawley. Dependence of Inner Accretion Disk Stress on Parameters: The Schwarzschild Case. *ApJ*, 711:959–973, March 2010. doi: 10.1088/0004-637X/711/2/959.

C. Palenzuela, L. Lehner, O. Reula, and L. Rezzolla. Beyond ideal MHD: towards a more realistic modelling of relativistic astrophysical plasmas. *MNRAS*, 394:1727–1740, 2009. doi: 10.1111/j.1365-2966.2009.14454.x.

J. C. B. Papaloizou and J. E. Pringle. The dynamical stability of differentially rotating discs with constant specific angular momentum. *MNRAS*, 208:721–750, June 1984.

L. Pareschi and G. Russo. Implicit-Explicit Runge-Kutta Schemes and Applications to Hyperbolic Systems with Relaxation. *Journal of Scientific Computing*, 25(1-2):129, 2005.

R. Penrose. Gravitational Collapse: the Role of General Relativity. *Nuovo Cimento Rivista Serie*, 1, 1969.

T. Piran. Gamma-ray bursts and the fireball model. *Physics Reports*, 314:575–667, June 1999. doi: 10.1016/S0370-1573(98)00127-6.

E. Priest. *Magnetohydrodynamics of the Sun*. Cambridge University Press, May 2014.

M. J. Rees. Black Hole Models for Active Galactic Nuclei. *ARA&A*, 22:471–506, 1984. doi: 10.1146/annurev.aa.22.090184.002351.

R. A. Remillard and J. E. McClintock. X-Ray Properties of Black-Hole Binaries. *ARA&A*, 44:49–92, September 2006. doi: 10.1146/annurev.astro.44.051905.092532.

C. S. Reynolds. Measuring Black Hole Spin Using X-Ray Reflection Spectroscopy. *Spac.Scienc.Review*, 183:277–294, September 2014. doi: 10.1007/s11214-013-0006-6.

L. Rezzolla and O. Zanotti. *Relativistic Hydrodynamics*. Oxford University Press, September 2013.

L. Rezzolla, L. Baiotti, B. Giacomazzo, D. Link, and J. A. Font. Accurate evolutions of unequal-mass neutron-star binaries: properties of the torus and short GRB engines. *Classical and Quantum Gravity*, 27(11):114105, June 2010. doi: 10.1088/0264-9381/27/11/114105.

P. H. Roberts. Kinematic Dynamo Models. *Philosophical Transactions of the Royal Society of London Series A*, 272:663–698, August 1972. doi: 10.1098/rsta.1972.0074.

B. R. Ryan, C. F. Gammie, S. Fromang, and P. Kestener. Resolution Dependence of Magnetorotational Turbulence in the Isothermal Stratified Shearing Box. *ArXiv e-prints*, February 2017.

A. Sądowski. Thin accretion discs are stabilized by a strong magnetic field. *MNRAS*, 459:4397–4407, July 2016. doi: 10.1093/mnras/stw913.

N. I. Shakura and R. A. Sunyaev. Black holes in binary systems. Observational appearance. *A&A* , 24:337–355, 1973.

M. Shibata and K. Uryū. Merger of black hole-neutron star binaries: Nonspinning black hole case. *Physical Review D*, 74(12):121503, December 2006. doi: 10.1103/PhysRevD.74.121503.

Raymond J. Spiteri and Steven J. Ruuth. A new class of optimal high-order strong-stability-preserving time discretization methods. *SIAM Journal on Numerical Analysis*, 40(2):469–491, 2003. ISSN 00361429. URL `http://www.jstor.org/stable/4100965`.

A. Suresh and H. T. Huynh. Accurate Monotonicity-Preserving Schemes with Runge Kutta Time Stepping. *Journal of Computational Physics*, 136:83–99, September 1997. doi: 10.1006/jcph.1997.5745.

M. Wielgus, P. C. Fragile, Z. Wang, and J. Wilson. Local stability of strongly magnetized black hole tori. *MNRAS*, 447:3593–3601, March 2015. doi: 10.1093/mnras/stu2676.

S. E. Woosley. Gamma-ray bursts from stellar mass accretion disks around black holes. *ApJ*, 405:273–277, March 1993. doi: 10.1086/172359.

J. W. York, Jr. Kinematics and dynamics of general relativity. In L. L. Smarr, editor, *Sources of Gravitational Radiation*, pages 83–126, 1979.

A. Appendix

A.1. Coordinate transformation

The gravitational background of our simulations is shaped by a central black hole of mass M and spin a. To avoid any spurious numerical artifact that could arise from the inner radial boundary, we decided to adopt the so-called *Kerr-Schild coordinates* (KS), that allow one to remove the unphysical singularity at the black hole event horizon and place the domain's inner boundary beyond it.
To exploit the regularity property of these coordinates, we perform a transformation of all the primitive variables computed for a stationary torus in Boyer-Lindquist (BL) coordinates. In the following, the labels KS and BL indicate quantities measured by KS and BL *Eulerian observer* respectively, while unprimed and primed indices refer to quantities expressed in KS and BL *coordinates*.
We start by considering the linear transformation that relates the two coordinate systems:

$$\mathcal{A}^{\mu}_{\mu'} = \begin{pmatrix} 1 & G & 0 & 0 \\ 0 & 1 & 0 & 0 \\ 0 & 0 & 1 & 0 \\ 0 & H & 0 & 1 \end{pmatrix} \text{ with } \begin{cases} G = -\frac{2r}{\Delta} \\ H = -\frac{a}{\Delta} \end{cases} \tag{A.1}$$

where $\Delta = r^2 - 2Mr + a^2$, r is the radial coordinate and a is in general non vanishing. This transformation relates vectors and tensors respectively:

$$x^{\mu}_{\mu'} = \mathcal{A}^{\mu}_{\mu'} x^{\mu'}, \tag{A.2}$$

$$T^{\mu\nu} = \mathcal{A}^{\mu}_{\mu'} \mathcal{A}^{\nu}_{\nu'} T^{\mu'\nu'}. \tag{A.3}$$

We also have to consider that Eulerian observers in the two coordinate systems are not identical in general, i.e. we cannot simply apply the transformation in Eq. (A.1) to the vectorial primitive variables $(\boldsymbol{v}, \boldsymbol{B}, \boldsymbol{E})$, which represent quantities measured in an Eulerian frame of reference. For quantities like the fluid four-velocity u^{μ} and the Faraday tensor $F^{\mu\nu}$, on the other hand, one must only apply Eq. (A.1) to fully take into account the change of frame of reference (e.g., $\mathcal{A}^{\mu}_{\mu'} u^{\mu'}_{\mathrm{BL}} = u^{\mu}_{\mathrm{KS}}$). The goal is then to obtain for $\boldsymbol{v}$, $\boldsymbol{E}$, and $\boldsymbol{B}$ the correct relation

between KS components measured by the KS Eulerian observer and BL components measured by the BL Eulerian observer.
We first write the spatial velocity, magnetic field, and electric field in terms of four-velocity and Faraday tensor in KS coordinates as measured by the KS Eulerian observer:

$$v^i_{\rm KS} = \frac{1}{\alpha}\left(\frac{u^i}{u^t} + \beta^i\right), \tag{A.4}$$

$$B^i_{\rm KS} = \alpha_{\rm KS} F^{*ti}_{\rm KS}, \tag{A.5}$$

$$E^i_{\rm KS} = \alpha_{\rm KS} F^{ti}_{\rm KS}. \tag{A.6}$$

Then we use Eq. (A.1) to transform the components of $u^i_{\rm KS}$, $F^{*ti}_{\rm KS}$ and $F^{ti}_{\rm KS}$ in BL coordinates. Finally, using Eq. (3.17), Eq. (3.19) and Eq. (3.20) we rewrite them in terms of $v^{i'}_{\rm BL}$, $E^{i'}_{\rm BL}$ and $B^{i'}_{\rm BL}$. The result gives the correct transformation rules:

$$v^i_{\rm KS} = \frac{1}{\alpha_{\rm KS}}\left[\frac{\mathcal{A}^i_{j'}(\alpha_{\rm BL} v^{j'}_{\rm BL} - \beta^{j'}_{\rm BL})}{1 - \mathcal{A}^0_{r'}\alpha_{\rm BL} v^{r'}_{\rm BL}} + \beta^i_{\rm KS}\right], \tag{A.7}$$

$$B^i_{\rm KS} = \frac{\alpha_{\rm KS}}{\alpha_{\rm BL}}\left\{B^i_{\rm BL} - \mathcal{A}^0_{r'}\left[B^{r'}_{\rm BL}\beta^i_{\rm BL} + \frac{\alpha_{\rm BL}}{\gamma^{1/2}_{\rm BL}}\left(\delta^i_{\phi'}E^{\rm BL}_{\theta'} - \delta^i_{\theta'}E^{\rm BL}_{\phi'}\right)\right]\right\}, \tag{A.8}$$

$$E^i_{\rm KS} = \frac{\alpha_{\rm KS}}{\alpha_{\rm BL}}\left\{E^i_{\rm BL} - \mathcal{A}^0_{r'}\left[E^{r'}_{\rm BL}\beta^i_{\rm BL} - \frac{\alpha_{\rm BL}}{\gamma^{1/2}_{\rm BL}}\left(\delta^i_{\phi'}B^{\rm BL}_{\theta'} - \delta^i_{\theta'}B^{\rm BL}_{\phi'}\right)\right]\right\}. \tag{A.9}$$